

Master Thesis

**Development and Experiment of Snow-Avalanche
Monitoring at Mt. Fuji**

Wataru Ikeda

Earthquake Research Institute

Department of Earth & Planetary Science

Graduate School of Science, The University of Tokyo

March 1, 2021

Abstract

In Mt. Fuji (a stratovolcano and highest mountain in Japan), avalanches are frequently released during winter. Monitoring of snow avalanches in natural field is very important to ensure the safety around snowy mountains, which have a potential risk of avalanche to infrastructures and recreational users. However, monitoring a high-altitude mountain is not easy, especially during winters, due to the poor accessibility and visibility, limited power supply, and severe conditions. Since the avalanches often emanate infrasonic and seismic waves, we installed infrasound microphones, seismometers, and thermometer probes at north side of Mt. Fuji for 2 winter seasons (2018-2019 and 2019-2020 winter season) to record the avalanches and weather condition (especially snow depth).

The infrasound microphone pairs were installed in 2 stations along with the seismometers in the 2018-2019 winter observation. We detected 46 signals, which were assumed to be generated by avalanches in Mt. Fuji. By comparing the power spectra of the infrasound data and the collocated seismometer data at a station, we successfully distinguished the infrasonic and seismic signals. Surprisingly, only 4 of 46 detected events were estimated to involve both seismic and infrasonic signals, while only infrasonic signals were detected in the other 42 events. Furthermore, based on the estimated snow depth by the thermometer probes, the 4 events with seismic signals occurred during the snowfall and temperature rise in spring. We expected that the whole volumes of the 4 avalanches and their dense parts increased to generate seismic waves as well as infrasound waves.

In the 2019-2020 winter observation, we installed the infrasound arrays and high-resolution thermometer probes at stations on the fifth and seventh steps, respectively. We detected 29 possible avalanche signals. Using the multi-channel semblance method, we could estimate that 26 of those detected events originated from the slopes in the range from north-west to north-east from the array. On the contrary, the number of detected avalanches which were estimated to be originated from the other slopes were only 3. Therefore, we hypothesize that the topographical features of Mt. Fuji limit the observable areas by the infrasonic array at one station.

In both winter season, most of the events were detected during and shortly after the new snowfall or snowmelt. We expect that this is the reliable data to estimate that the snowfall and snowmelt is the dominant factor for the avalanches.

Based on the observation of the 2 winter seasons, we revealed that the following points are essential for the observation of avalanches at Mt. Fuji; the installation of both infrasound microphones and seismometers is effective to monitor the avalanches, multiple infrasound stations are necessary to cover the wide range of slopes in the corn-shaped mountain, and the combination of infrasonic and seismic methods and thermometer probes allow to consider the relationship between weather conditions (such as snowfall, snowmelt, precipitation and rise in temperature) and avalanches. In addition, our observations uncovered the background noises against the infrasound measurements at Mt. Fuji for the first time.

Lastly, based on the observation and discussion in the 2 winter seasons, we propose a snow-avalanche monitoring system suitable for Mt. Fuji.

要旨

富士山では冬季に雪崩が頻繁に発生し、雪崩のモニタリングは道路や建造物の保護や登山者等の安全を確保するためにも重要である。しかしながら、富士山のような高山での冬季観測はアクセスの悪さや環境の過酷さ、視界の悪さ、電源等の制約など様々な課題が存在する。そこで、本研究では雪崩が空振波や地震波を発生させることに注目し、空振計および地震計を使用して富士山の雪崩をリモートかつ包括的に観測することを目指し、2冬(2018-2019 冬と 2019-2020 冬)の観測を行った。また同時に温度プローブ(簡易的に温度計を鉛直に並べたもの)を設置して、積雪・気象状態のモニタリングも行った。本研究では、特に、空振と積雪の計測や解析に独自の工夫を試みた。

まず 2018-2019 年冬シーズンの観測では、2 個の空振計を 10m 程度に離して 2 点設置し、雪崩と考えられる 46 のイベントを検出することに成功した。これらのシグナルのパワースペクトルを空振計と地震計で比較することにより、そのうちの 4 イベントのみが地震波を伴うイベントで、残りのイベントは全て空振波のみを伴うことが判明した。さらに温度プローブから推定された気象情報と合わせると、これらの地震波を伴う 4 イベントは全て 4 月の降雪とその後の昇温で起こっていると推察される。これは、以上のような天候により、発生する雪崩の総量が増加するとともに重いフローが発生しやすくなったためだと考えられる。

2019-2020 年の観測では、空振アレイを 1 点設置し、29 のイベントに対してマルチチャンネルセンブリランス法でその波源を推定した。そのうちの 26 のシグナルの波源が空振アレイを設置した場所の北西から北東の斜面に集中していた。それ以外の斜面に波源が推定されたイベントは 3 つのみであり、これは富士山の地理的な影響で 1 点での空振アレイ観測では円錐状の富士山の広い斜面をカバーすることは出来ないためではないかと推測される。

2 冬の観測結果ではいずれも雪崩と思われるイベントは降雪中や降雪の直後、もしくは融雪期に集中していた。

以上の観測から雪崩の観測には空振計と地震計の併設が有効であること、円錐状の火山で広範囲の斜面をモニタリングするためには複数観測点を設置する必要があること、プローブ式温度計による積雪把握が雪崩と積雪・天候状態との関

係を把握するために重要であることが明らかになった。さらに富士山の空振観測に対するノイズ環境が初めて観測された。

以上の観測結果を踏まえて、富士山の雪崩を空振計と地震計で包括的に監視するために最適な手法を考案した。

Contents

1. Introduction.....	8
<u>1-1 Infrasound and Seismic Observations</u>	8
Infrasonic Observation	
Seismic Observation	
Infrasonic and Seismic Observation	
<u>1-2 Thermometer Probe</u>	12
2. Observation.....	13
<u>2-0 Study Area</u>	13
<u>2-1 2018-2019 Winter Season</u>	14
2-1-1 Infrasound Microphone	
2-1-2 Seismometers	
2-1-3 Thermometer Probe	
<u>2-2 2019-2020 Winter Season</u>	17
2-2-1 Infrasound Microphone	
2-2-2 Seismometers	
2-2-3 Thermometer Probe	
3. Analysis.....	22
<u>3-1 2018-2019 Winter Season</u>	22
3-1-1 Infrasound Array	
Signal Detection	
Distinction of Seismic and Infrasonic Signal	
Calculation Methods of Infrasound Visibility	
3-1-2 Thermometer Probe	
<u>3-2 2019-2020 Winter Season</u>	29
3-2-1 Infrasound	
Signal Detection	
Minimization of Correlation Vector	
Exclusion of Inconsistent Signals	
Multi-Channel Semblance	
Calculation Methods of Infrasound Visibility	
3-2-2 Wind Level	
3-2-3 Thermometer Probe	

4. Results.....	40
<u>4-1 2018-2019 Winter Season</u>	40
4-1-1 Infrasound Microphones and Seismometers	
Signal Detection	
Distinction of Infrasonic and Seismic Signals	
Signal Comparisons Among Different Stations	
Visibility	
4-1-2 Thermometer Probe	
<u>4-2 2019-2020 Winter Season</u>	48
4-2-1 Infrasound Microphones and Seismometers	
Detected Events	
Source Detection by Multi-Channel Semblance	
Seismic Signals	
Accuracy of Multi-Channel Semblance	
Visibility and Wind Level	
4-2-2 Thermometer Probe and Snowfall	
5. Discussion	67
<u>5-1 2018-2019 Winter Season</u>	67
5-1-1 Infrasound Microphones and Seismometers	
Verification of Infrasonic and Seismic Signals	
Infrasonic Signal and Seismic Signal	
5-1-2 Thermometer Probe and Avalanche Events	
<u>5-2 2019-2020 Winter Season</u>	71
5-2-1 Snowfall Estimation by Thermometer Probe	
Difference in the Results between Thermometer Probes	
and the Automatic Meteorological Observatory	
Behavior of Estimated Snowfall	
Observation of Precipitation	
The Advantage of Thermometer Probes	
5-2-2 Array Analysis of Infrasound Microphones	
Visibility and the Noise Level of Infrasound Microphones	
Verification of Infrasound and Seismic Signals	
Analysis on the Results of Source Estimation	
by Multi-Channel Semblance	
Differences between This Observation and Other Previous Studies	

<u>5-3 Designing Infrasound Observation for Snow Avalanches at Mt. Fuji</u>	78
5-3-1 Ambient Infrasound Noise at Mt. Fuji	
5-3-2 Comparison of the Infrasound Observations in 2018-2019 and in 2019-2020	
5-3-3 Designing Infrasound Observation for Snow Avalanches at Mt. Fuji	
6. Conclusions.....	84
7. Acknowledgements	86
8. References	86

1. Introduction

Monitoring of snow avalanche in natural field is very important to ensure the safety around snowy mountains which have a potential risk of avalanche to infrastructures and recreational users.

Mt. Fuji is a huge stratovolcano characterized by long slopes. It has many snow avalanches in winter seasons, which frequently cause damages to the infrastructures (Anma et al., 1988, Anma, 2007 and Tanaka et al., 2008). It is subject to an additional risk of snow avalanches in case the volcano becomes active. Flows due to melting snowpack by magma make a type of the biggest volcanic hazards at high-altitude volcanoes (e.g., Pierson et al., 1990). Therefore, it is highly needed to develop a method to monitor snow avalanche at high-altitude volcanoes including Mt. Fuji. However, monitoring a high-altitude mountain is not easy, especially during winters, due to the poor accessibility and visibility, limited power supply, and severe conditions. Moreover, the avalanche paths are distributed in many directions in wide areas because of the volcano's conical shape.

In this study, we installed infrasound microphones and seismometers at the Mt. Fuji for 2 winter seasons and aimed to detect the snow avalanches only by monitoring the infrasonic and seismic signals. Besides, we also installed the thermometer probes and measured the snow depth. We evaluated the practicality of using the infrasonic and seismic method and the thermometer probes in the sever mountain. Based on the results from the observations and data analyses for the two winters, we propose a snow-avalanche monitoring system suitable for Mt. Fuji.

1-1 Infrasound and Seismic Observations

These days, most of the avalanche reports are based on the information by surveillance cameras and encounters. Therefore, we tend to observe the avalanches during the daytime in fine weather better than in rough weather or during the night because of poor visibility and few people in the field. To improve this bias, avalanche monitoring by infrasound microphones (Marchetti et al. 2015, Scott et al. 2007, Ulivieri et al. 2011, Arai et al. 2017), by seismometers (Heck et al. 2019, Perez-Guillen et al. 2019, Lacroix et al., 2012) or by both infrasound microphones and seismometers (Marchetti et al. 2020, Kogelnig et al. 2011) were carried out recently. With these methods, it is expected to monitor the avalanches regardless of weather conditions, visibility and witnesses.

Most of those previous studies were carried in experimental fields or valleys where they already knew the exact avalanche slopes (Marchetti et al. 2020, Koelning et al. 2011) or they artificially triggered the avalanches by explosive (Scott et al. 2007, Ulivieri et al. 2011). Studies targeting natural snow avalanches in wide areas of snowy mountains are still limited (Arai et al. 2017, Pérez-Guillén et al. 2019 etc.). A short review of these studies is given below.

<Infrasonic Observation>

Scott et al. (2007) installed the infrasound array of 7 microphones (5 were placed linearly with a relative distance of 40 m and 2 were placed roughly 300 m away from each other) around 675 m away from the avalanche paths and measured the signals of dry-snow avalanches which were triggered by the explosions in the avalanche control. In the study, the size of the avalanche was mostly size-class 2 and they run hundreds of others down highly vertical terrain toward the array. The infrasound signals in the frequency band of 0.1-8.5 Hz were analyzed and reported that the avalanche signals are concentrated around 4 Hz and that the duration time and amplitude of avalanches is 20-40 s and 0.5-1.5 Pa respectively.

Marchetti et al. (2015) performed the observation of avalanches by an infrasound array with 4 microphones (placed in triangular-shape with a relative distance of 150 m) in the aim of automatic avalanche detection by the infrasound array. The array was installed in a flat area approximately 1 km away from the avalanche paths. They reported that they successfully detected signals of several dry snow avalanches and estimated the back-azimuths and apparent velocities of those signals. The durations of infrasonic signals were 60-120 s, and their amplitudes were 0.3-1.0 Pa in the frequency band of 0.5-20 Hz.

Ulivieri et al. (2011) observed the infrasound signals of natural snow avalanches and those triggered by explosions using an infrasound array in the frequency band of 0.8-12 Hz. The installation site was around 2 km away from the avalanche slopes where the avalanche controls were carried out frequently. The array had 4 elements with a triangular geometry and an aperture of about 150 m. Through the observation, they detected 5 artificially-triggered avalanches consisting of 4 small loose snow avalanches and one small- to medium-sized snow slab avalanches. They reported that those avalanches had durations of 5-40 s, amplitudes of around 0.5 Pa, and frequency bands of 1-10 Hz. Besides, they searched for infrasound signals of natural avalanches in the data by the same

infrasound array. They extracted 146 candidate signals in 1 winter season, though they could not confirm those data as the avalanches by supplemental information such as visual data.

Arai et al. (2017) installed three high-precision barometers spaced by 1-2 km in triangular-shape in roughly 1 km away from the avalanche slopes with the sampling rate of 100 Hz. They reported that they were able to locate 12 infrasound signals, possibly associated with snow avalanches in a winter season, and their amplitudes and duration times were about 0.5 Pa and about 60 s, respectively.

<Seismic Observation>

In the observation by Heck et al. (2018), they installed a seismic array (7 vertical geophones with a relative distance of 30 m) approximately 500 m away from avalanche paths to identify the direction of avalanche signals. Twenty-four seismic signals of dry-snow avalanches released in the middle and after a storm (those signals were confirmed to be avalanches by the visual information after the storm) were analyzed in the frequency band of 5-40 Hz. According to their report, the main frequencies of the seismic signals by the avalanches were 5-40 Hz, the duration times were 30- 120 s, and the amplitudes were about $2.0e-6$ m/s.

Lacroix et al. (2012) also installed the seismic array (7 seismometers with a relative distance of 45 m) about 1-5 km from the avalanche paths to estimate the location and the speed of avalanches and to find the relationship between avalanche occurrences and meteorological variables. In their report, the main frequency band of seismic signals was 1-10 Hz and duration times were 20-120s.

In the avalanche observation carried out by Pérez-Guillén et al. (2019), they analyzed the data of seismic network in Mt. Fuji. Their test site was almost the same as this research and they observed the avalanches on mainly North-West side of Mt. Fuji by the seismic network in the winters of 2014, 2016 and 2018. The frequency band used in this analysis is 1-45 Hz. During their observation, they detected 7 avalanche signals. Among those 7 signals, 4 were confirmed to be the avalanches by the visual information and those were relatively big avalanches (size class 3 to 5). One of them was a slush flow (highly water-saturated avalanches) and other 3 events were snow avalanches. The distances between the seismic stations and the avalanche slopes were roughly 1-4 km; which are almost the

same as our observations. According to their reports, the amplitudes of the seismic signals were from $1.5e-5$ m/s to $1.0e-4$ m/s in maximum and the signals had high power in the frequency band of 3-30 Hz. Duration of those signals were about 60-180 s.

<Infrasonic and Seismic Observation>

Koelning et al. (2011) installed 1 infrasound microphone in front of the avalanche test site and 4 seismometers along with and in front of the avalanche test site (the Vallée de la Sionne) and measured the 4 dry-snow avalanches whose size were between size class 3 to 5. The data were analyzed in the frequency band of 1-40 Hz. Base on their report, the main frequencies of the infrasonic signals were 1-6 Hz and those of the seismic signals were 4-12 Hz. The amplitudes of the seismic and infrasonic signals were $2.0e-4$ ~ $1.0e-6$ m/s and 0.7-5 Pa, respectively. Duration times of those signals were 80-300 s depending on the property and size of the avalanches.

Marchetti et al. (2020) installed both infrasonic and seismic arrays (5 infrasound sensors with the aperture of 160 m and 7 seismometers with the aperture of 75 m) in a flat area surrounded by the mountains and analyzed the signals released by a dry-snow avalanche. The distance between the infrasonic array and the seismic array was approximately 200 m. In their study, the spectral power of the infrasonic signal was concentrated in 0.5-8 Hz with a peak at 3.4 Hz. On the contrary, the seismic power was in 3.5-12 Hz with the peak frequency around 6 Hz, which was sharper than the spectral peak of the infrasonic signal. The observed duration time of infrasonic signals (~45 s) was shorter than that of seismic signals (~60 s).

Kogelnig et al. (2011) presented that avalanches generate both infrasound and seismic waves from different flow regimes. They pointed out that the infrasound sensors could detect avalanche initiation while the seismic sensors could detect the stopping phase of an avalanche. Similarly, Marchetti et al. (2020) showed that seismic energy was radiated all along the avalanche path, from the initiation to the deposition area, while infrasound is only from the powder cloud. These are two of the few studies that combined infrasonic and seismic data from snow avalanches. Since infrasound microphones and seismometers record both infrasonic and seismic waves (Cannata et al. 2013, Ichihara et al., 2011, Watada et al. 2006), the separation of infrasonic signal and seismic signal is important to analyze the property of an avalanche from its signal. The use of arrays allows to distinguish the wave types (Marchetti et al., 2020; Heck et al., 2019). Alternatively,

Kurokawa and Ichihara (2020) proposed methods to distinguish seismic wave and infrasound wave by comparing the power spectra of data by a single seismometer and a collocated infrasound microphone.

In this study, we set infrasonic and seismic sensors around Mt. Fuji for two winter seasons (2018-2019 and 2019-2020). We used signals detected by the multiple sensors to identify events and estimate the direction of sources by calculating the delay of signals. We also compared the power spectra between the data recorded by an infrasonic sensor and a collocated seismometer for each event to distinguish seismic signals and infrasonic signals and to determine the location and the type of the avalanche.

1-2 Thermometer Probe

Continuous monitoring of the snowfall and the snow layer structures are useful to estimate the stability of snow cover (Steinkogler et al., 2014, Gascón et al., 2015, Schattan et al., 2017). Several methods to measure the snowfalls have been proposed and practiced in the real field. The laser snow gages are the most typical instruments. However, they are heavy and expensive and need electric power, which makes it difficult to monitor the snowfall under severe environments and at several points. Regarding to the snow-layer structure, the information is mainly based on the occasional field surveys (Schweizer and Jamieson, 2000) and numerical simulations (Steinkogler et al., 2014, Bartelt and Lehning, 2002).

Fujihara et al. (2015, 2017) proposed a new idea to estimate the snowfall in a less expensive and easier way. They used small temperature loggers attached to poles with 20 cm interval from the ground surface, which we call as “thermometer probe” hereafter in this study. Variation of temperature recorded at each height was used to estimate the snowfall.

Thermometer probe can provide the information about not only snowfall, but also the snow-layer structures, weather conditions, and so on. Thus, in this study, we installed similar thermometer probes in the field and applied their method with some improvements. We combine the information of avalanches from the infrasound and seismic data and snow-depth from the thermometer probe to understand the relationship between avalanches and snow conditions.

2. Observation

2-0 Study Area

Mt. Fuji is a stratovolcano and the highest mountain in Japan (3776 m above sea level). Usually, snow covers the mountain slopes above 2000 m a.s.l. (Anma et al., 1988) during the winter to spring.

In this study, we selected the north side of Mt Fuji as the study area of the avalanche observation. As shown in Fig 2-0-1, Mt. Fuji has several clear valleys which have high potential to be the avalanche paths. We installed the instruments to observe the avalanches on those paths.

Observations were carried out in 2 winter seasons (2018-2019 and 2019-2020). Infrasound microphones, seismometers, and thermometer probes were installed to monitor the snow avalanches. Since setups of instruments differ depending on the seasons, here we describe the detailed installation respectively.

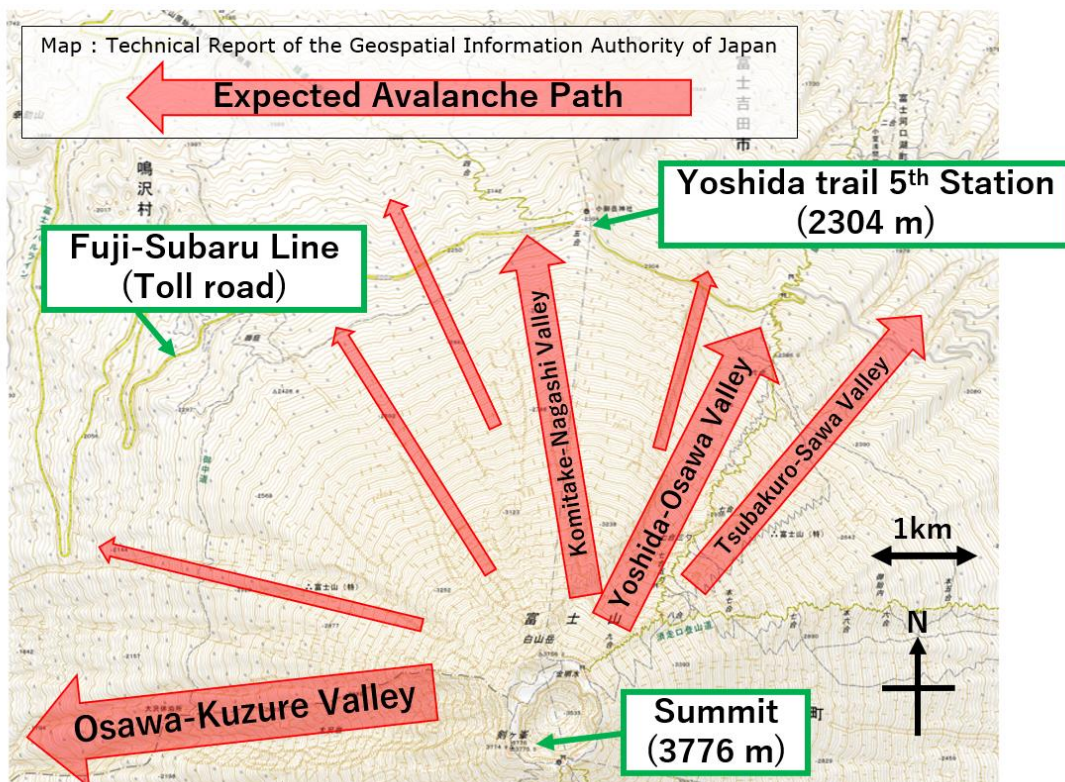


Fig 2-0-1. Topography and avalanche slopes on the north side of Mt. Fuji

2-1 2018-2019 Winter Season

2-1-1 Infrasound Microphones

We set two infrasonic stations (AKD and KMT in Fig 2-1-1) with a relative distance of 1 km, each of which consists of a pair of microphones separated about 10 m. The detailed locations of those stations are in Table 2-1-1 and the arrangements are in Fig 2-1-2.

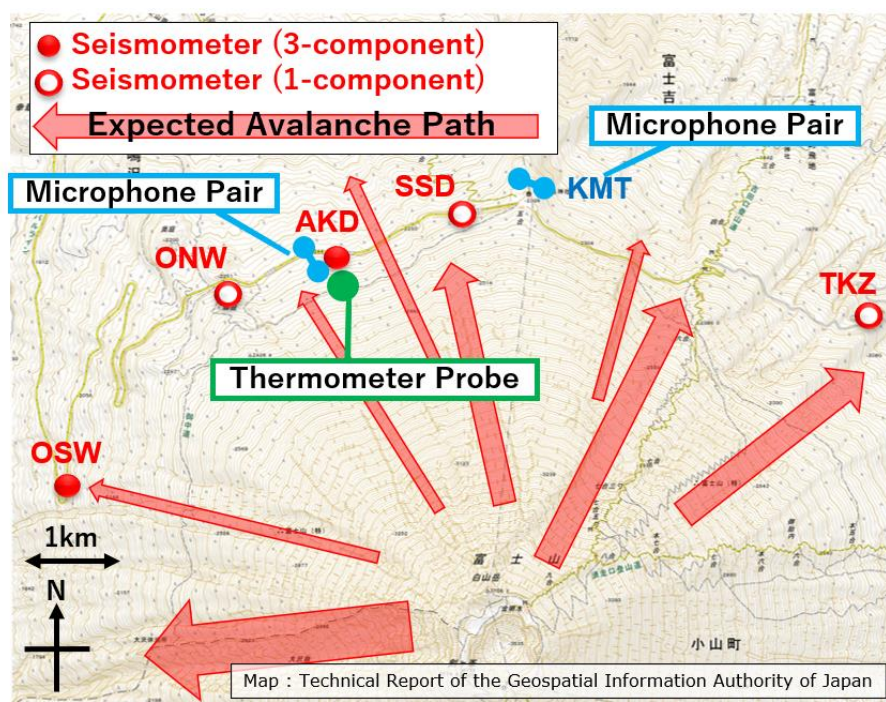


Fig 2-1-1. Locations of instruments in 2018-2019 winter season

We used two types of electric condenser microphones, both of which have flat responses in 0.3-2000 Hz and were sensible to signals below 0.01 Pa. The two at AKD and the one at KMT were SI104's manufactured by Hakusan Co.. The SI104 microphone had an advantage of low power consumption (<6 mA) but had relatively large electric noise (~0.1 Pa). The other one at KMT was a prototype of 7744N (No. 10647) developed by ACO Co.. It had low electric noise (<0.1 mPa according to the data sheet) with a power consumption of ~12 mA. The data were recorded by 24-bit data loggers, LS8800 (Hakusan Co.), at the sampling rate of 100 Hz with GPS time synchronization. The power consumption of the data logger was less than 17 mA. Each station was powered by three sealed batteries (SunXtender, PVX-840T). The detailed instruments used in this observation were summarized in Table 2-1-2. Before this observation, we measured the

same infrasonic signal by all the infrasound microphones used in this observation and verified that properties of those microphones have are the same in sensitivity, phase and amplitude in the target frequency band of 1-10 Hz. Besides, we also measured those properties of those microphones after the observation and checked that their properties had not been changed during the observation.

The observations were carried out from December 12th, 2018 to May 22nd, 2019.

Station Name	Latitude[N]			Latitude[N]			Altitude[m]	
	Degrees	Minutes	Seconds	Degrees	Minutes	Seconds		
OSW	35	23	19.12	138	42	30.71	2030	
ONW	35	23	18.76	138	42	20.37	2239	
AKD	seismometer	35	23	26.38	138	43	0.58	2245
	microphone	35	23	26.32	138	42	59.81	2270
SSD	35	23	37.42	138	43	44.56	2281	
KMT	35	23	38.76	138	44	1.79	2308	
TKZ	35	23	6.71	138	45	52.66	2008	

Table 2-1-1. Location and the name of the station on 2018-2019 winter season

Station name	Sampling Frequency [Hz]	A/D resolution	Senor	Component	Sensitivity	Unit of sensitivity	Logger	1LSB voltage [V]	Date of Installation	Date of removal
OSW	100	24	LE3D Mk3	UD	800.00	V/m/s	LS7000XT	3.22465E-06	2018/12/21	2019/4/19
	100	24	LE3D Mk3	NS	800.00			3.22465E-06		
	100	24	LE3D Mk3	EW	800.00			3.22465E-06		
ONW	100	18	L22D	UD	70.00	V/m/s	EDR-X1000	7.60000E-08	2018/12/12	2019/5/22
AKD	100	27	LE3D Mk3	UD	800.00	V/m/s	HKS9700	3.07047E-07	2019/2/3	2019/5/22
	100	27	LE3D Mk3	NS	800.00			3.07047E-07		
	100	27	LE3D Mk3	EW	800.00			3.07047E-07		
	100	24	SI104	ch1	9.80E-04	V/Pa	LS8800	6.25850E-07	2018/12/12	2019/5/22
100	24	SI104	ch2	9.90E-04	V/Pa	LS8800	6.25850E-07	2018/12/12	2019/5/22	
SSD	100	18	L22D	UD	70.00	V/m/s	EDR-X1000	7.60000E-08	2018/12/12	2019/5/22
KMT	100	24	ACO	ch1	8.30E-03	V/Pa	LS8800	6.25850E-07	2018/12/12	2019/5/22
	100	24	SI104	ch2	9.60E-04			6.25850E-07		
TKZ	100	18	L22D	UD	70.00	V/m/s	EDR-X1000	7.60000E-08	2018/12/12	2019/5/22

Table 2-1-2. List of instruments used in the observation on 2018-2019 winter season

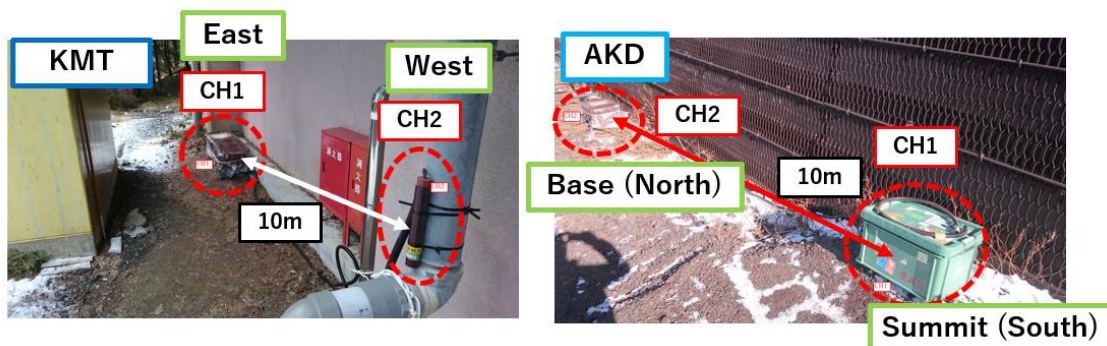


Fig 2-1-2. Installation of infrasound microphones at KMT (Left) and AKD (Right)

2-1-2 Seismometers

Two 3-component seismometers and three 1-component seismometers were installed along with the infrasound microphone arrays by a research group consisting of Mt. Fuji Research Institute, Hokkaido University, and Earthquake Research Institute. The station locations were OSW (3-component), AKD (3-component), ONW (1-component), SSD (1-component) and TKZ (1-component) as shown in Fig 2-1-1. The detailed locations of those stations are in Table 2-1-1.

The 3-component seismometers used were LE-3Dlite MkIII (Lennartz Electronic) with a natural frequency of 1 Hz and a sensitivity of 800.00 V/m/s. The 1-component seismometers used were L-22D (Sercel Inc.) with a natural frequency of 2 Hz and a sensitivity of 70.00 V/m/s. The 3-component data were recorded by a 24-bit data logger, LS-7000XT (Hakusan Co., 100-150 mA) at OSW and an HKS9700 data logger (Keisoku Giken Co., <0.15 W) with a 27-bit resolution at AKD. The 1-component data were recorded by low-power consumption data loggers, EDR-X1000 (Kinkei System Co., 6 mA) with an 18-bit resolution. All the stations were operated at the sampling rate of 100 Hz with GPS time synchronization.

As the Table 2-1-2 shows, the observations were carried out from December 21st, 2018 to April 19th, 2019 at OSW and from December 12th, 2018 to May 22nd, 2019 at ONW, SSD and TKZ. At AKD station, observations were carried out from February 3rd, 2019 to May 22nd, 2019 and both infrasonic and seismic sensors were operated.

2-1-3 Thermometer Probe

We installed a probe-like thermometer that had three elements in vertical 40-cm grids next to the infrasonic sensors in AKD to measure the temperature and snow condition (Fig 2-1-3). Compact waterproof temperature loggers (TR-52i, T&D Co., Range -60 to 155 °C, Accuracy ± 0.3 °C) were attached to a wood pole. We used wood because of its low thermal conductivity. As the logger could store 16,000 data points, the temperature was recorded every 15 minutes from January 10th, 2019 to May 22nd, 2019.

Before the field installation, we calibrated the thermometers in still water with ice in it for 20 minutes recording every 10 seconds. The average temperature recorded in those thermometers showed the offset of measurement on each thermometer due to the

individual difference, and the offsets were 0.1 °C, -0.2°C and 0.2°C on the thermometers at the height of 0 cm, 40 cm and 80 cm individually. The offsets were within the accuracy of the thermometers. For the analysis, we subtract the bias from the result to correct the individual difference.

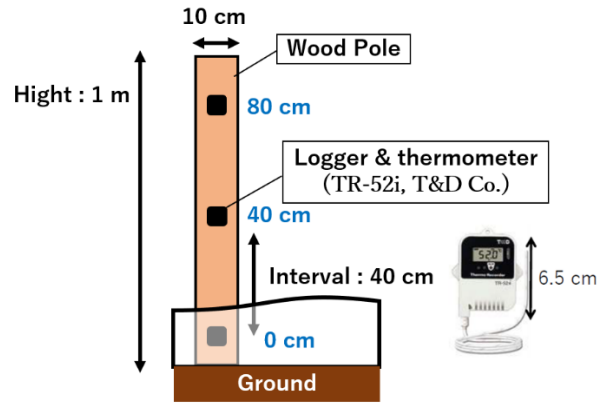


Fig 2-1-3. Thermometer probe used in the observation in 2018-2019 winter season

2-2 2019-2020 Winter Season

2-2-1 Infrasound Microphones

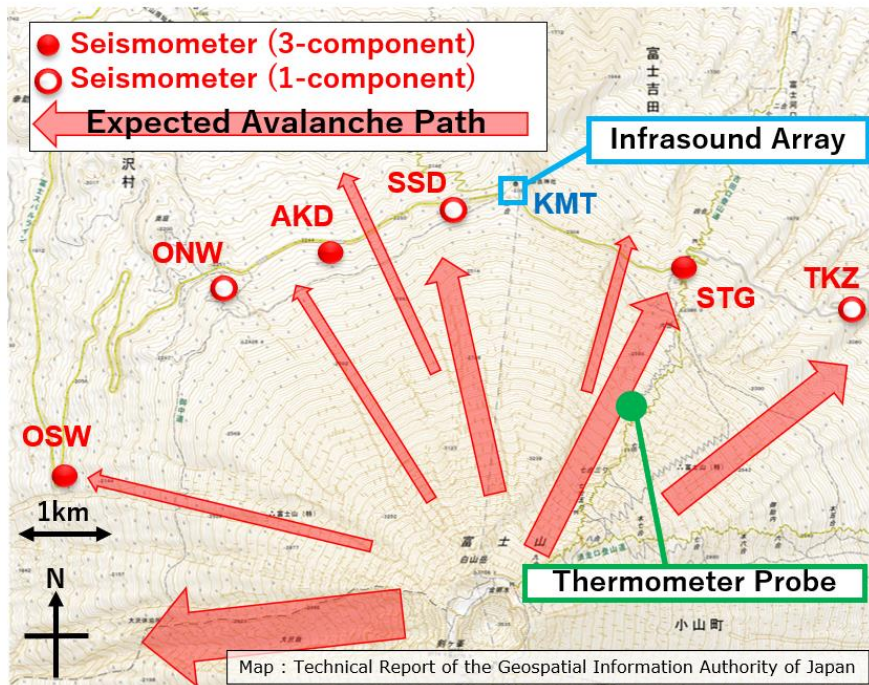


Fig 2-2-1. Locations of instruments in 2018-2019 winter season

In this winter, a 5 m-scale array with 3 elements (hereinafter, this 3 m-scale array is called “S-array”) and a 200 m-scale array with 4 elements (hereinafter, this array is called “L-array”) were installed at KMT as shown in Fig 2-2-1 and Fig 2-2-2. CH1 of S-array and CH2 of L-array were common. Detailed information of their locations is in Table 2-2-1.

The prototypes of 7744N microphones developed by ACO Co. were used in L-array (No. 10326, No. 10607, No. 10646, and No. 10654). The specifications were the same as the ACO microphone used in 2018-2019. CH2 and CH3 of the S-array used high-sensitivity MEMS infrasound sensors, which were designed to have flat responses above 1 Hz (Wada and Takahashi, 2020). The data were recorded by the data loggers LS8800 at the sampling rate of 100 Hz with GPS time synchronization. Table 2-2-2 summarizes the detailed properties of the instruments. Like the observation in the previous winter season, we tested the properties of all infrasound microphones before and after the observation and confirmed that those microphones were the same in sensitivity, phase and amplitude in the target frequency band of 1-10 Hz.

The observations were carried out from November 11th, 2019 to May 28th, 2020 at L-array and from December 20th, 2019 to May 28th, 2020 at S-array.

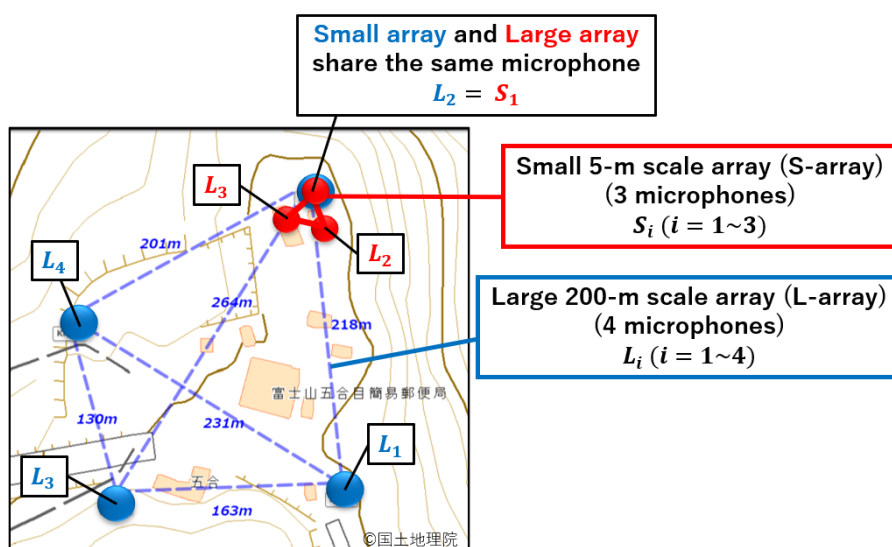


Fig 2-2-2. Locations of instruments in 2018-2019 winter season

Station Name	Latitude[N]			Latitude[N]			Altitude[m]	
	Degrees	Minutes	Seconds	Degrees	Minutes	Seconds		
OSW	35	23	19.12	138	42	30.71	2030	
ONW	35	23	18.76	138	42	20.37	2239	
AKD	35	23	26.38	138	43	0.58	2245	
SSD	35	23	37.42	138	43	44.56	2281	
KMT	KMT1	35	23	38.08	138	44	1.83	2300
	KMT2	35	23	45.29	138	44	0.86	2278
	KMT3	35	23	38.2	138	43	54.57	2266
	KMT4	35	23	41.92	138	43	53.75	2285
STG	35	23	20.24	138	44	52.47	2228	
TKZ	35	23	6.71	138	45	52.66	2008	

Table 2-2-1. Location and the name of the station on 2019-2020 winter season

Station name	Sampling Frequency [Hz]	A/D resolution	Senor	Component	Sensitivity	Unit of sensitivity	Logger	1LSB voltage [V]	Date of Installation	Date of removal
OSW	100	24	LE3D Mk3	UD	800.00	V/m/s	LS7000XT	3.22465E-06	2019/11/13	2020/5/28
	100	24	LE3D Mk3	NS	800.00			3.22465E-06		
	100	24	LE3D Mk3	EW	800.00			3.22465E-06		
ONW	100	18	L22D	UD	70.00	V/m/s	EDR-X1000	7.60000E-08	2019/11/13	2020/5/28
AKD	100	27	LE3D Mk3	UD	800.00	V/m/s	HKS9700	3.07047E-07	2019/11/13	2020/5/28
	100	27	LE3D Mk3	NS	800.00			3.07047E-07		
	100	27	LE3D Mk3	EW	800.00			3.07047E-07		
SSD	100	18	L22D	UD	70.00	V/m/s	EDR-X1000	7.60000E-08	2019/11/13	2020/5/28
KMT	L1	100	7744N	ch1	9.77E-03	V/Pa	LS8800	6.26E-07	2019/11/11	2020/5/28
	L2(S1)	100	7744N	ch1	8.30E-03	V/Pa	LS8800	6.26E-07	2019/11/11	
	S2	100	MEMS	ch2	4.00E-02	V/Pa		6.26E-07	2019/12/20	
	S3	100	MEMS	ch3	4.00E-02	V/Pa		6.26E-07	2019/12/20	
	L3	100	7744N	ch1	8.10E-03	V/Pa		LS8800	6.26E-07	
L4	100	7744N	ch1	6.20E-03	V/Pa	LS8800		6.26E-07	2019/11/11	
STG	100	27	LE3D Mk3	UD	800.00	V/m/s	HKS-9700	2.45600E-06	2019/11/13	2020/5/28
	100	27	LE3D Mk3	NS	800.00			2.45600E-06		
	100	27	LE3D Mk3	EW	800.00			2.45600E-06		
TKZ	100	18	L22D	UD	70.00	V/m/s	EDR-X1000	7.60000E-08	2019/11/13	2020/5/28

Table 2-2-2. List of instruments used in the observation on 2019-2020 winter season

2-2-2 Seismometers

Two 3-component seismometers and three 1-component seismometers were installed. Detailed setup was almost the same as that in 2018-2019 winter season, but a 3-component seismometer (LE-3Dlite MkIII, Lennartz Electronic) was additionally installed at STG with an HKS-9700 data logger. The station locations were OSW(3-component), AKD (3-component), STG (3-component), ONW (1-component), SSD (1-component), and TKZ (1-component), as shown in Fig 2-2-1 and Table 2-2-1.

The observations were carried out from November 13th, 2019 to May 28th, 2020.

2-2-3 Thermometer probe

Two thermometer probes were used to record the temperature and snow depth. Each thermometer probe had 10 elements in vertical 20-cm grids (Fig 2-2-3). The probes were installed close to the bottom of the Yoshida-Osawa Valley (2730m a.s.l.) right next to the 7th step of Mt. Fuji Yoshida trail. The probes were attached to the levees, which had been constructed to protect the trail from the avalanches, with a relative distance of 10 m. Ten of the probe elements (the lowest seven of Probe 1 and the upper three of Probe 2) were digital temperature loggers (TR-52i, T&D Co.) like last year. They recorded temperature every 10 minutes from November 2019 to March 2020 until the data capacity became full. The other tens were the older types but failed to record the data.

Before the field installation, we calibrated the thermometers in still water with ice in it for 20 minutes recording every 10 seconds like the last year and the shifts are between -0.2 °C to 0.3 °C. For the analysis, we subtract the bias from the result to correct the individual difference.

Besides, the Mt. Fuji Research Institute installed an automatic meteorological station 20 m away from the thermometer probes (Fig 2-2-5) and recorded the air temperature, snowfall, and winds (the maximum and average speeds and direction) every 1 hour. Snow depth was measured by KADEC 21-SNOW (North One Co.) (Fig 2-2-4).

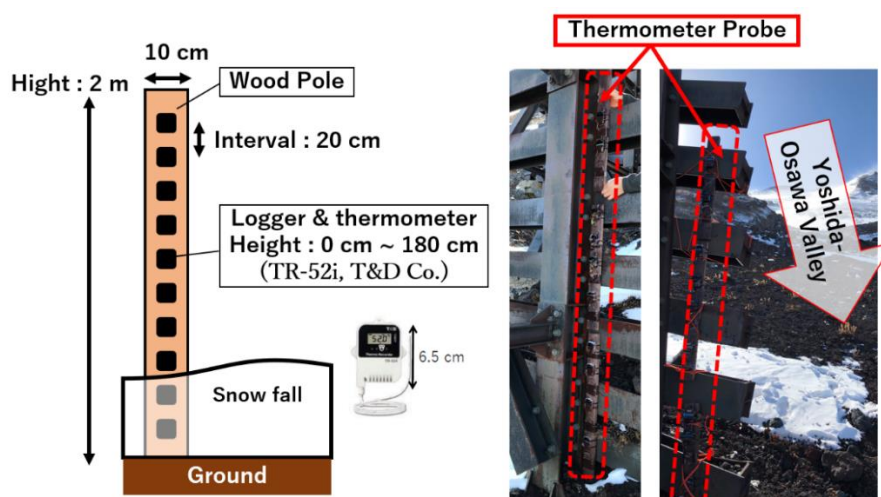


Fig 2-2-3. Thermometer probe in the observation in 2019-2020 winter season (left), Installation of thermometer probes in the field (right)

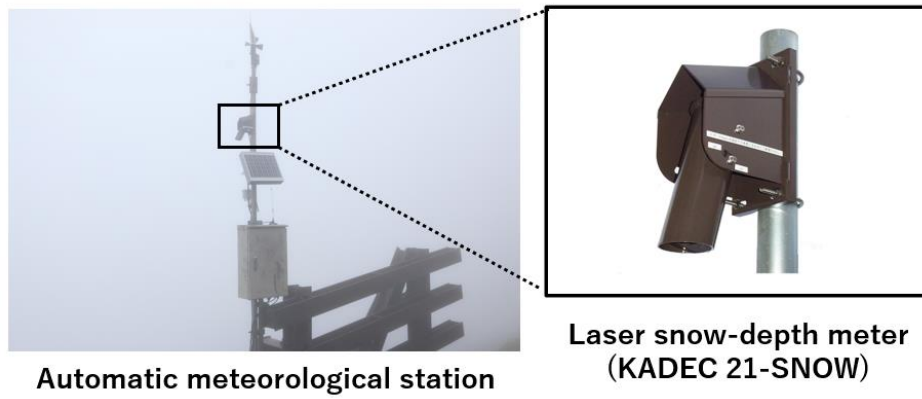


Fig 2-2-4. The automatic meteorological station and the snow-depth meter

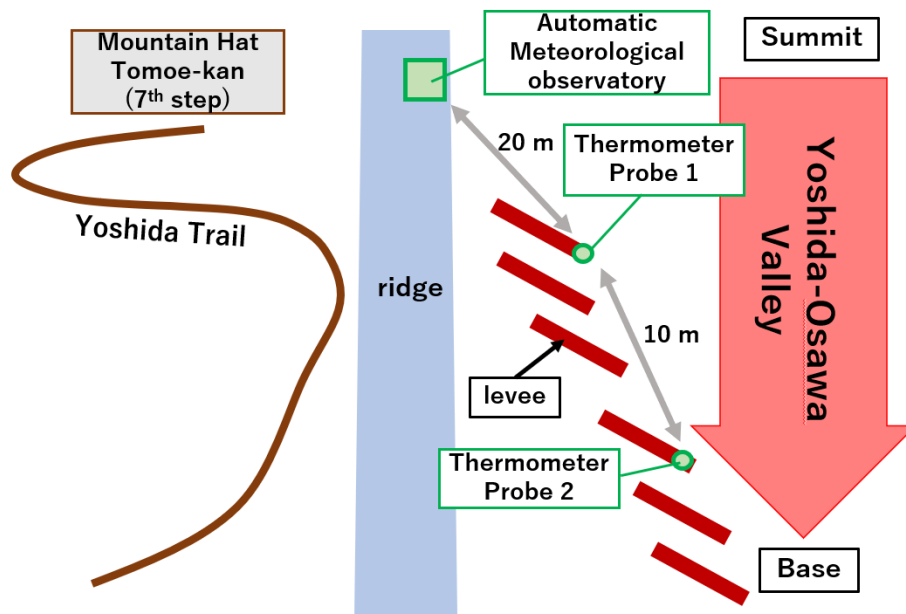


Fig 2-2-5. Arrangement of thermometer probes in 2019-2020 winter season

3. Analysis

3-1 2018-2019 Winter Season

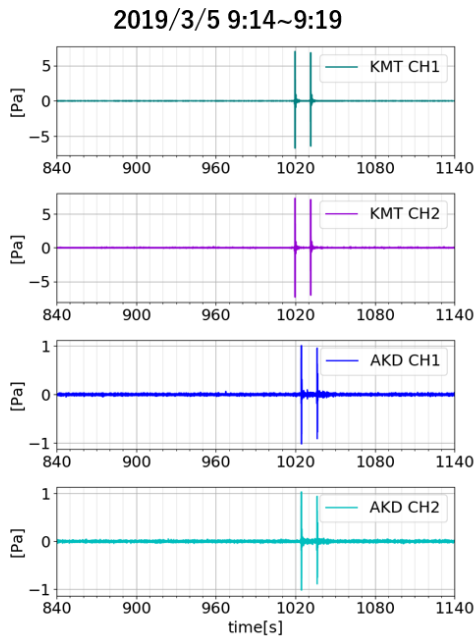
3-1-1 Infrasound Array

<Signal Detection>

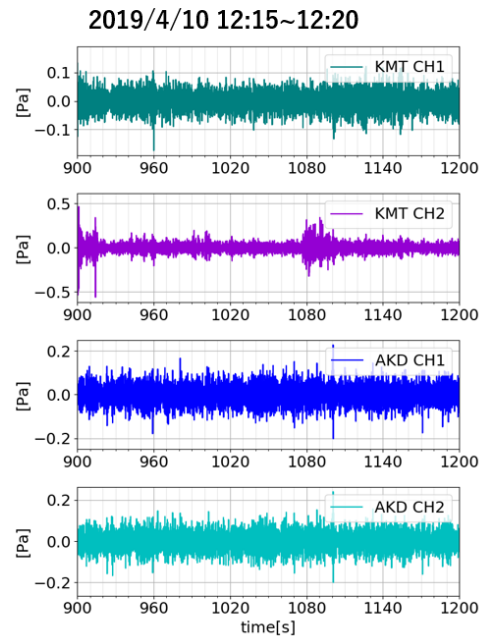
According to the previous studies (Scott et al. 2007, Ulivieri et al. 2011 etc.), it is reported that infrasound signals originated by the avalanches had a power in the frequency band of 1~10 Hz. Therefore, in the analysis of infrasound signals, the signals in the frequency band of 1-10 Hz were used to reduce the wind noise and observe the infrasound signals originated by avalanches.

We calculated the cross correlation of 1~10 Hz data in 2 microphones at AKD and KMT individually at every 20 seconds. Hereafter, we only use the cross-correlation coefficient (the normalized cross correlation function) and refer to it as 'CC.' The analysis effectively excluded the disturbances generated by wind from the infrasound signals because the two microphones were separated longer than the correlation lengths of the turbulent wind noise (Castano et al., 2020, Shields, 2005). The length of data to calculate the CC was 60 seconds which roughly matches the durations of infrasound signals by avalanches in previous studies (Koelning et al. 2011, Scott et al. 2007 etc.); they reported that durations of infrasound signals were from 20 s to 300 s depending on the properties and the size of avalanches. Then, we extracted events whose maximum correlation values were higher than 0.8 at both stations simultaneously. Lastly, we excluded (1) the infrasonic signals from exercises at the Japan Self-Defense Force training ground, (2) the continuous infrasound noises with no clear waveforms, and (3) earthquakes. Fig 3-1-1 shows the examples of waveforms on the excluded events on each infrasound microphones. Infrasonic signals from exercises at the Japan Self-Defense Force training ground (fig 3-1-1-(1)) had clear impulse-shaped waveforms with short duration and high amplitudes (higher than 0.5 Pa) and the number of those events was 12. Fig 3-1-1-(2) represents the example of the continuous infrasound noises with no clear waveforms. As this figure represents, there were no obvious waveform of avalanches which had a spindle-shaped envelope (Arai et al. 2017) on the data. The existence of continuous infrasound signals was revealed by the CC calculation. The number of those unclear infrasound signals was 13. Lastly, one earthquake was also picked by the method on January 14th, 2019 at 13:23.

(1) Signals from exercises at the Japan Self-Defense Force training ground

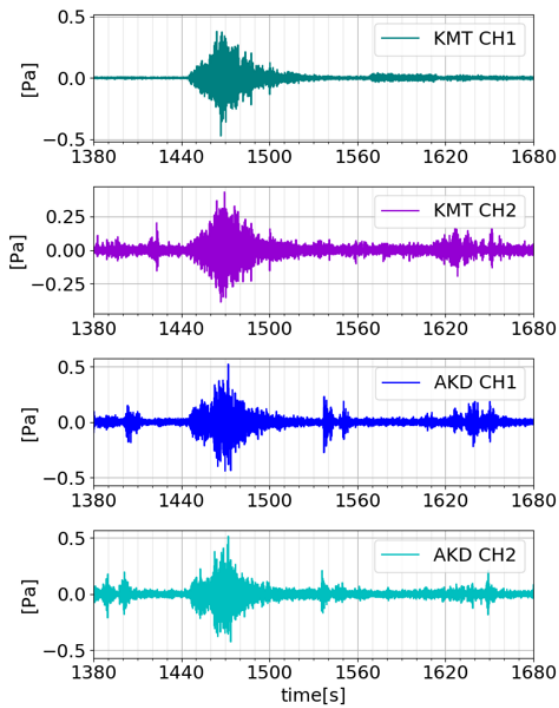


(2) Continuous infrasound noises with no clear waveform



(3) Earthquake 2019/1/14 13:23~13:28

Infrasound Microphones



Seismometers

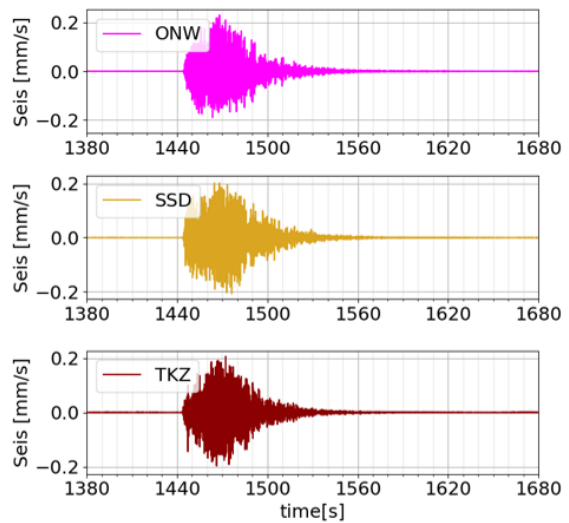


Fig 3-1-1. Waveforms of the detected events in infrasound microphones and seismometers

This earthquake was confirmed by the earthquake database of Japan Meteorological Agency. Fig 3-1-1-(3) shows the waveforms recorded in infrasound microphones and seismometers on this event. After those exclusion, 46 events were selected eventually.

<Distinction of Seismic and Infrasonic Signal>

In order to distinguish the seismic signals which were triggered by infrasound and by seismic wave, we analyzed the data of AKD where seismic and infrasonic sensors were both installed. This is because seismic sensors detect both seismic wave and infrasonic wave and vice versa. Accordingly, comparison of power spectral is essential to determine whether these signals were caused by seismic ground movement or by infrasonic wave (Kurokawa and Ichihara, 2020).

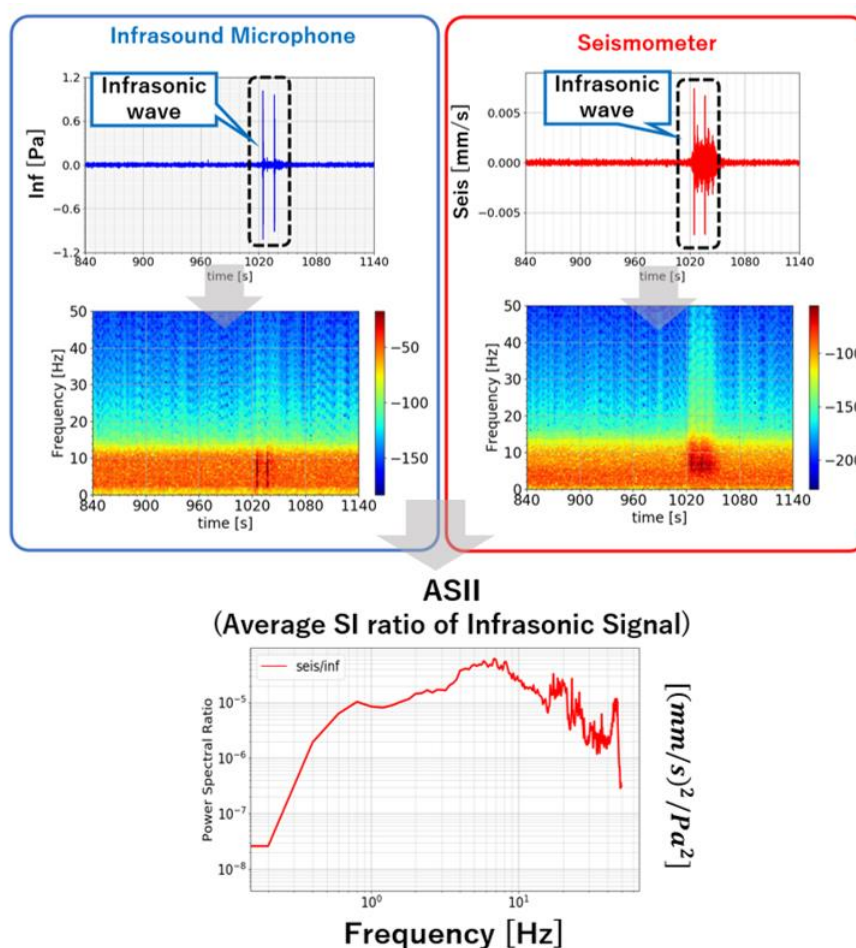


Fig 3-1-2. Waveforms and spectrograms of infrasound signals recorded in infrasound microphones and seismometers (top and middle) ASII (average SI ratio of infrasonic signal) (bottom)

First, we selected 12 samples which recorded artificial infrasonic waves from exercises at the Japan Self-Defense Force training ground. Second, power spectra of these infrasonic and seismic signals were calculated. Third, the power spectral ratio of seismic power to infrasonic power was obtained, which is denoted as “SI ratio” with the unit of $(\text{mm/s})^2/\text{Pa}^2$, hereafter. We averaged the SI ratios of the 12 samples, which we called “ASII” (Averaged SI of Infrasound), hereafter (Fig 3-1-2). ASII falls in the empirical range of the SI ratio, 10^{-8} – 10^{-4} $(\text{mm/s})^2/\text{Pa}^2$ (e.g., Langston 2004; Matoza and Fee 2014; Ichihara 2016; Kurokawa and Ichihara, 2020).

We normalized the SI ratio of the detected 41 events by the ASII (the 5 events from December 30th to January 30th were not analyzed because the seismometer was not installed at AKD during this period). If the seismic sensors recorded infrasonic waves, the normalized SI ratio should be close to 1. If the recorded signals were seismic waves, the it would be larger by orders (Kurokawa and Ichihara, 2020). By evaluating the normalized SI ratio, we can distinguish the types of recorded waves.

<Calculation Methods of Infrasound Visibility>

We are not always able to detect infrasound signals even with the array analyses signals because the microphone data are frequently dominated by wind noise. Castano et al. (2020) defined the ‘visibility’ of the infrasound to evaluate the ability to detect weak infrasound signals by microphones.

The ‘visibility’ of the infrasound is calculated from the mean-square values of microphone data. In this research, first, we applied the band-pass filter in the frequency band of 1-10 Hz to each station data, which was the same frequency band as we used to analyze the signals. Second, we calculated the mean-square value, namely the power, of the filtered data in every 60 seconds with the time window of 60 seconds. Third, we took the median of the power in every hour for each station. Figure 3-1-3 compares the power median values in all the time windows (red) and those in the time windows in which infrasound was recognized (purple). We found that most of the signals were detected when the power medians were smaller than $10^{-2.5}$ Pa^2 , which we employed as the threshold.

We evaluate the infrasound visibility, $V_i(t)$, at station i by

$$V_i(t) = \frac{N_i(t)}{60},$$

where $N_i(t)$ is the number of windows which had lower power median than $10^{-2.5} \text{ Pa}^2$ in every 1 hour (60 windows), and t indicates the beginning time of the 1-hour windows. Then, we evaluated the total infrasound visibility of the array, $V_{total}(t)$, as the average of visibilities over the array elements:

$$V_{total}(t) = \frac{1}{4} \sum_{i=1}^4 V_i(t).$$

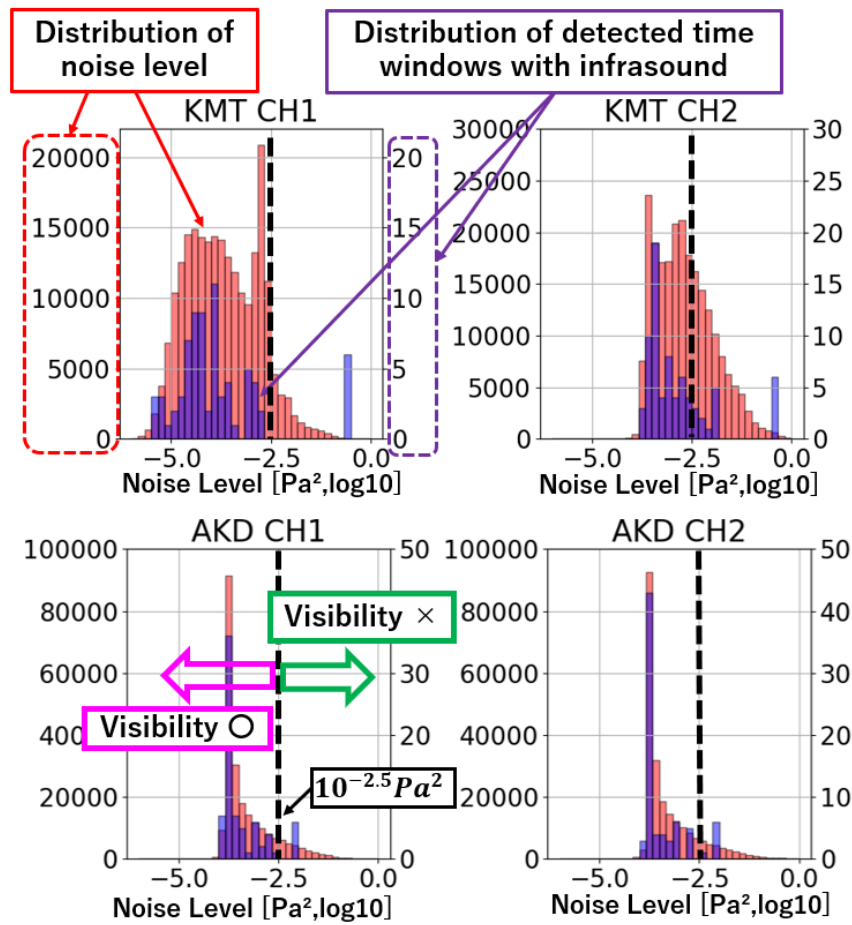


Fig 3-1-3. Distribution of the infrasound noise levels of all time (red) and the detected time windows with infrasound signals (purple) at AKD and KMT

3-1-2 Thermometer Probe

It is known that the fluctuation and diurnal changes of the temperature are smaller in the snow layer than in the air due to the low thermal diffusivity of snow, according to the previous studies (Kondou, 1994). As shown in Fig 3-1-4, the recorded temperature showed clear diurnal change when the thermometer was exposed to the air. On the contrary, it showed unclear diurnal changes under the snow cover. If the thermometer at 0 cm did not show the diurnal change while the others did, we estimated the snow depth was less than 40 cm (we here approximated as 20 cm). Similarly, if only the thermometers at 80 cm showed the diurnal change, snowfall was regarded to be approximately 60 cm. If none of thermometers showed the diurnal change, snowfall was assumed to be 100 cm. In this way, we could roughly estimate the snow depth by this simple method.

The snow-depth measurement with a thermometer probe was proposed by Fujihara et al., (2015,2017). They recorded thermal data at the sampling rate of 1 sample in 2 hours. They calculated the standard deviation of every 12 samples (1day) of each thermometer and regarded that it was covered by snow when the standard deviation was below a threshold value (0.3 °C).

We here used a similar measurement, but we recorded the data at 15-minute intervals. Then, we found that the first-order differentiations of the data were useful for distinguishing whether a thermometer was covered by snow or not. The detailed methods are as follows.

Fig 3-1-4 demonstrates the procedure of the thermal data analysis. Fig 3-1-4-(1) shows the original thermal data used for this analysis with a correction of the offset obtained by the calibration experiment. The first-order time differentiations (dT) exhibit the distinct differences between outside and inside the snow (Fig 3-1-4-(2)). The standard deviation of 12 samples in time scale (3 hours) at every 15 minutes by using first-order differentiations at each height shows how the thermal deviation in timescale changes (Fig 3-1-4-(3)). When the standard deviation is large, it means that the thermometer was above the snowpack. On the contrary, when the standard deviation is small, the thermometer was below the snowfall. The threshold value of the standard deviation was set to 0.4 °C. Then, the snow height was estimated as in Fig 3-1-4-(4).

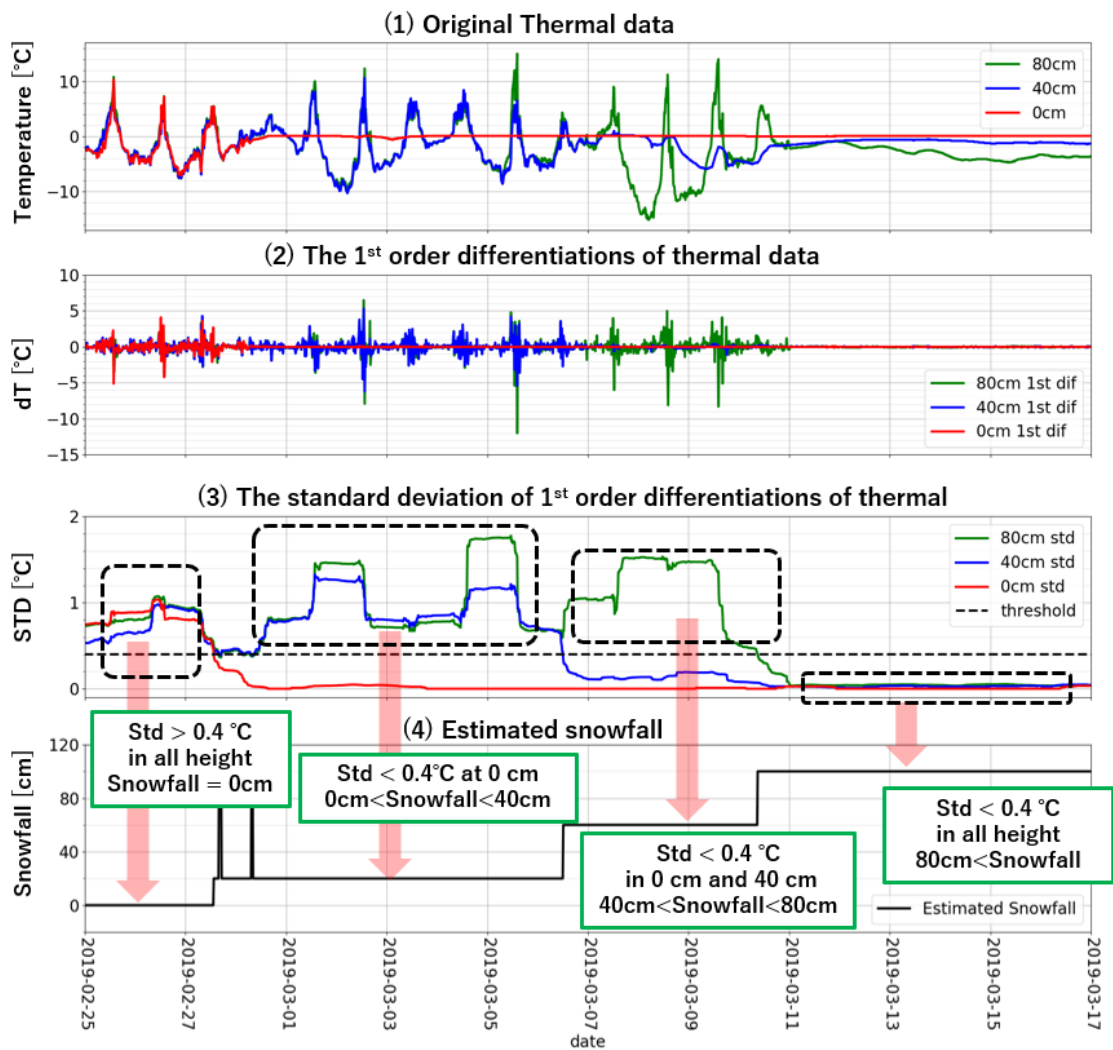


Fig 3-1-4. Results of the thermometer probe in the observation of 2018-2019 winter season

3-2 2019-2020 Winter Season

3-2-1 Infrasound

<Signal Detection>

Recorded infrasound data were analyzed in the frequency band of 1-10 Hz, in which we expect infrasonic power of snow-avalanche signals as mentioned in 1-1-1. We analyzed the data recorded by the microphones in both S-array (the 5 m-scale array with 3 elements) and L-array (the 200 m-scale array with 4 elements) as shown in Fig 3-2-1. The location of microphones in S-array and L-array were described $X_i^S (i = 1,2,3)$ and $X_i^L (i = 1,2,3,4)$, respectively, and the recorded data were denoted as $D_i^S(t) (i = 1\sim3)$ and $D_i^L(t) (i = 1\sim4)$, respectively.

- $X_i^S (i = 1,2,3)$: Location of microphones in S – array
- $X_i^L (i = 1,2,3,4)$: Location of microphones in L – array
- $D_i^S(t) (i = 1\sim3)$: Data of microphones in S – array
- $D_i^L(t) (i = 1,2,3,4)$: Data of microphones in L – array

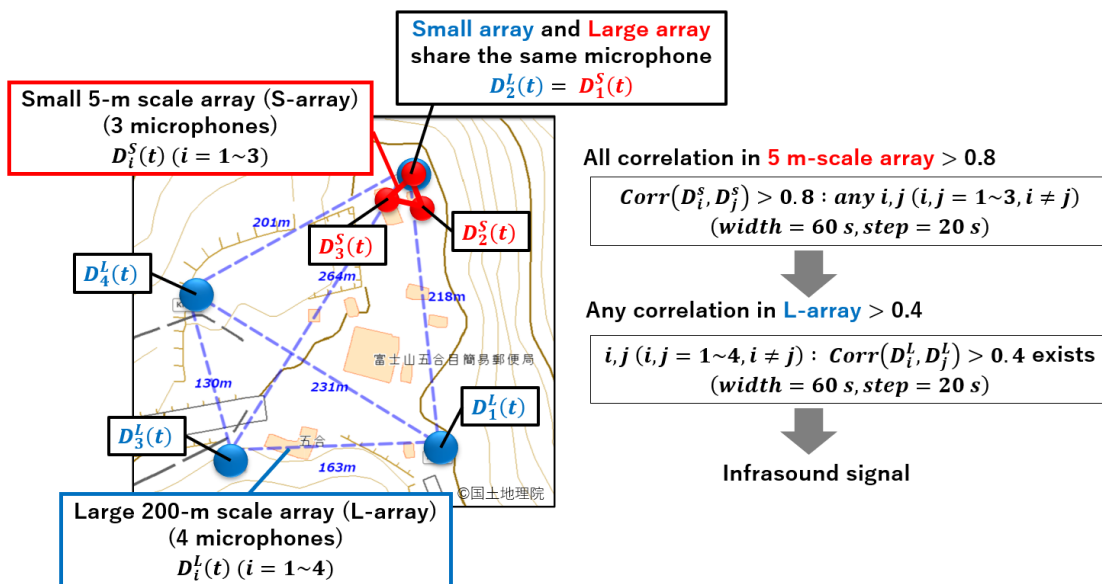


Fig 3-2-1. Installation of infrasound microphones in L-array (left) and Methods of signal detection (right)

First, we calculated the CCs with zero-shift between the elements in the S-array to discriminate between infrasound and wind noise. The length of data to calculate the CC was 60 seconds with time shift of 20 seconds, and the frequency band was 1-10 Hz. The time windows in which the CCs between all pairs of the three elements were higher than 0.8 were regarded to be the possible signal candidates. Second, to identify clear signals, the CCs between the 4 microphones in the L - array were also calculated on the candidate signals. The length of data to calculate the CC was also 60 seconds. If any of the CCs in the L - array was higher than 0.4, the candidate signals were accepted as infrasound signals. This threshold value of the CCs in the L – array was set to detect the clear infrasound signals and to reduce the misdetection of infrasound noise with no clear waveform. Consequently, it is possible that some infrasound signals by avalanches had been missed when the noise was high. Nevertheless, this threshold value enabled us to detect clear infrasound signals selectively, which made the analysis efficient and robust. After the selection above, the list of the time windows with infrasound signals was gained. Continuous time windows in this list were regarded to record the same infrasonic signals with long duration and the initial time of those continuous time windows were listed as the time of infrasound events. Third, the sources of infrasound signals were estimated on the events by using the following methods: “Minimizing Correlation Vector” and “Multi-Channel Semblance”. Detailed procedures of those methods are described below.

< Minimization of Correlation Vector >

This method computes the CC, $C_{ij}(t, \delta_d)$, between signals, $D_i^L(t)$ and $D_j^L(t)$ ($i, j = 1 \sim 4, i \neq j$) as a function of the initial time of the window, t , and delay δ_d ,

$$C_{ij}(t, \delta_d) = \text{Corr}(D_i^L(t), D_j^L(t), \delta_d).$$

As shown in Fig 3-2-2, Y-axis shows the relative delay time of $D_i^L(t)$ to $D_j^L(t)$ as δ_d . Namely, each vertical column of the image shows the CC between $D_i^L(t + \delta_d)$ and $D_j^L(t)$ as a function of δ_d . X-axis shows the initial time (t) of the time window to calculate the CC, and the color of this map indicates the value of $C_{ij}(t, \delta_d)$. We call this plot as “correlation map”. By using the correlation map, the relative delay time of signals was gained on each microphone pair (i and j) and time (t), which is denoted as $\tau'_{ij}(t)$.

Then, the correlation vector $\boldsymbol{\tau} \left(\tau_i = \left[\frac{1}{3} \sum_{\substack{j=1 \sim 4 \\ j \neq i}} (\tau'_{ij} - \tau'_{1j}) \right]_i \right)$ was also obtained. Here,

“relative” delay time of microphone pairs means the delay time of the arrival at \boldsymbol{x}_i^L relative to \boldsymbol{x}_1^L . For example, τ_2 (relative delay time at \boldsymbol{x}_2^L) is

$$\tau_2 = \frac{1}{3} \{(\tau'_{21} - \tau'_{11}) + (\tau'_{23} - \tau'_{13}) + (\tau'_{24} - \tau'_{14})\}$$

$$= \frac{1}{3} \{\tau'_{21} + (\tau'_{23} - \tau'_{13}) + (\tau'_{24} - \tau'_{14})\} (\because \tau'_{11} = 0)$$

Here, relative delay times (τ'_{ij}) of 5 microphone pairs (2 & 1, 2 & 3, 1 & 3, 2 & 4 and 1 & 4) were considered.

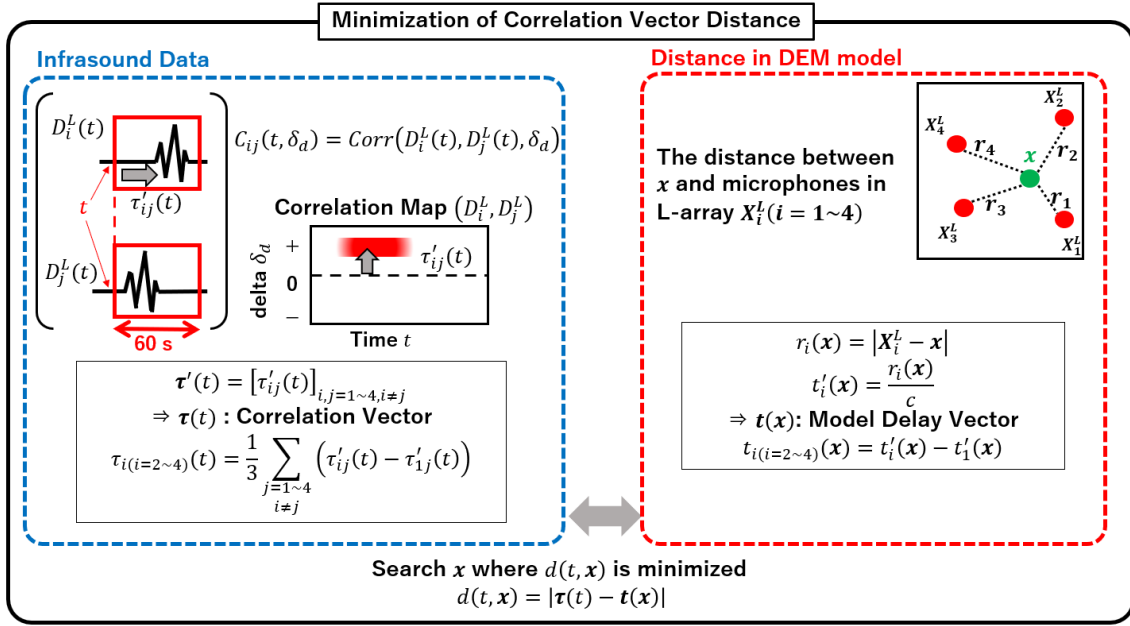


Fig 3-2-2. Minimization of correlation vector distance

On the other hand, the DEM data on Mt Fuji were available in the Technical Report of the Geospatial Information Authority of Japan website. Based on the DEM data, a hypothetical signal source x was set on the surface grids (32×32 grids with 305 m intervals) of the north side of Mt. Fuji and the theoretical distances between the source and microphones $r_i(x)$ were obtained. Then, the theoretical arrival time $t'_i(x)$ on each microphone was obtained by dividing $r_i(x)$ by the speed of sound c . In this study, the speed of sound was assumed to be constant as $c = 330 \text{ m/s}$. To compare with the correlation vector, we defined the model delay vector $\mathbf{t}(x)$ consisting of $t'_i(x) - t'_1(x)$, ($i = 2, 3, 4$).

By computing the distance, $d(t, x)$, between the correlation vector ($\tau(t)$) and the model delay vector ($\mathbf{t}(x)$) the possible signal source, x , was gained to minimize $d(t, x)$.

<Exclusion of Inconsistent Signals>

A simple way of excluding signals inside the L-array is using $T_{\text{delta}}(\mathbf{x})$, defined as the summation of the delay time lengths for the hypothetical source of infrasound at \mathbf{x} :

$$T_{\text{delta}}(\mathbf{x}) = \sum_{i=2\sim 4} \text{abs}(t'_i - t'_1)$$

Fig 3-2-3 indicates that $T_{\text{delta}}(\mathbf{x})$ is smaller when \mathbf{x} is inside the L-array than outside. The threshold value of $T_{\text{delta}}(\mathbf{x})$ was found to be 0.6 s.

For each of the selected infrasound events, we calculated the summation of the absolute values of the components in the correlation vector, τ_{delta} , as

$$\tau_{\text{delta}} = \sum_{i=2\sim 4} \text{abs}(\tau_i)$$

When $\tau_{\text{delta}} < 0.6$ s, we regarded the signal origin was inside the L-array and excluded the event from the candidate list of snow avalanche events.

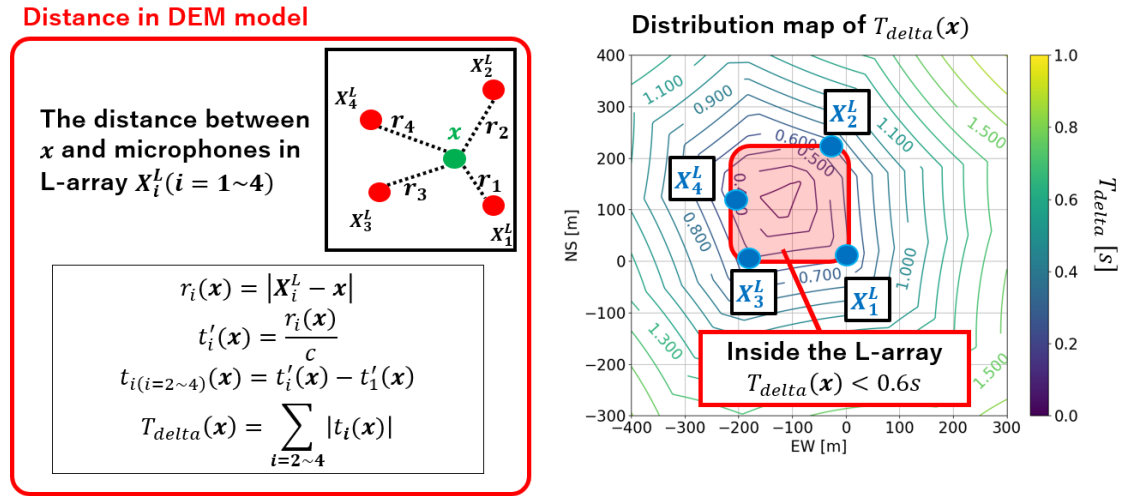


Fig 3-2-3. Methods of excluding the inconsistent signals

<Multi-Channel Semblance>

The other methods to estimate the source of infrasound is multi-channel semblance (Ripepe et al., 2007). Here, we first calculated the hypothetical delay time $t'_i(\mathbf{x})$ of each microphone by the same means as the minimization in correlation vector. Then, the CCs between those microphone pairs were re-computed. In this computation, the data $D_i^L(t)$ was shifted by $t'_i(\mathbf{x})$ for each microphone as $D_i^L(t + t'_i(\mathbf{x}))$ (Fig 3-2-4). Namely,

$D_i^L(t + t'_i(\mathbf{x}))$ is a 60-second-long time series starting from $t + t'_i(\mathbf{x})$. Thus, calculated CCs of microphone pairs (i, j) are the functions of t and \mathbf{x} and denoted as $S_{ij}(t, \mathbf{x})$. The summation of all microphone pairs $S(t, \mathbf{x})$ is the semblance, which is also the functions of t and \mathbf{x} . The location \mathbf{x} that maximized $S(t, \mathbf{x})$ was searched as the source of infrasound in this method.

In this research, this multi-channel semblance was used to identify the location of sources on the detected events. Length of signals to calculate the CC on infrasonic signals was 60 s and the semblance was calculated in every 5 s. The DEM data used was 305 m grid and numbers of grids in EW direction and in NS were both 32.

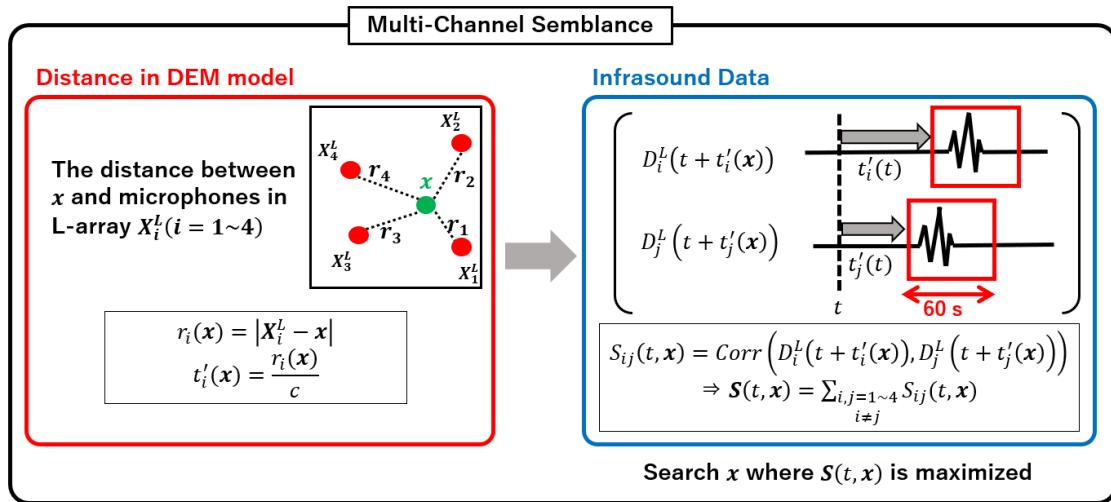


Fig 3-2-4. Multi-channel semblance

<Calculation Methods of Infrasound Visibility>

In the observation of 2019-2020 winter season, we also analyzed the visibility (see 3-1-1 for detail) of infrasound array. Fig 3-2-5 compares the power median values in all the time windows (red) and those in the time windows in which infrasound was recognized (purple) in the frequency band of 1-10 Hz. In this winter, we found that most of the signals were detected when the power medians were smaller than 10^{-4} Pa^2 , which we employed as the threshold.

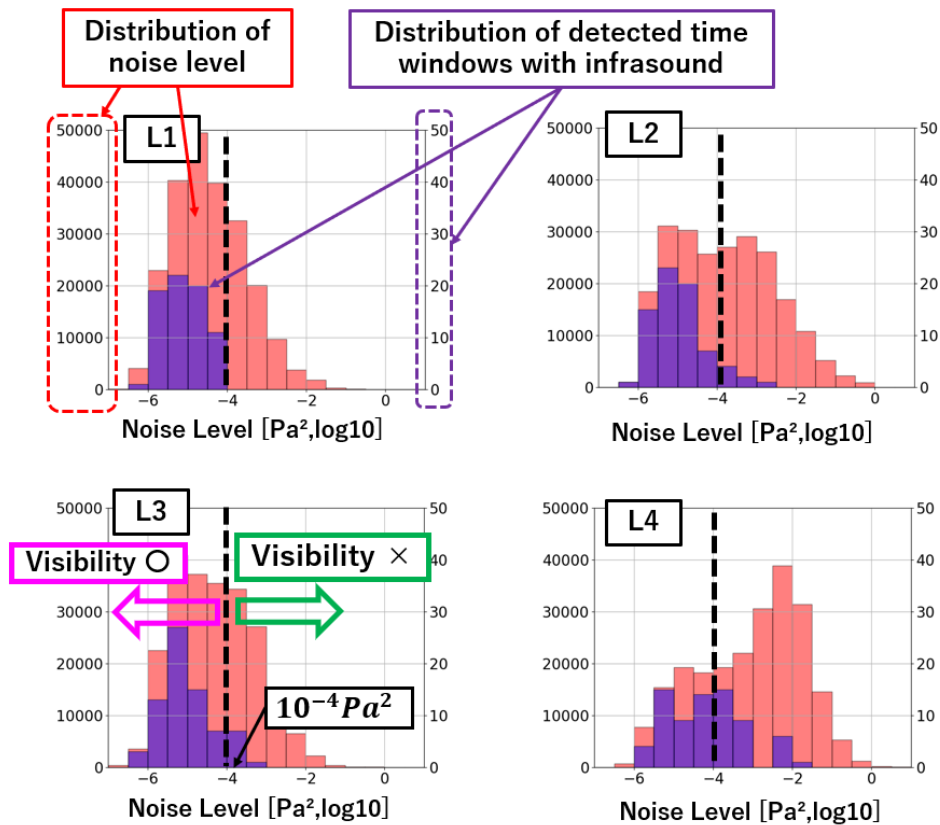


Fig 3-2-5. Distribution of the infrasound noise levels of all time (red) and the detected time windows with infrasound signals (purple) at 4 microphones in L-array

3-2-2 Wind Level

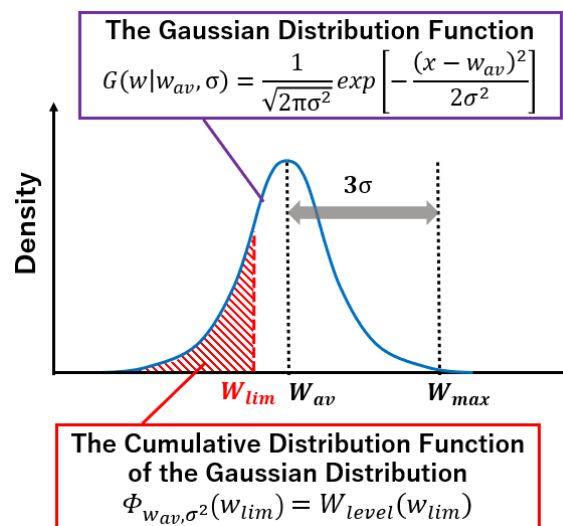


Fig 3-2-6. Wind level in the Gaussian distribution model

The average wind speed and the max wind speed had been recorded in every 1 hour at the meteorological station in the seventh step of Yoshida-Osawa trail. Since we did not have the distribution of wind-speed in 1 hour, we assumed the Gaussian distribution model, $G(w|w_{av}, \sigma)$, with the average w_{av} and the variance σ^2 (Fig 3-2-6) to evaluate a wind-level parameter, W_{level} , to compare with the infrasound visibility, V_{total} . In this model, we represented the max wind speed (w_{max}) by the 3σ -higher value than the average wind speed (w_{av}) as

$$w_{max} = w_{av} + 3\sigma.$$

Then, wind level, $W_{level}(w_{lim})$, was defined by the cumulative distribution function of the Gaussian distribution in $w < w_{lim}$ ($\Phi_{w_{av}, \sigma^2}(w_{lim})$), where w_{lim} is a threshold value. In this study, we used $w_{lim} = 8$ m/s.

3-2-3 Thermometer Probe

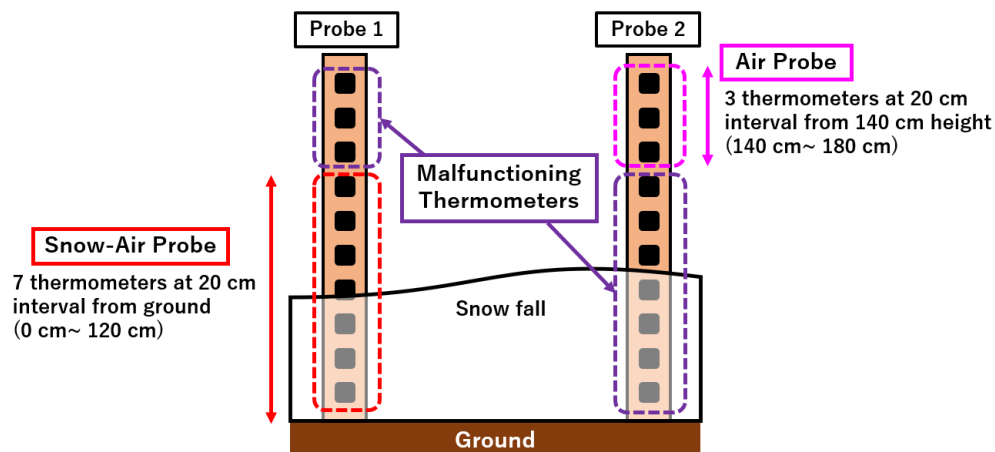


Fig 3-2-7. Model of thermometer probes in 2019-2020 winter season

Although we installed twenty thermometers in two probes, we had data from only ten due to the malfunction of the others (Fig 3-2-7). Among these ten successful thermometers, the seven were in one probe (described as “Probe 1” in Fig 3-2-7 and Fig 2-2-5), from 0 cm to 120 cm at the serial 20 cm intervals (this probe is called “Snow-Air Probe” hereafter). The other three were on another probe (described as “Probe 2” in Fig 3-2-7 and Fig 2-2-5), from 140 cm to 180 cm, also in serial (this thermometer probe is called “Air Probe” hereafter).

Since all the three thermometers on the Air Probe showed similar behaviors and clear diurnal changes (Fig 3-2-8), we assumed that they had always been above the snow layer and had recorded the air temperature. On the contrary, some thermometers on the Snow-

Air Probe showed different behaviors from those on the Air Probe, depending on time and the thermometer heights (Fig 3-2-8). It likely means that they were sometimes below the snowfall. Accordingly, we compared the data of the Snow-Air Probe and the Air Probe to estimate the snowfall.

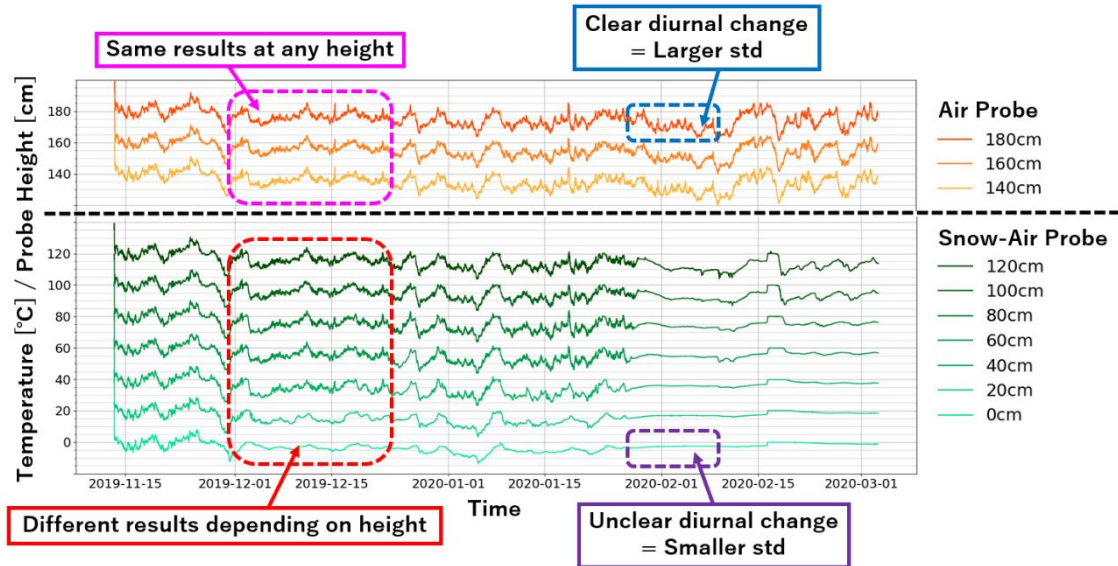
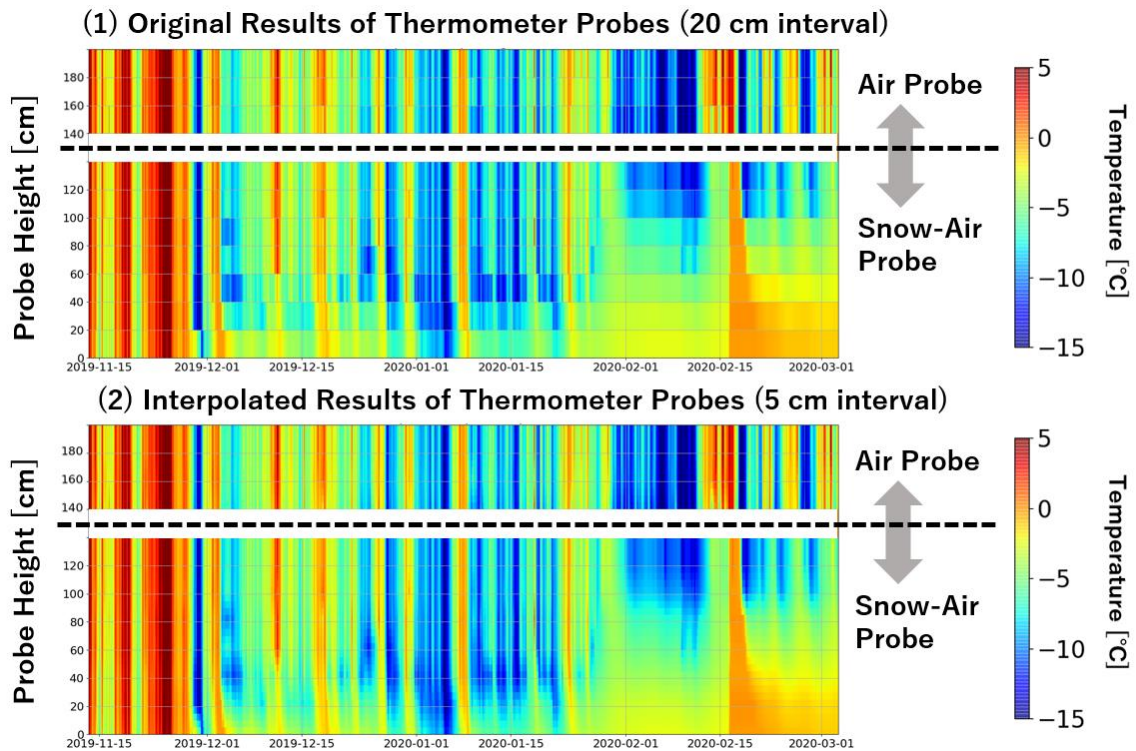


Fig 3-2-8. Original thermal data recorded by the thermometer probes



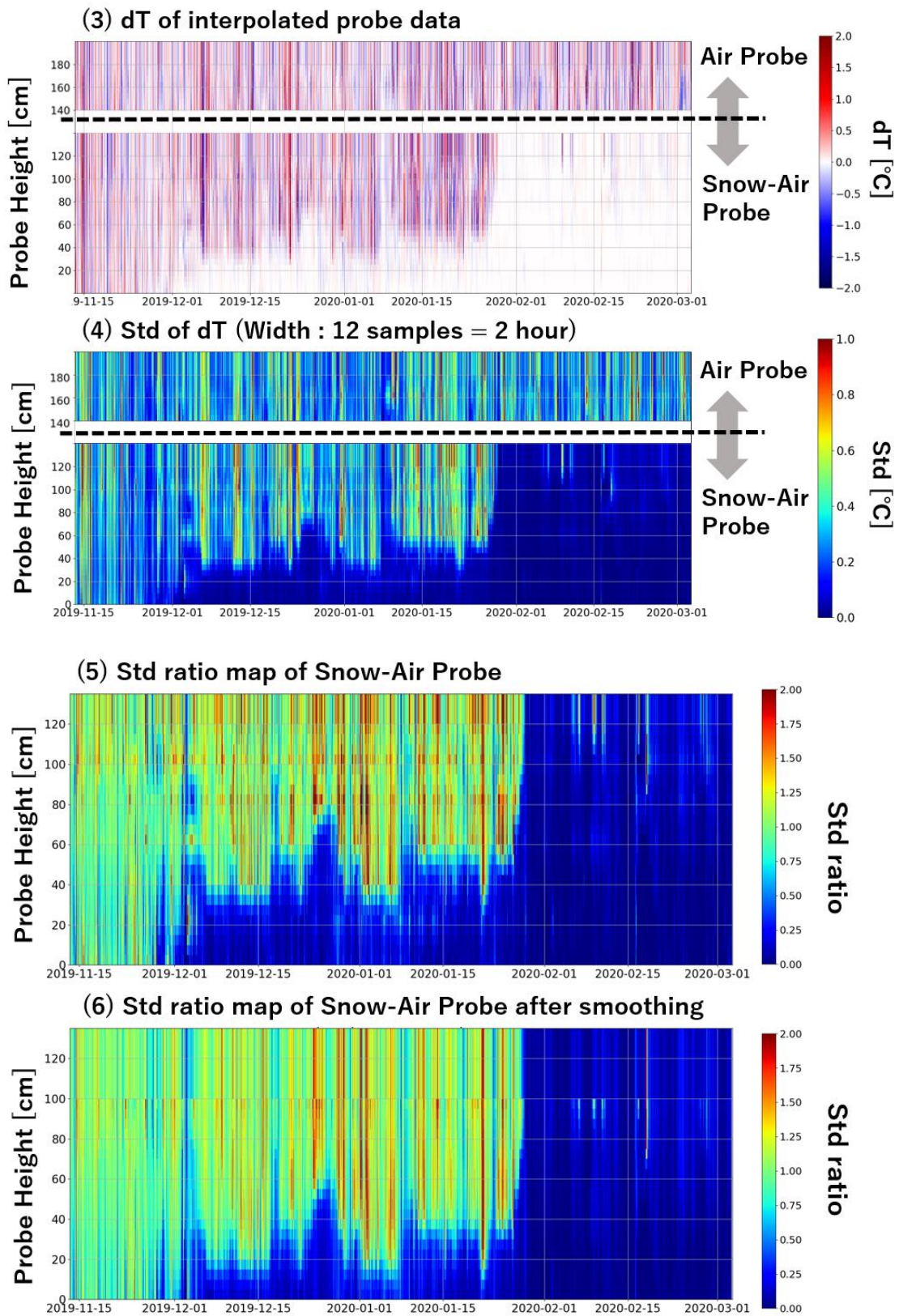


Fig 3-2-9. Analysis methods of the thermal data in the thermometer probes

Since we gained the thermal data with higher resolution in this season than in 2018-2019, we attempted to evaluate the snowfall quantitatively. The original thermal data (Fig 3-2-9-(1)) used for this analysis were corrected by the result of the calibration experiment to eliminate the effect of the individual differences.

First, in order to improve the height resolution, which was originally 20 cm interval (Fig 3-2-9-(1)), we interpolated the data of the Snow-Air probe linearly in 5 cm interval (Fig 3-2-9-(2)). Then, we investigated the standard deviation (STD) of the first-order time differentiations (dT) as explained in 3-1-1. Figure 3-2-9-(3) shows dT of the spatially interpolated data, and Fig 3-2-9-(4) shows the STD of 12 samples of dT (2 hours with 10-minute intervals) at each height. When the STD is large, we regard the thermometer is above the snowfall and exposed to the air. On the contrary, when the STD is small, we infer that the thermometer at this height is below the snowfall. To distinguish whether each probe was above the snowfall or not automatically, the STD of the individual thermometers in the Snow-Air probe are compared with the average STD of the thermometers in the Air probe in the same time (Fig 3-2-9-(5)). Fujihara et al., (2015,2017) used the STD of the temperature itself (12 samples at the sampling rate of 1 sample in 2 hours), and judged whether a thermometer was covered by snow or not by a threshold STD of 0.3 °C. However, the STD changes depending on the weather conditions even when the thermometer is not covered by snowfall. Therefore, using the STD value in the outer air as a reference is better than to set some certain threshold value in standard deviation.

As shown in Fig 3-2-9-(5), the STD ratio shows obvious changes in time. However, the top of the raw STD-ratio points (snow-covered points) shows discontinuous ups and downs, which we hypothesized as the effect of temporal snow-stuck on the thermometers. Therefore, we applied the smoothing processing on the STD ratio. A median filter was applied for 12 samples in a time and 8 samples in height (2 hour in time and 40 cm in height) (Fig 3-2-9-(6)). To estimate the snowfall based on the smoothed standard deviation ratio, we set the threshold value at 0.35. The lowest pixel whose standard deviation ratio was higher than 0.35 on each time was substituted for estimated snowfall. Probe data and estimated snowfall were shown in Fig 3-2-10 together.

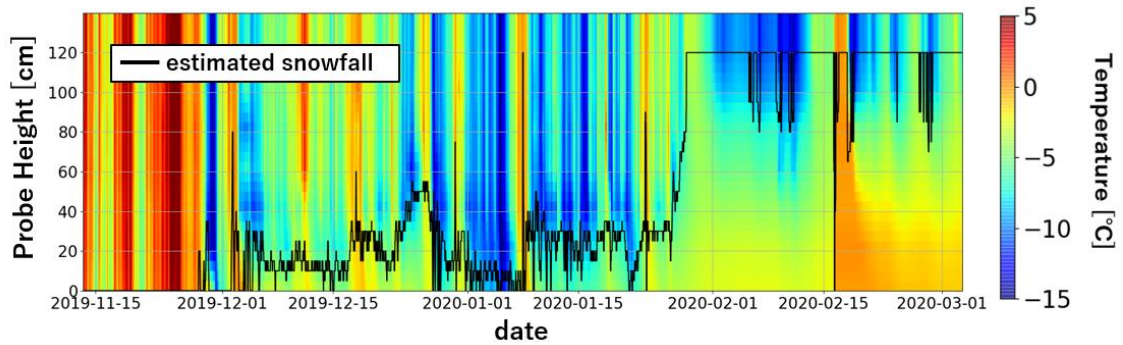


Fig 3-2-10. Estimated snow depth by the thermometer probes (black line) and the original thermal data (colormap)

On the contrary, the following Fig 3-2-11 shows the estimated snow depth calculated by the same methods as Fujihara et al. (2015,2017) (the detailed methods are in 3-1-2). In order to process the data in the same way, the data of thermometer probes were down sampled (1 sample in 2 hours). Compared to this result, the Fig 3-2-10 shows much clearer and smoother trends in snow depth due to the measurements with high resolution in time and depth.

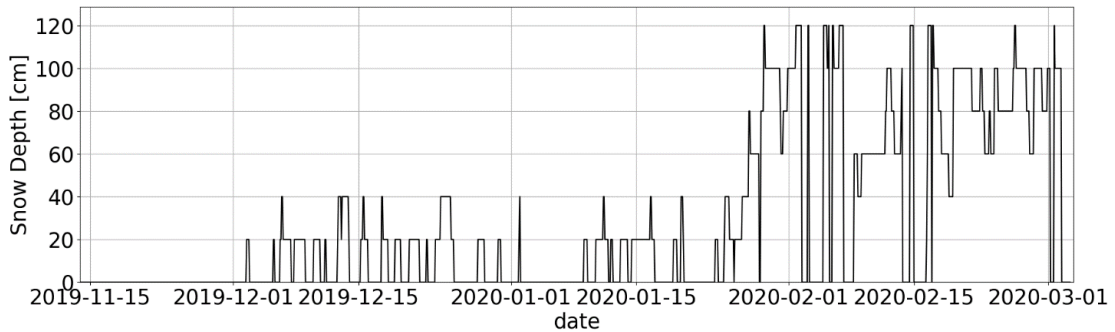


Fig 3-2-11. Estimated snow depth by the method in Fujihara et al. (2015 and 2017)

4. Results

4-1 2018-2019 Winter Season

4-1-1 Infrasound Microphones and Seismometers

<Signal Detection>

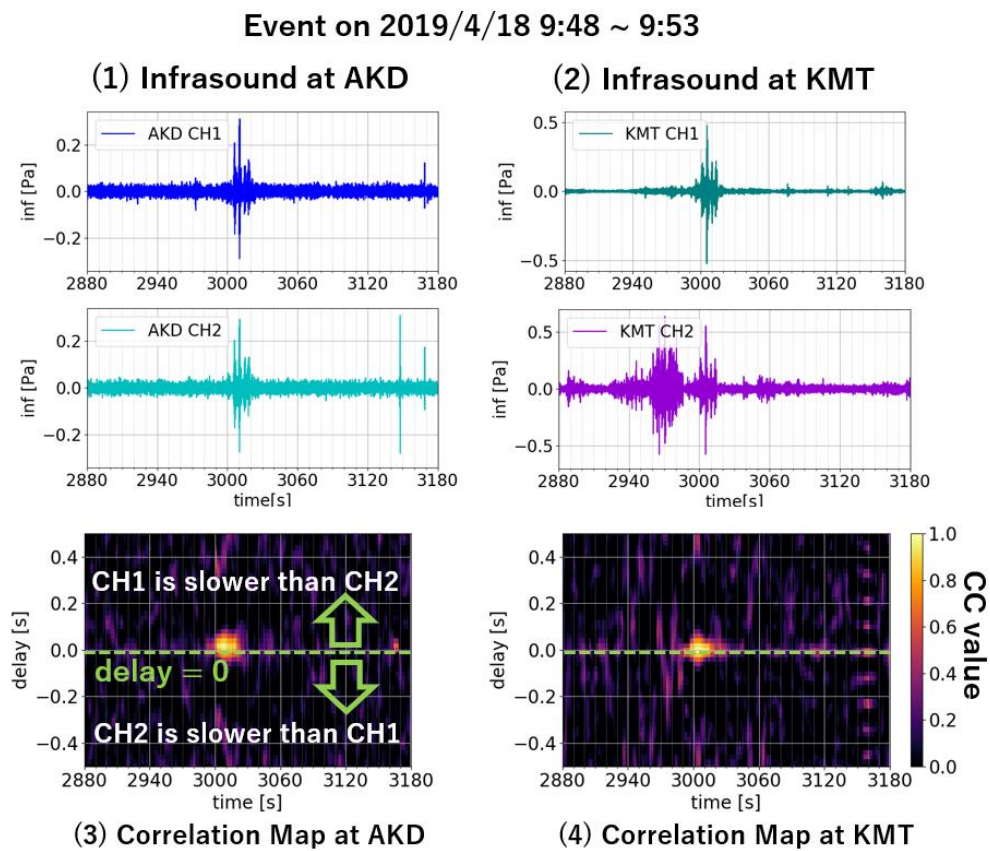


Fig 4-1-1. Infrasound waveforms and correlation maps of the event on April 18th, 2019 at 9:48~9:53

The Fig 4-1-1 and Fig 4-1-2 show the 2 examples of the detected events by the analysis of CCs (cross-correlation coefficients) of 1~10 Hz infrasound signals in 2 microphones at AKD and KMT. The left figures show the waveforms and correlation map of infrasound signals in the frequency band of 1-10 Hz at AKD, and those at KMT are shown on right hand side. The CH1 and CH2 refer to the microphones at each station. In these correlation maps, the color bar on the right represents the CC value. The horizontal axis shows the initial time of the windows to calculate the CCs. The vertical axis shows the relative delay

time of CH1 to CH2; the relative delay time is positive when the signals at CH1 is delayed compared to those at CH2 as the Fig 4-1-1-(3) shows. The length of data to calculate the CCs is 5 seconds and CC is calculated every 1 s in time (horizontal axis) and 0.02 s in relative delay time (vertical axis).

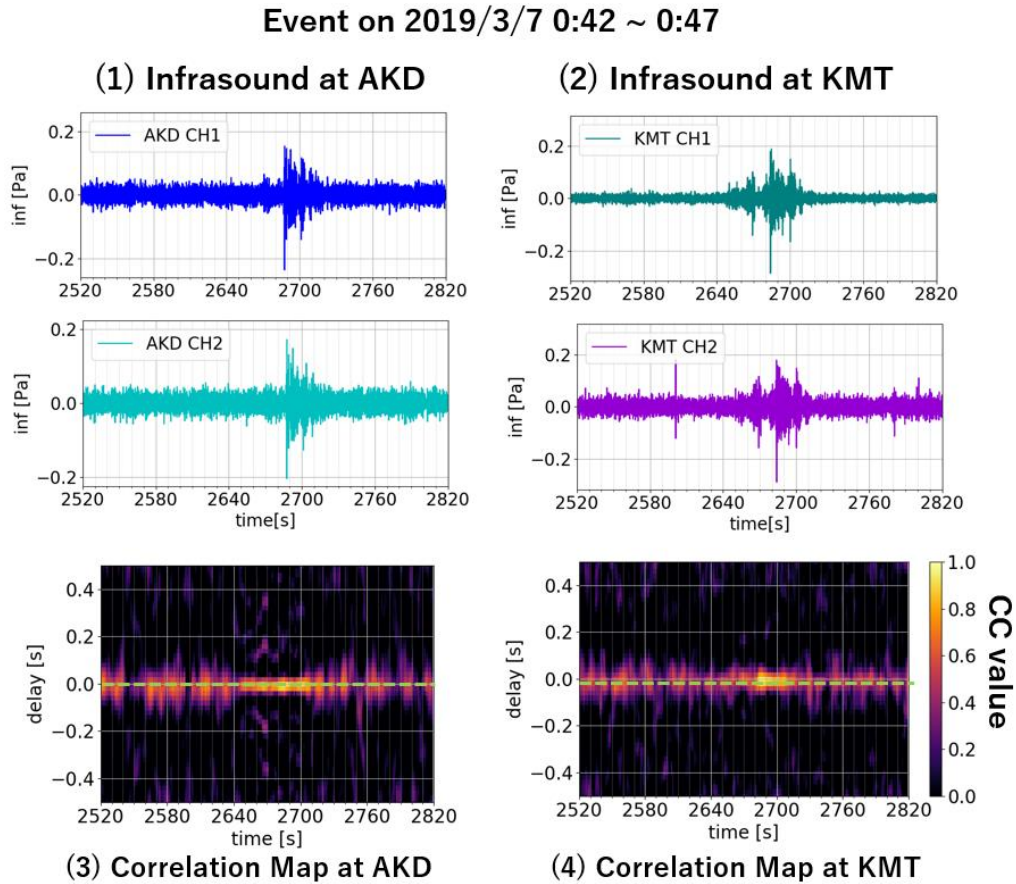


Fig 4-1-2. Infrasound waveforms and correlation maps of the event on March 7th, 2019 at 0:42~0:47

<Distinction of Infrasonic Signals and Seismic Signals >

We calculated the normalized SI ratio on the 41 selected events (see 3-1-1). Fig 4-1-3 and Fig 4-1-4 show the examples of signals recorded at AKD by the infrasound microphone and the seismometer, and the normalized SI ratios (from the left to right columns). Here, SI ratio is power spectra ratio of seismic signal to infrasonic signal, ASII is the averaged SI ratios of the 12 samples with infrasound signals used as the reference and the normalized SI ratio is the ratio of SI to ASII (see 3-1-1 for detail). The waveforms have been high-pass filtered above 1 Hz. The horizontal axes are the lapse times in second each

of which start time is on the hour. The vertical axes show the acoustic pressure (Pa), vertical ground velocity (mm/s), and frequency (Hz), respectively. The color-scale was used to show the ratio on each frequency and time in log 10 scale in the normalized SI ratio map. Blue shows the normalized SI ratio is low and red shows it is high. If the signal was infrasound originated, the ratio goes close to 1 (white). On the contrary, in the case of seismic signal, the ratio is much higher than 1 (red).

Of the 41 candidate signals, we found that most of the events only had infrasonic signals. For 5 events that occurred before the installation of the seismometer at AKD, we could not investigate the normalized SI ratios. As far as we compared the amplitudes and waveforms between the microphone data at AKD and the seismometer data at the other four seismic stations, we did not see any clear signals indicating seismic waves. On the other hand, both infrasonic and seismic signals were recognized in 4 events in April, which are presented later in this section.

Fig 4-1-3 shows one of the examples of infrasound signals originated from the exercise by the Japan Self-Defense Force. The normalized SI ratio map goes 1 when the infrasonic signals were detected ($t=1020 \text{ s} \sim 1050 \text{ s}$). Fig 4-1-4 shows the waveforms and The normalized SI ratio map of one of the events which recorded only infrasonic wave. As the ratio map shows, the ratio goes close to 1 when the signal arrived ($t=2670 \text{ s} \sim 2730 \text{ s}$), and we can infer that the both waveforms recorded in microphones and seismometers were an infrasonic wave. Because a microphone records more significant power of wind noise than a seismometer, the normalized ratio tends to be less than 1 when the ratio of infrasound signal power to the wind noise power is smaller than that of the reference data used for ASII.

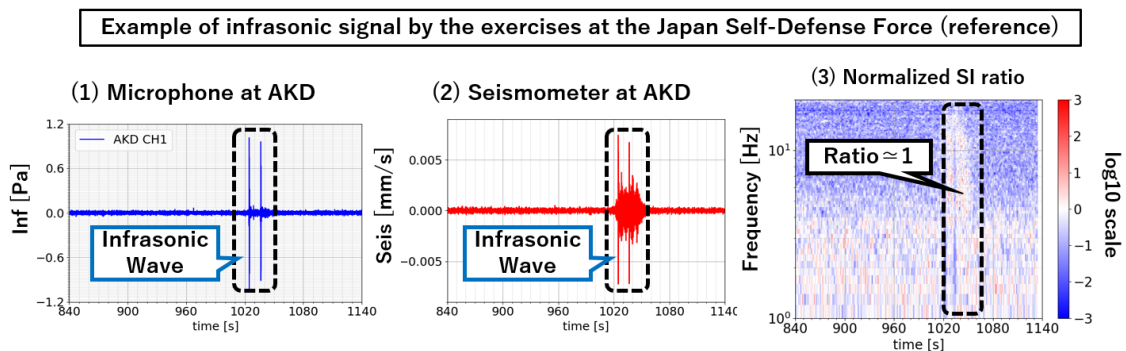


Fig 4-1-3. Example of infrasonic signal by the exercises at the Japan Self-Defense Force (reference) on March 5th, 2019 at 9:14~9:19

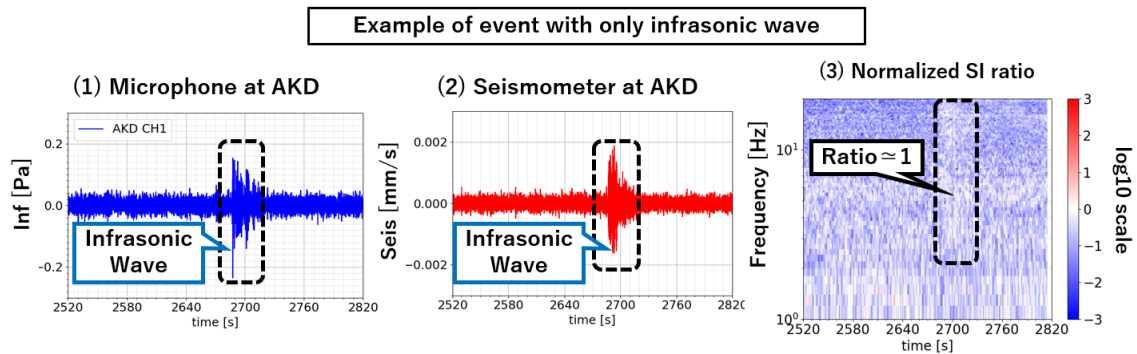


Fig 4-1-4. Example of event with only infrasonic wave on March 7th, 2019 at 12:15~12:20

On the contrary, the following figures (Fig 4-1-5) show the 4 events (denoted as “Event 1”- “Event 4”) which recorded both infrasonic and seismic waves. Although it is not obvious from the waveforms, the infrasonic wave was clearly recognized by the CC analysis. When the infrasonic wave was observed, the ratio map shows the ratio is low. We also observe time and frequency regions where the ratio is significantly larger than 1, which we regard is due to seismic waves.

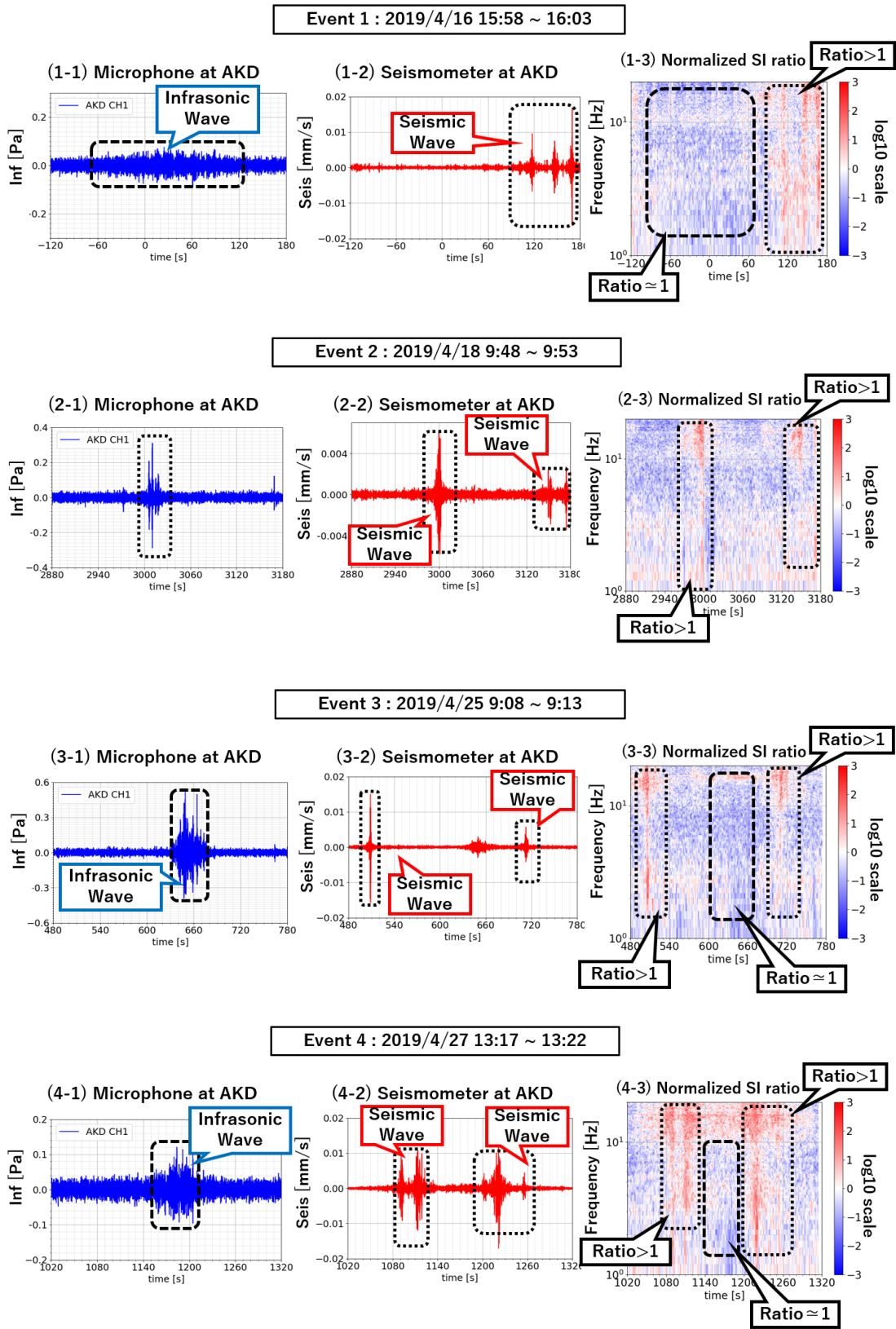


Fig 4-1-5. 4 events (Event 1 ~ Event 4) with both infrasonic and seismic signals

<Signal Comparisons Among Different Stations>

Fig 4-1-6-(1) and Fig 4-1-6-(2) show the correlation maps at AKD and KMT of Event 4 (the same event in Fig 4-1-5). The length of data to calculate the CCs is 5 seconds and CC is calculated every 1 s in time (horizontal axis) and 0.02 s in relative delay time (vertical axis) as stated in 4-1-1. The Fig 4-1-6-(3) shows the zero-shift CC value at KMT and AKD which correspond to the green dashed lines on Fig 4-1-6-(1) and Fig 4-1-6-(2). Fig 4-1-6-(4) represents the correlation of CCs at KMT and AKD. Vertical axis shows that relative delay time and horizontal axis shows the initial time of calculate the CC. Relative delay time is positive when the signals in KMT are delayed compared to those at AKD as the notation shows. Here, the time-window to calculate the correlation of CCs is 30 seconds in length and shifted every 5 s (horizontal axis). The relative delay time was investigated in 1-s resolution (vertical axis).

As Fig 4-1-6-(4) shows, the time delay between CCs at AKD and KMT changed in time. At $t = 1110\sim 1150$ s, the correlation is high with the relative delay time ~ -8 s. However, the relative delay time with the maximum correlation shifted to ~ 0 s at $t = 1150\sim 1160$ s, as green arrow indicates. This may indicate that the source of this infrasound signal shifted from the point which is close to KMT to the point where the distances to KMT and AKD are similar.

In addition, Fig 4-1-6-(5) shows the seismic signals recorded at the 4 seismic stations. Although the seismic signals at $t = 1080\sim 1140$ s were recorded in all seismometers, the seismic signals at $1200\sim 1240$ s was recorded only at AKD and the amplitudes of seismic signals was high at AKD compared to the other stations. Based on the data, we expect that this seismic ground motion happened locally and did not propagate through the seismic network.

Event 4 : 2019/4/27 13:17 ~ 13:22

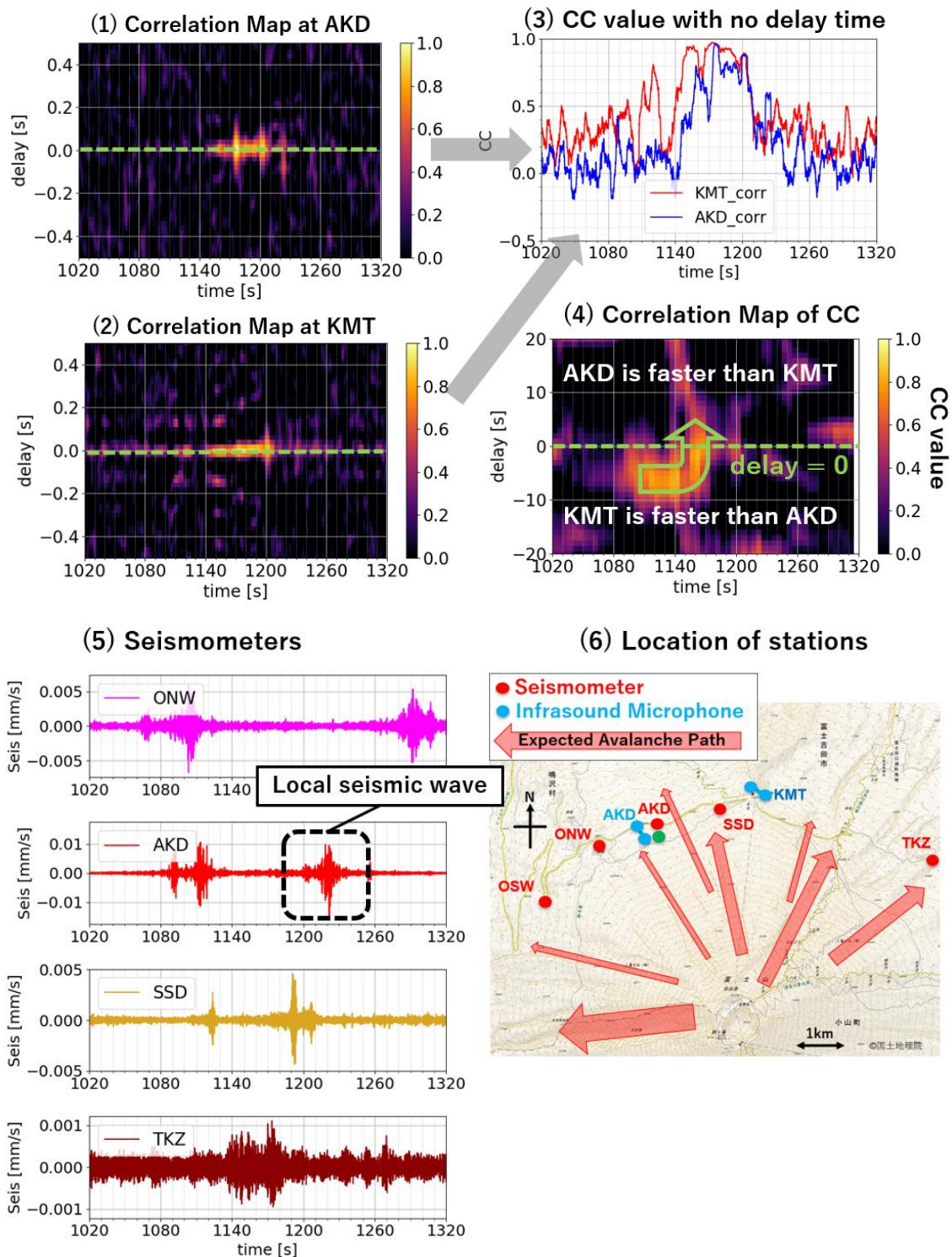


Fig 4-1-6. Correlation maps and the seismic waveforms on Event 4

<Visibility>

The visibility was gained by the method of the previous section and the results are shown in Fig 4-1-7. The horizontal axis shows the date of observation and the vertical axis shows the infrasound visibility (green) in 0 to 1 scale. When the infrasound visibility is high (1.0), the noise level of infrasound microphones is low so that the infrasound array has high detectability. On the contrary, when the visibility is low (0.0), the infrasound array has low detectability. Besides, the distribution of the events detected by the microphone pairs are also shown in Fig 4-1-7 with the diamond-shaped markers. The red markers show the events with only infrasonic signals, and the blue markers show the events with both infrasonic and seismic signals. The black frame indicates the events for which we could not confirm the absence of seismic waves as explained in 4-1-1.

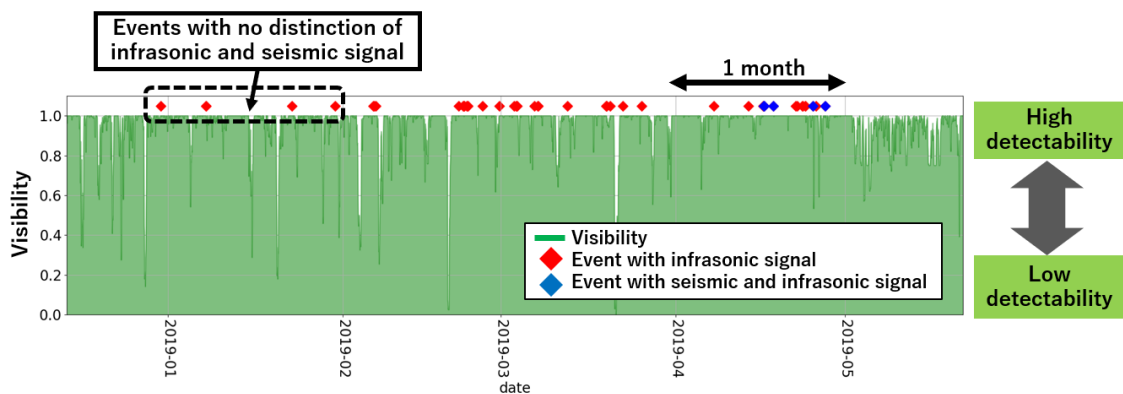


Fig 4-1-7. The visibility of infrasound array during the observation period in 2018-2019 winter season

4-1-2 Thermometer Probe

The result of thermometer at each height is shown in Fig 4-1-8. The red, blue, and green lines show the temperatures at 0 cm, 40 cm, and 80 cm above the ground, respectively. The estimated snow depth is shown in Fig 4-1-8 with the black line. Although the resolution is not high, we can visualize the snowfall clearly. In addition, the distribution of the events detected by the microphone pairs are also shown in Fig 4-1-8.

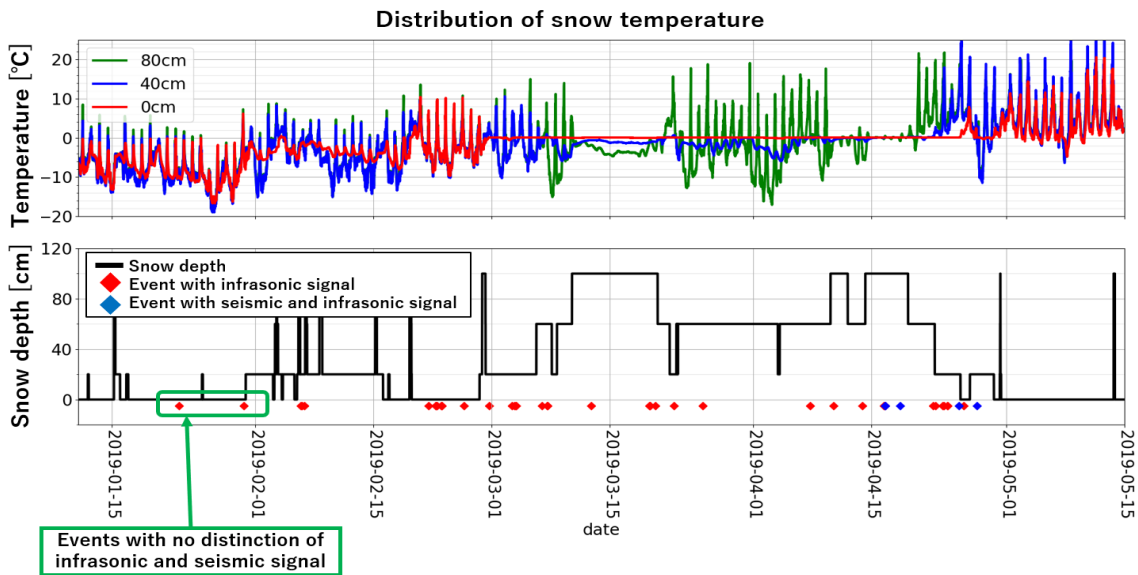


Fig 4-1-8. Recorded temperature in the thermometer probe (top) and estimated snow depth by thermometer probe (bottom)

4-2 2019-2020 Winter Season

4-2-1 Infrasound Microphones and Seismometers

<Detected Events>

By calculating the CCs of infrasonic signals between S-array and L-array, we selected 72 events. First, we excluded the 5 events whose infrasound waveforms were significantly strange as avalanche signals. Those infrasound waveforms of those 5 events are shown in Fig 4-2-1. Those waveforms are filtered in the frequency band of 1-10 Hz. The following 5 event ((1)-(5)) have the short and strong impulse shaped waveforms. Since the waveforms are similar to those of exercises at the Japan Self-Defense Force, which are recorded in the previous winter season, we assumed that they were not originated by avalanches.

Then, we calculated the correlation vector on each signal and excluded the 37 signals which are estimated to be inconsistent (see 3-2-1). Fig 4-2-2 show the 3 examples of these inconsistent infrasound waveforms in 1 Hz to 10 Hz.

After these screening, we obtained 30 events which are assumed to be avalanche signals. The following analysis are applied to only those 30 events.

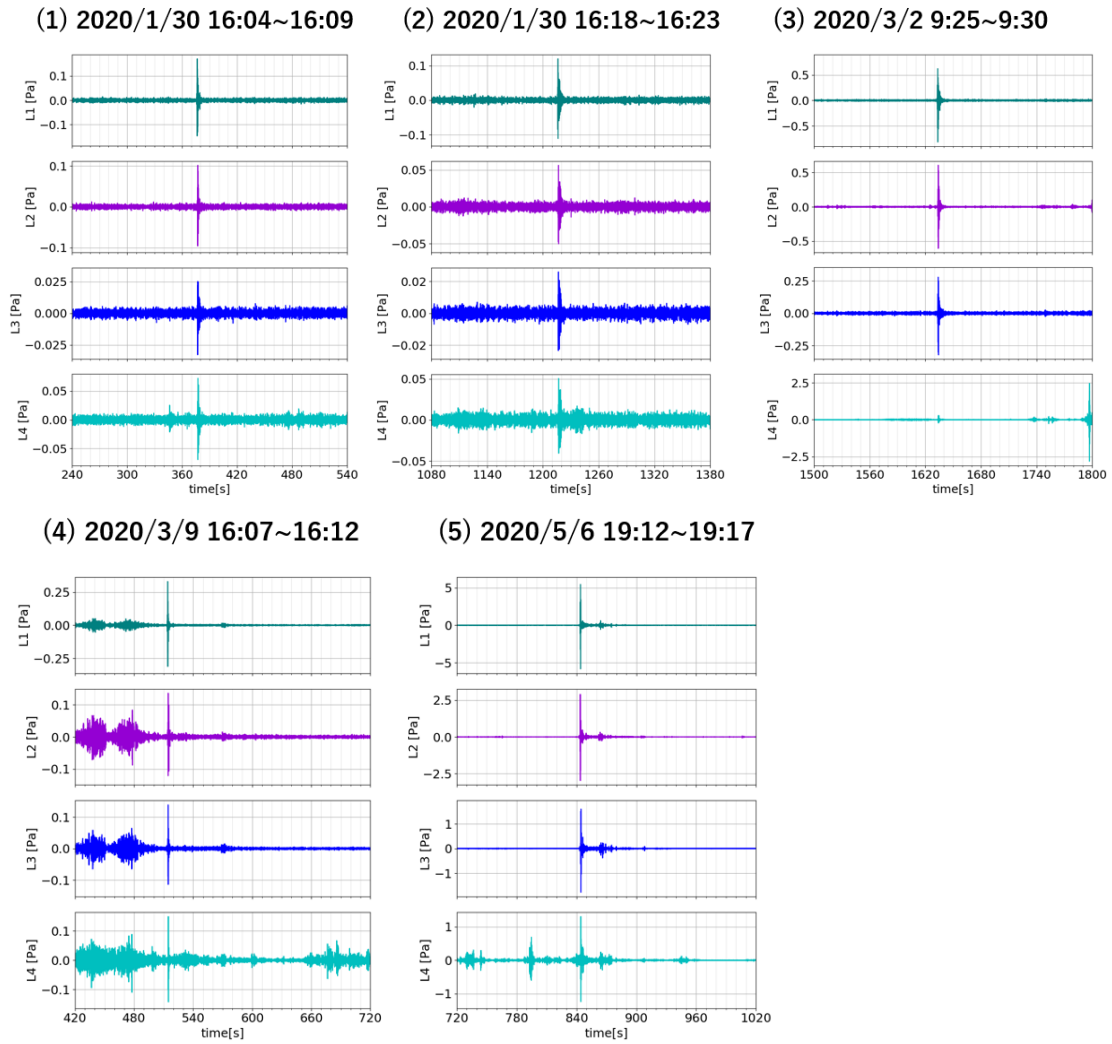


Fig 4-2-1. The infrasonic waveforms of 5 excluded events

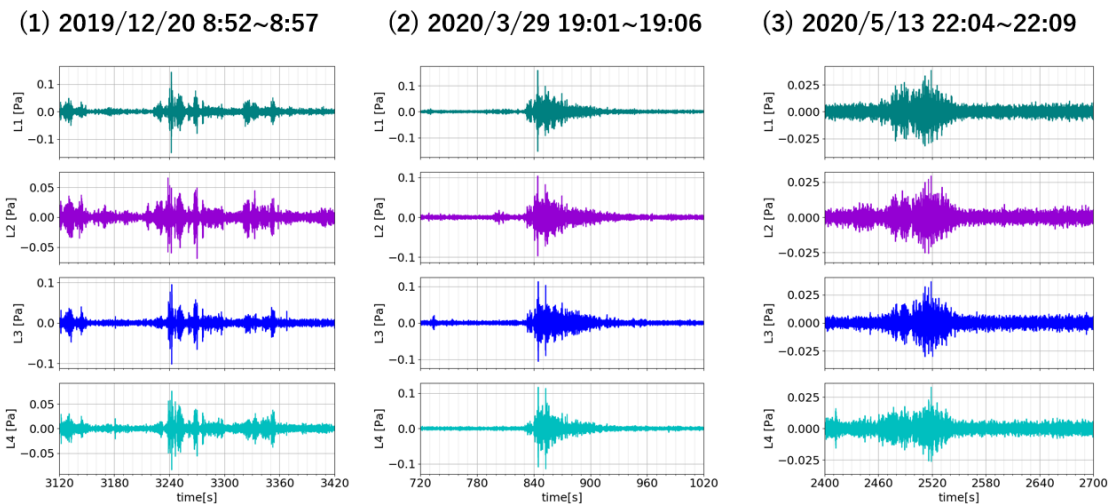


Fig 4-2-2. The infrasonic waveforms which were estimated to be inconsistent

<Source Detection by Multi-Channel Semblance>

We estimated the source of infrasonic signals on the events above by the multi-channel semblance. In order to visualize the movement of the origin of sources, we calculated the source of infrasonic signals at every 5 seconds (with the window length of 60 s) in 30 events as stated in 3-2-1. Fig 4-2-3 and Fig 4-2-4 show the results of the 2 of those events (denoted as “Event A” and “Event B” respectively).

Fig 4-2-3-(1) and Fig 4-2-3-(2) are the original waveforms of infrasound microphones from the L-array and those of seismometers, both in the frequency band of 1-10 Hz of the event at 14:38~14:53 on January 16th, 2020 (Event A). Fig 4-2-3-(3) displays the correlation maps of all pairs of the infrasonic signals in L-array. The infrasonic microphone pairs to calculate the correlation map is shown on the vertical axis. The horizontal axis shows the initial time of the window to calculate the correlation and the vertical axis shows the relative delay time. In these correlation maps, the window length to calculate the CCs is 5 seconds, and CC is calculated every 1 s in time (horizontal axis) and 0.05 s in relative delay time (vertical axis). Fig 4-2-3-(4) and Fig 4-2-3-(5) show the source estimation results by the multi-channel semblance. In Fig 4-2-3-(4) the results are shown in 2D on the red relief image map of Mt. Fuji, and Fig 4-2-3-(5) shows the results in 3D on the DEM model of Mt. Fuji. In Fig 4-2-3-(4), the X-axis shows east-west [m] and the Y-axis shows north-south [m]. The origin of the coordinates is infrasound array as the black box represents. In Fig 4-2-3-(5), the vertical axis shows the elevation [m], and horizontal axis shows the north-south and east-west axis [m]. As in Fig 4-2-3-(4), the coordinate of infrasound array is (0 m, 0 m, 2300 m) as the black box represents. In these figures, the circles show the estimated location of the sources. When the size of the circle is big (small), it means the semblance value is high (low) at the point and in the time window. To visualize this map clearly, we plotted the locations which satisfy the following conditions; the semblance value is higher than 2.0 and higher than 0.9 times of the maximum semblance value at every time window. If the semblance value satisfies these threshold values at multiple locations in one time window, we plot multiple dots on the figure at each time. The colors of those circles mean the lapse time starting on the hour (9:00 on April 27th, 2020, in this case), as the color at the bottom of the figure represents. As stated in 3-2-1, we calculated the CCs in the multi-channel semblance method and the time means the beginning time of data used to calculate the CCs. In reference to this color bar, we can visualize the change in location of sources by time, of which resolution is discussed later.

The waveforms in Fig 4-2-3-(1) have clear infrasonic signals at $t = 2980\sim 3030$ s as the blue frame indicates. The corresponding waveforms were also recorded in seismometers as shown in Fig 4-2-3-(2) by the blue frame. Although there was no seismometer at KMT, the amplitudes of waveforms at $t = 2980\sim 3030$ s in the seismometer at SSD (the nearest seismic station to KMT with a distance of 436 m) was roughly 0.004 mm/s. Since the amplitudes of the infrasound microphones were roughly 0.2 Pa, the power spectral ratio of infrasonic signals to seismic signals is estimated to be approximately $4.0e-4$ $(\text{mm/s})^2/\text{Pa}^2$ in the frequency band of 1-10 Hz. According to the measurements in 2018-2019 winter season and the ASII value in Fig 3-1-2, this power spectral ratio infers that the seismometers recorded ground motion by the infrasonic wave (see 3-1-1 for detail). This infrasonic signal is also verified at the correlation maps in Fig 4-2-3-(3). As the blue frame shows, there were high CC values at each microphone pair.

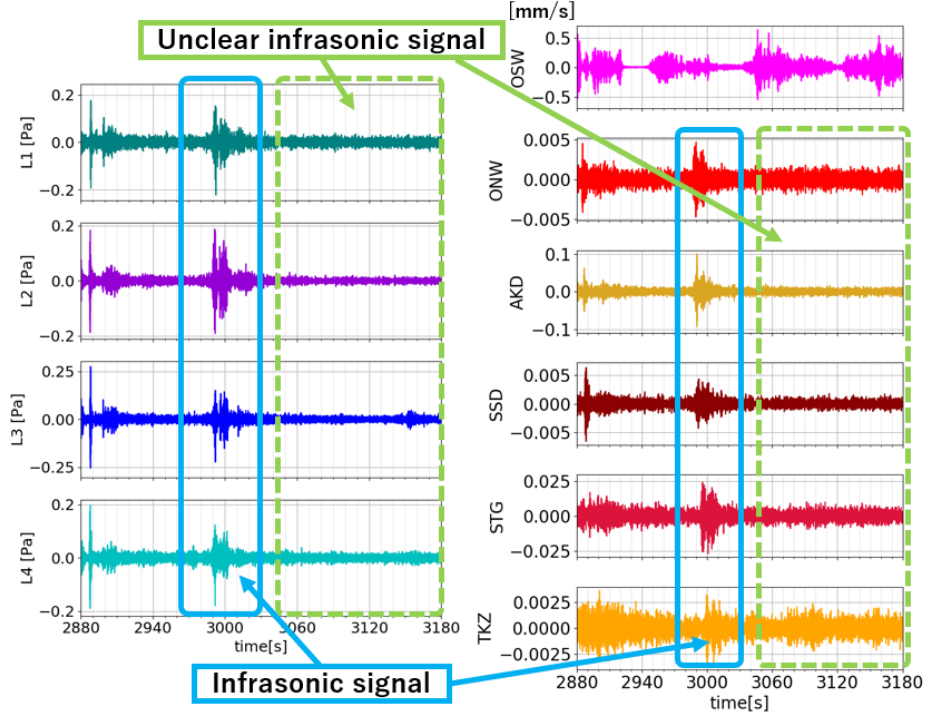
In addition, the correlation maps also show high CC values at $t = 3050\sim 3180$ s at all microphone pairs, as the green frame represents. However, there were no clear waveform on the original infrasound data and seismic data as Fig 4-2-3-(1) and Fig 4-2-3-(2) represent. The relative delay times of the high CC are steady and different from those for the signal at $t = 2980\sim 3030$ s with no continuous shifts. Therefore, we assume that this signal is independent of the signals at $t = 2980\sim 3030$ s.

Results of source estimation in Fig 4-2-3-(4) and Fig 4-2-3-(5) also shows the different direction depending on time. As the blue frames show, the signals at $t = 2980\sim 3030$ s are estimated to be originated from the north-west. On the other hand, the source of the signals at $t = 3050\sim 3180$ s is estimated to be from the north as the rectangular frames show.

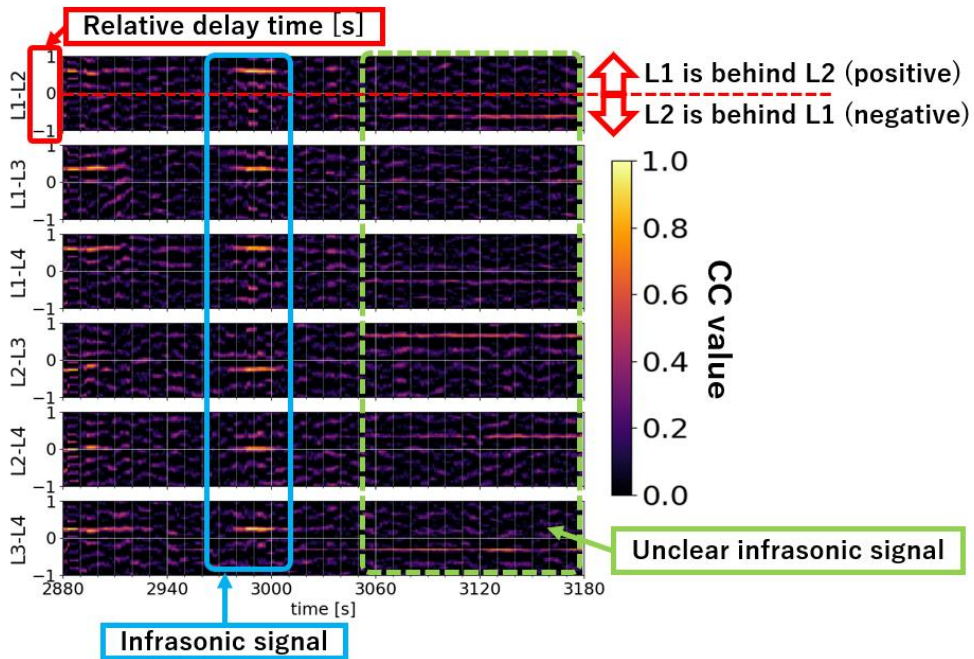
Event A : 2020/1/16 14:48~14:53

(1) Infrasound Microphones

(2) Seismometers



(3) Correlation map between L-array



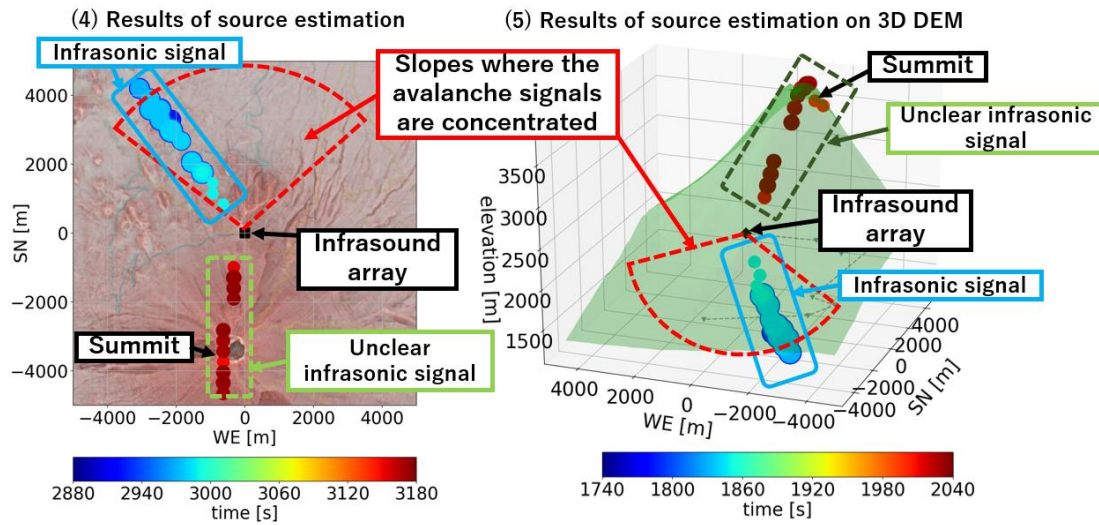
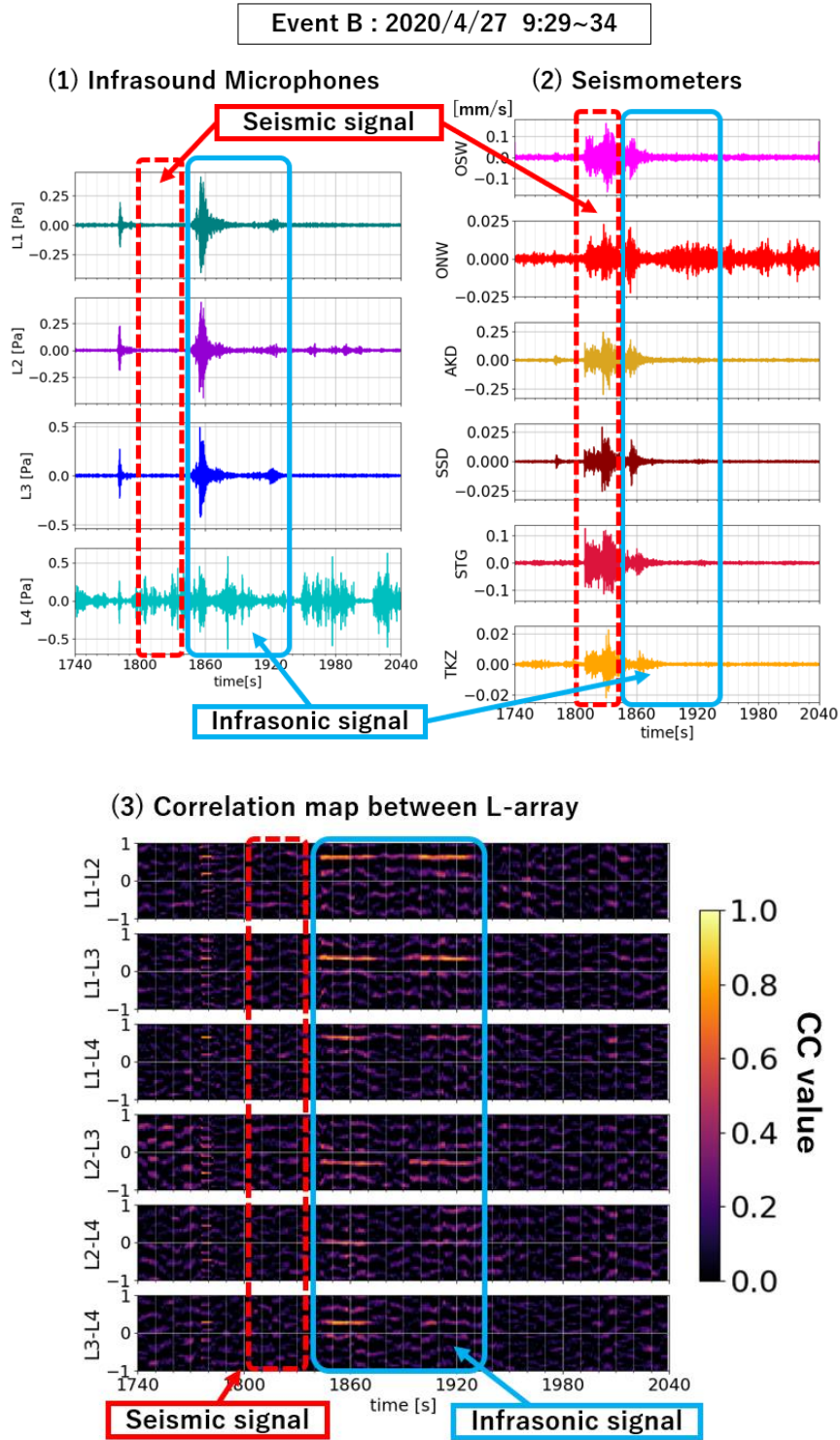


Fig 4-2-3. Infrasonic and seismic waveforms, correlation maps and results of source estimation of the Event A (January 16th, 2020 at 14:48~14:53)

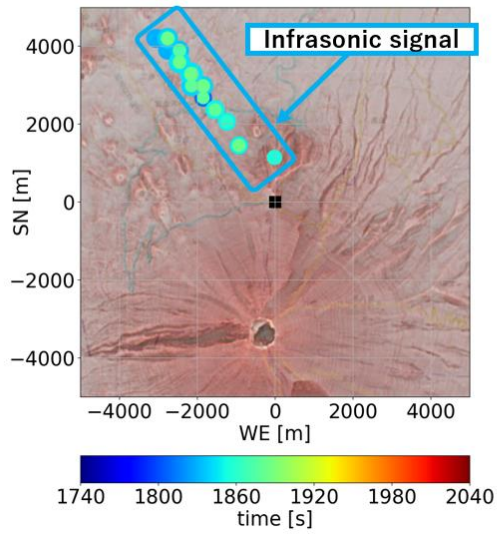
Fig 4-2-4 shows the infrasonic and seismic waveforms, correlation maps and results of source estimation of the event at 9:29~9:34 April 27th, 2020 (Event B). Based on the correlation maps in Fig 4-2-4-(3), infrasonic signals were recorded at $t = 1840\sim 1940$ s as the blue frame indicates, and this signal is also clearly recognized on the waveforms in Fig 4-2-4-(1). On the other hand, the seismometers show clear but different waveforms at $t=1800\sim 1840$ s as red dashed frame indicates. Since no corresponding signal was found in the infrasound microphone data in Fig 4-2-4-(1). The power spectral ratio of the seismometer at SSD to the infrasound microphones at KMT is much higher than ASII, we assume that this waveform is a seismic wave. This earthquake was confirmed by the database of Japan Meteorological Agency. Besides, the correlation maps show low CC values at $t=1800\sim 1840$ s, which means no significant infrasound wave. In the source estimation, only the time windows at $t = 1840\sim 1940$ s had high semblance values as Fig 4-2-4-(4) and Fig 4-2-4-(5) show.

Surprisingly, 26 of the 30 events are located on slopes ranging from north-west to north-east from the infrasound array as red fan-shaped frame shows in Fig 4-2-3-(4). Besides, no explicit change in direction was observed during the individual event for these 26 cases. For example, Fig 4-2-5 shows the result of the source estimation for another 2 events (named as “Event C” and “Event D”). Fig 4-2-5-(C-1) and Fig 4-2-5-(D-1) show the infrasound waveforms, Fig 4-2-5-(C-2) and Fig 4-2-5-(D-2) are the correlation maps of the microphone pairs, and Fig 4-2-5-(C-3) and Fig 4-2-5-(D-3) demonstrate the result of

the source estimation on the red relief image map. A blue frame marks the infrasound signals in each plot.



(4) Results of source estimation



(5) Results of source estimation on 3D DEM

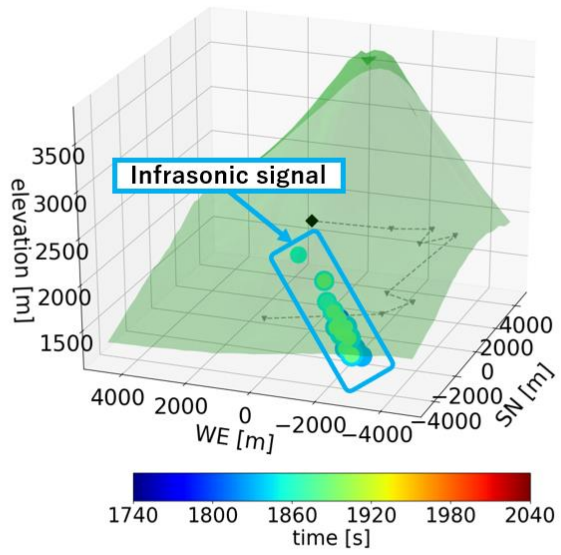
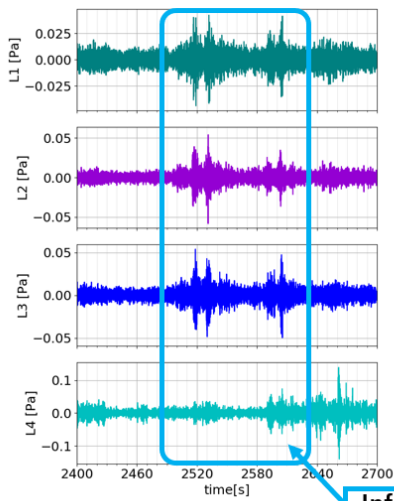


Fig 4-2-4. Infrasonic and seismic waveforms, correlation maps and results of source estimation of the Event B (April 27th, 2020 at 9:29~9:34)

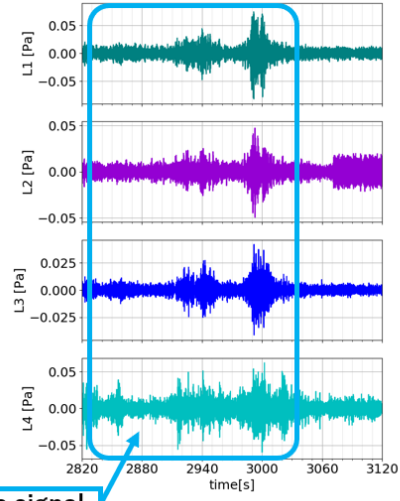
Event C: 2020/1/9 18:40~18:45

(C-1) Infrasonic microphones



Event D : 2020/1/31 11:47~11:52

(D-1) Infrasonic microphones



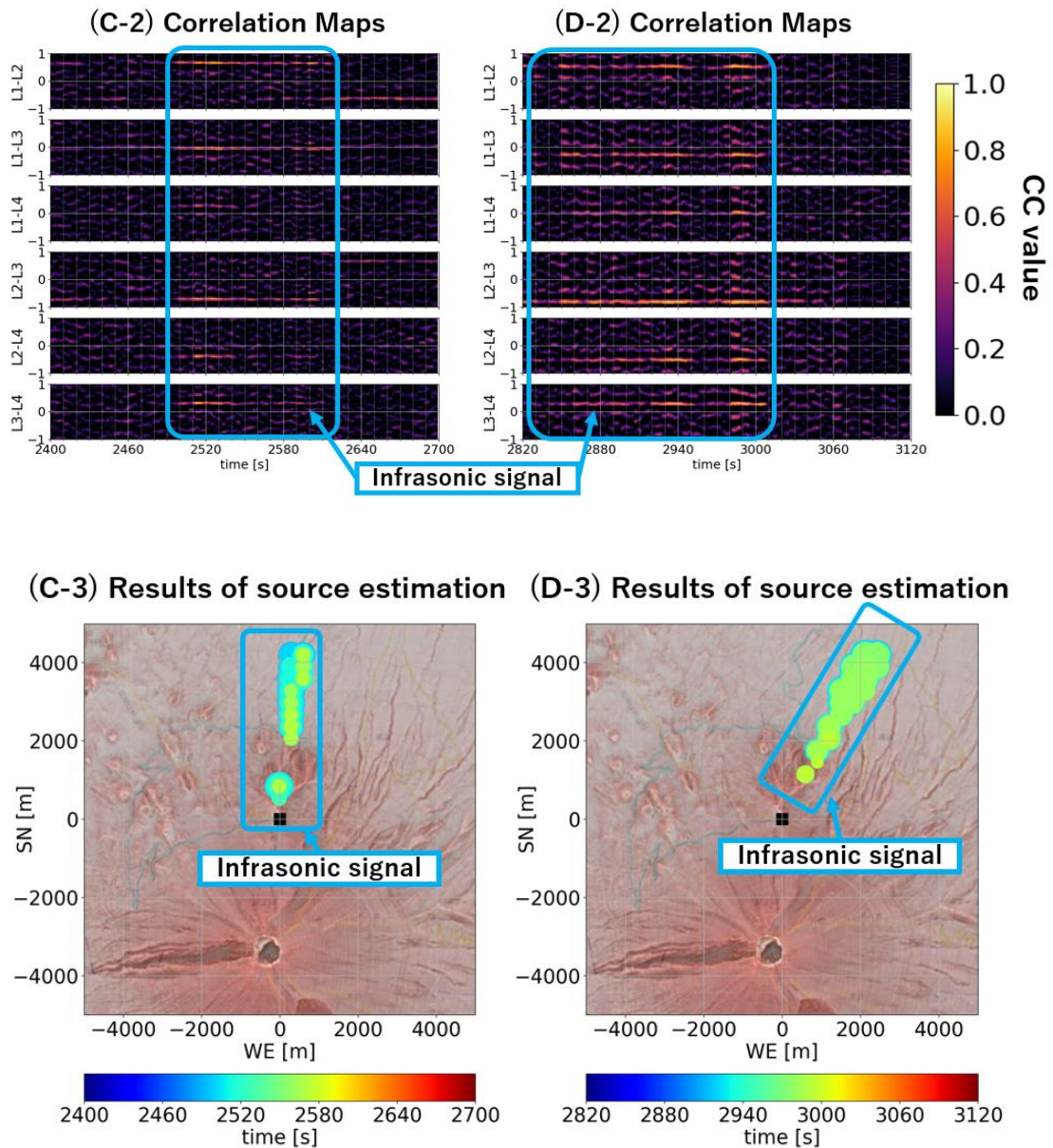
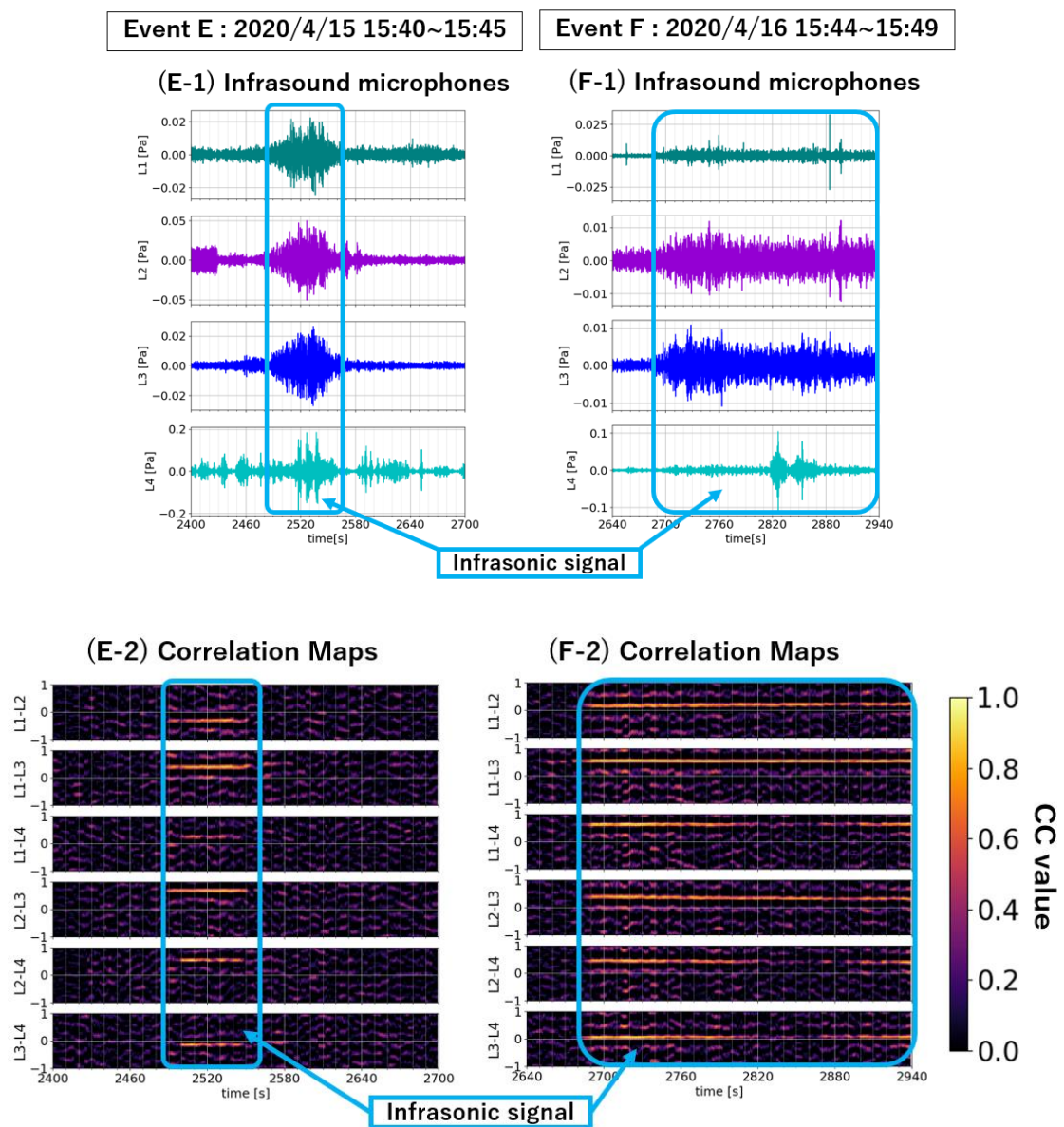


Fig 4-2-5. Infrasonic waveforms, correlation maps and results of source estimation of the typical events (Event C and Event D)

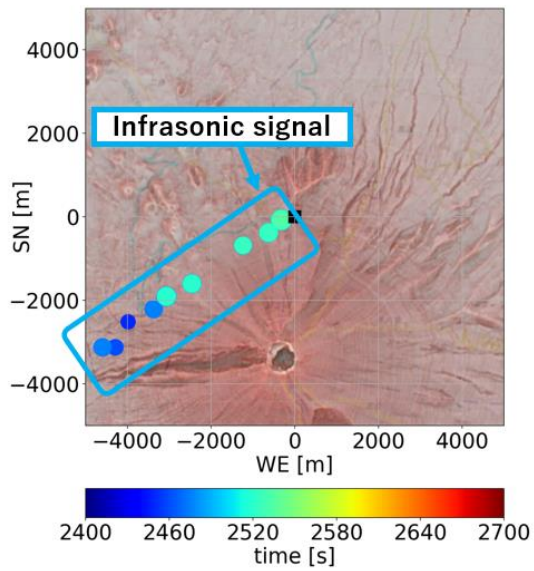
The other 4 of the 30 events shown in Fig 4-2-6 (captions are as same as Fig 4-2-5) are estimated to be originated from the different slopes from the sources of the 26 events. These 4 events are denoted as “Event E” to “Event G”, respectively.

On the Event E, F and H in Fig 4-2-6, clear waveforms and high CC values are observed in the blue frames. Those signals are estimated to be from south-west (Event E), west (Event F), and east (Event H), respectively.

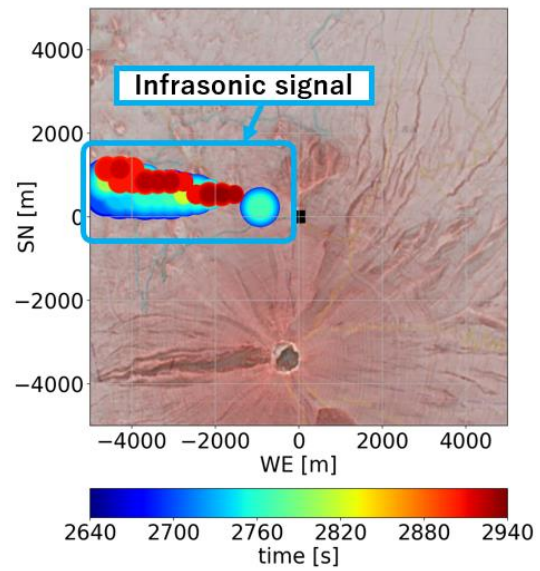
On the contrary, no clear waveforms are identified on Event G as the green frames represent. The duration time of this signal is very long (> 240 s) and the signals were originated from the south which is the same direction as the summit (Fig 4-2-3-(4)). Since the trends in the correlation maps and unclear waveforms are common to the signals on Event A in Fig 4-2-3-(3) at $t = 3050\sim 3180$ s and the results of source estimation is also similar, we infer that those 2 signals were originated from the same sources, and that both are not avalanches.



(E-3) Results of source estimation

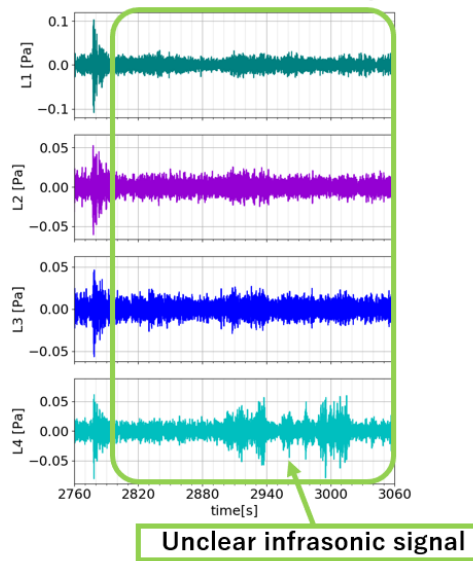


(F-3) Results of source estimation



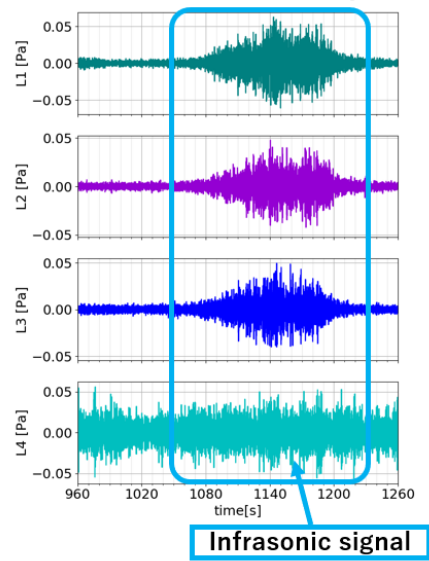
Event G : 2020/4/22 11:46~11:51

(G-1) Infrasound microphones



Event H : 2020/5/4 22:16~22:21

(H-1) Infrasound microphones



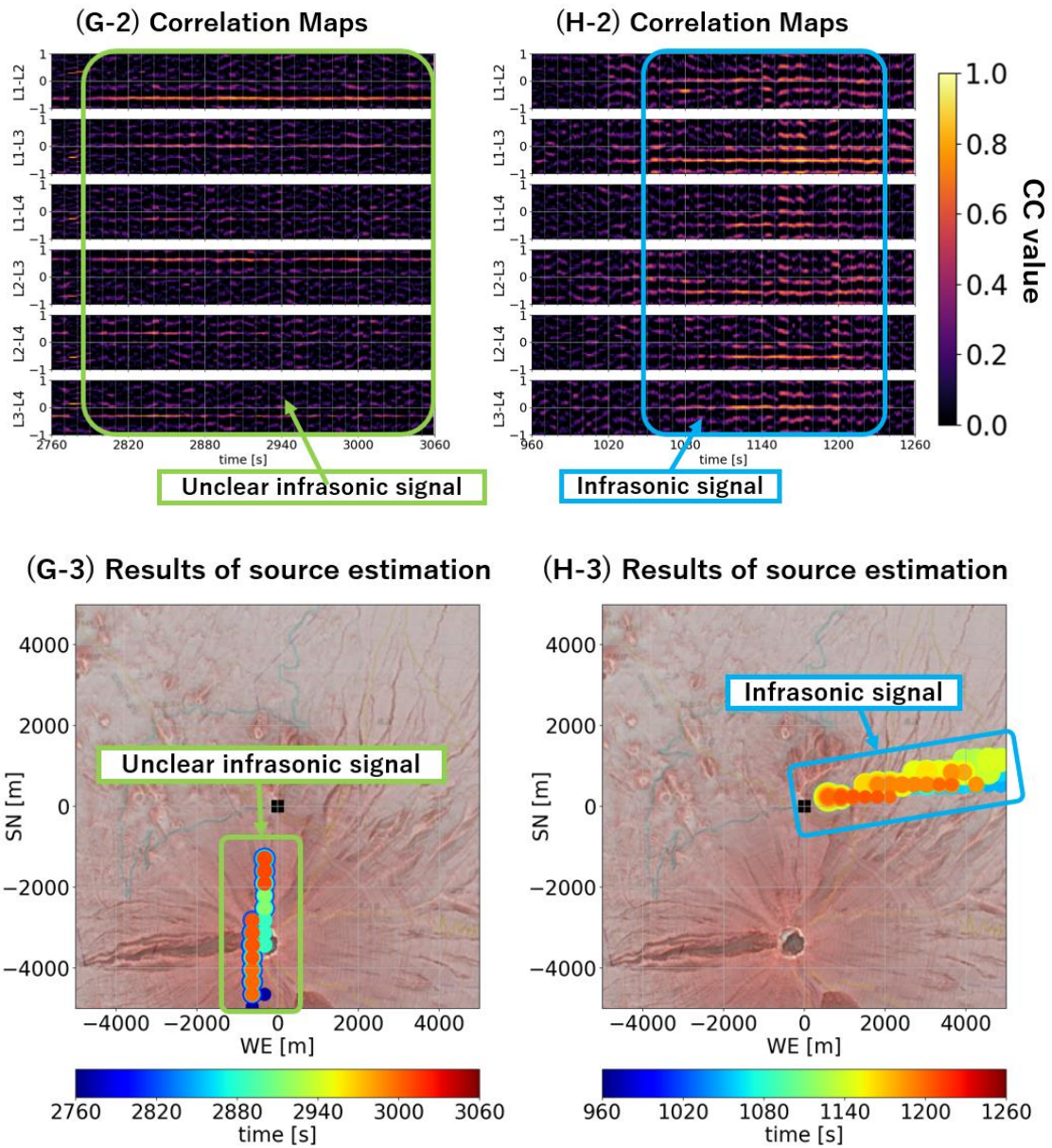


Fig 4-2-6. Infrasonic waveforms, correlation maps and results of source estimation of the 4 events with different trends (Event E - Event H)

<Seismic Signals>

In Event A (January 16th, 2020 at 14:48~14:53) and Event C (January 9th, 2020 at 18:40~18:45), we were able to clearly identify the infrasound signal on the seismometer waveforms. Fig 4-2-7-(1) and Fig 4-2-8-(1) are the seismic waveforms of the events. The onset times were picked in the following way. The power spectral density (PSD) of the vertical component of the seismometer data was calculated in a 1.28-second window sliding at 0.2 s. Then the PSD in every 0.2 s was integrated from 1 to 10 Hz to obtain the power in the frequency range. The results were shown in the logarithmic scale with the unit of $(\mu\text{m/s})^2$ (Fig 4-2-7-(2) and Fig 4-2-8-(2)). On the plots, the arrival times were manually picked. The data from OSW were too noisy to recognize the corresponding signals.

Then, the sources were estimated by the similar method as minimization of correlation vector in 3-2-1. The theoretical arrival time $t'_i(\mathbf{x})$ of all seismometers were calculated from the DEM data. Then, the model delay vector $\mathbf{t}(\mathbf{x})$ consisting of $t'_i(\mathbf{x}) - t'_{ONW}(\mathbf{x})$, ($i = \text{AKD, SSD, STG, TKZ}$) was obtained. On the contrary, we substitute the onset time vector ($\boldsymbol{\tau}$) consisting $\tau'_i(\mathbf{x}) - \tau'_{ONW}(\mathbf{x})$ to the correlation vector. Here, $\tau'_i(\mathbf{x})$ is the onset time on each seismometer which was picked manually.

Finally, the location of the sources was estimated by computing the distance, $d(\mathbf{x})$, between the onset vector ($\boldsymbol{\tau}$) and the model delay vector ($\mathbf{t}(\mathbf{x})$). The possible signal source, \mathbf{x} , was gained to minimize $d(\mathbf{x})$.

Fig 4-2-7-(3) and Fig 4-2-8-(3) show the results of source estimation. The colorbar on the right shows the $d(\mathbf{x})$ value, and the seismic stations used in this computation were also indicated with red boxes along with the location of infrasound array (black square). The results of source estimation by the multi-channel semblance method in infrasound and by minimization of $d(\mathbf{x})$ in seismometers were both shown in Fig 4-2-7-(4) and Fig 4-2-8-(4) on the red relief image map. The dots show the sources estimated by the infrasound array, and the colorbar at the bottom infers the lapse time starting on the hour just like the previous figures. On the other hand, the contour lines show the $d(\mathbf{x})$ value.

Fig 4-2-7-(4) compares that results of source estimation by the infrasound array and by the seismic stations on Event A. We could not constrain the distance of the sources by either method. Although the rough directions of the estimated sources are close, the

results do not match completely (Fig 4-2-7-(4)). We consider that the source location by the seismometer data do not have enough resolutions to discuss the difference because the spatial coverage of the stations is poor. On the contrary, Event C shows a clear match in source estimation by 2 methods as in Fig 4-2-8-(4), though the distance of the sources is not determined neither.

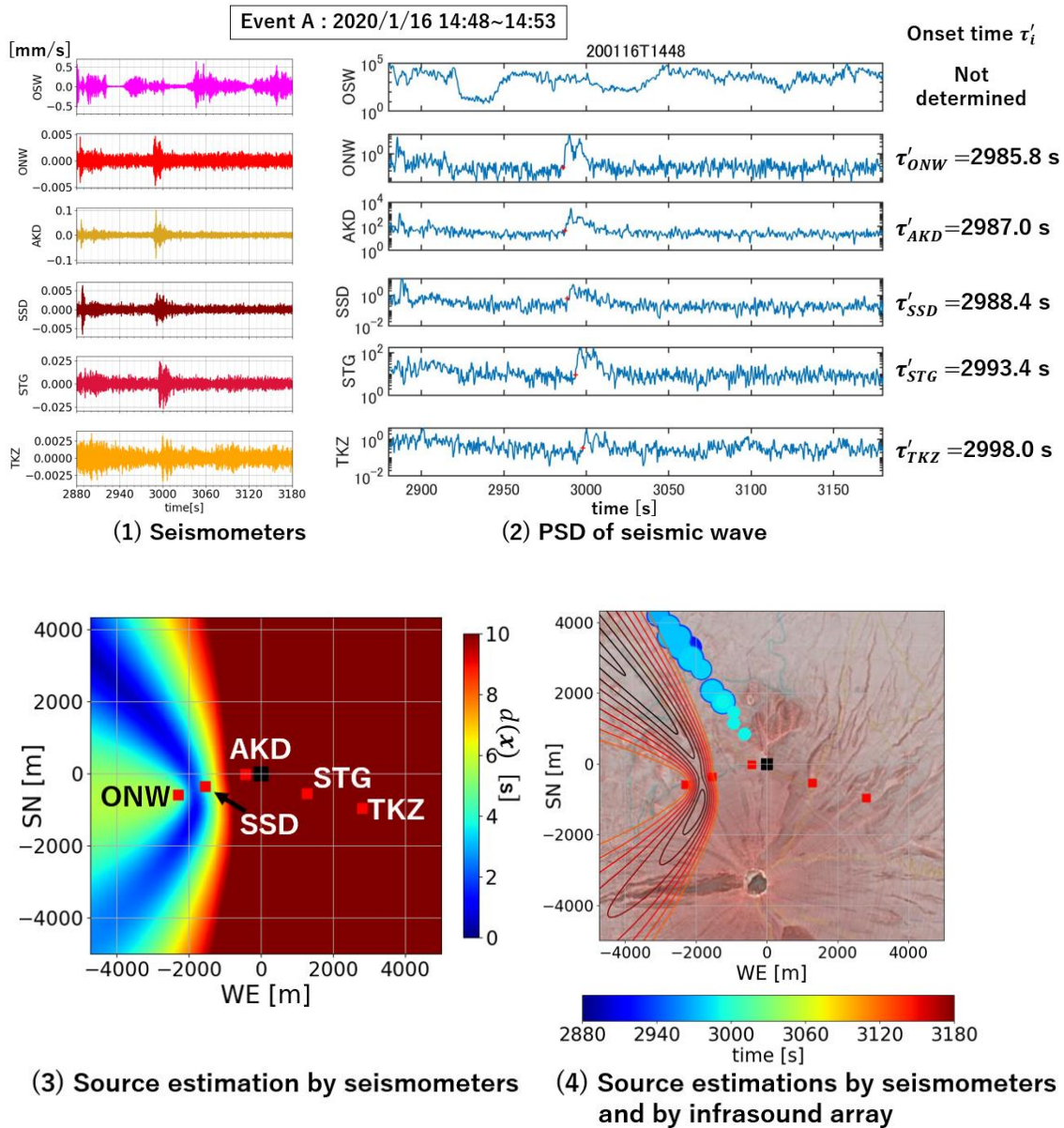


Fig 4-2-7. Seismic waveforms and PSD, results of source estimation by seismometers and by infrasound (Event A)

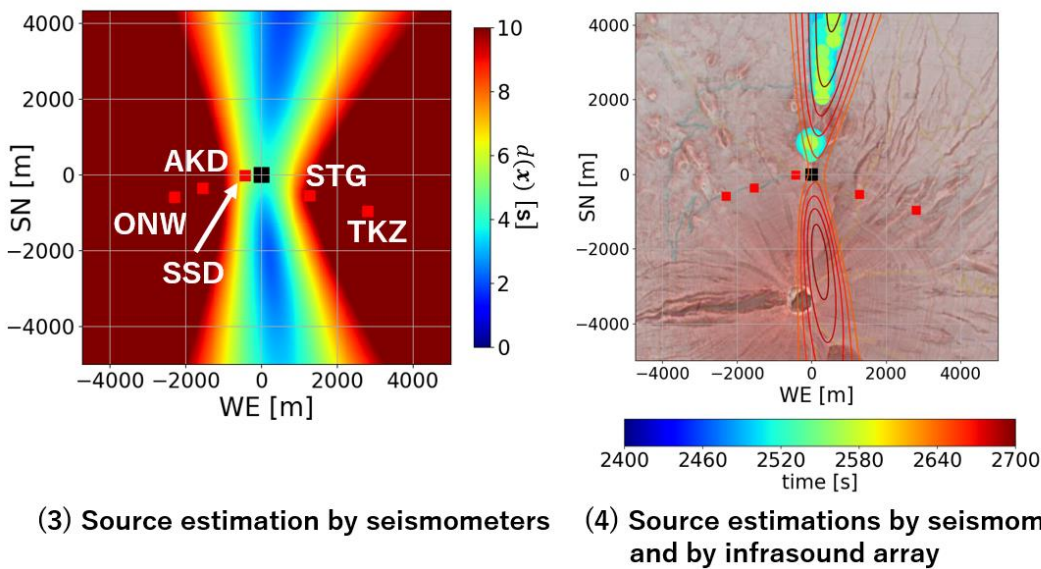
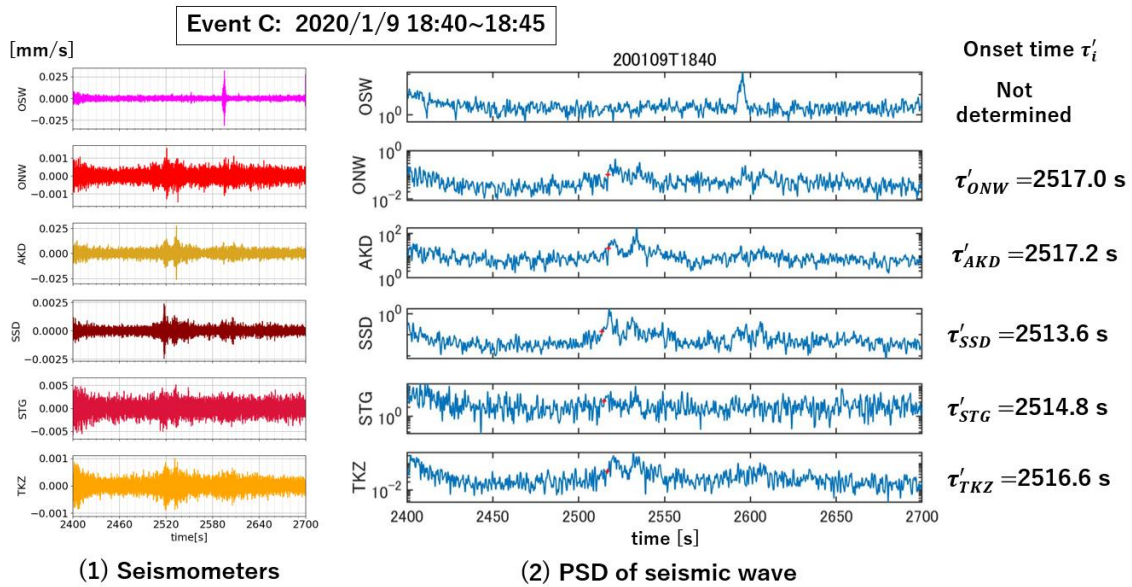


Fig 4-2-8. Seismic waveforms and PSD, results of source estimation by seismometers and by infrasound (Event C)

<Accuracy of Multi-Channel Semblance>

Although multi-channel semblance is useful to estimate the location of sources, it is important to know the accuracy of the results. Fig 4-2-9-(1) shows the semblance value of the Event B (the same event as Fig 4-2-4) at each grid in one window (60 s from $t = 1850$ s). The color bar on the right shows the semblance values and the white box shows the location of infrasound array. As this figure shows, the semblance values distribute in

a clear radial pattern. This is because the array has a high resolution in direction but low resolution in distance larger than the array aperture. In this figure, there are 2 directions with high semblance values (“Direction α ” and “Direction β ” in the Fig 4-2-9-(1)) and other weak envelopes in different directions.

Fig 4-2-9-(3) is the correlation maps of the microphone pairs of L1-L2, L1-L3 and L1-L4 on the event. There are sub-bands (blue arrows) along with the main-band (green arrows). Then, we hypothesize 2 signal sources at a point in direction α and another in direction β and calculated the travel time to the elements of L-array. The relative delay times normalized by the arrival time at L1 were obtained for L2, L3, and L4. Fig 4-2-9-(4) shows these relative delay times along with the correlation maps. Green dashed lines show the expected relative delay times from direction α , and blue dashed lines show those from direction β . The green and blue lines clearly explain the main-band and the sub-band, respectively. Therefore, it is regarded that direction β is a ghost source, which appears due to the sub-band in the correlation maps.

On the contrary, Fig 4-2-9-(2) shows the distance between the correlation vector and the model delay vector for the same time window as Fig 4-2-9-(1). As stated 3-2-1, we can also estimate the location of the sources by minimizing the distance between those vectors. If the distance value is small at a certain location, it means it is likely to be the source. Compared to the results of the multi-channel semblance methods in Fig 4-2-9-(1), it is obvious that the pattern of source location is very simple. This is because only the relative delay times with the maximum CC values were used in the analysis. The results in Fig 4-2-9-(2) show that the sources of signals came from North-West side which is consistent with the main source (direction α) in Fig 4-2-9-(1).

We need to pay attention when we interpret the results of source detection by multi-channel semblance method because they may contain the ghost envelopes (which is not likely to be the real sources) along with the real envelope. We first selected the grids of which semblance values were above a threshold. The threshold value was set to 2.0 to eliminate the noise signals with low semblance values. However, this screening was not enough to exclude the ghost envelopes with relatively high semblance value. We assume that, if the sub-bands exist in the correlation map, it would be stronger with the larger amplitude of the main-band and sometimes makes semblance values above the threshold. Thus, we installed the second screening; we employed the grids only if their semblance values were higher than 0.9 times of the maximum semblance value in the time window.

The double screening worked to eliminate the ghost envelopes. It is noted that there can be multiple real sources within a time window. We do not consider it in this study, as distinguishing overlapping infrasound from multiple sources in the field is still challenging (Yamakawa et al., 2018).

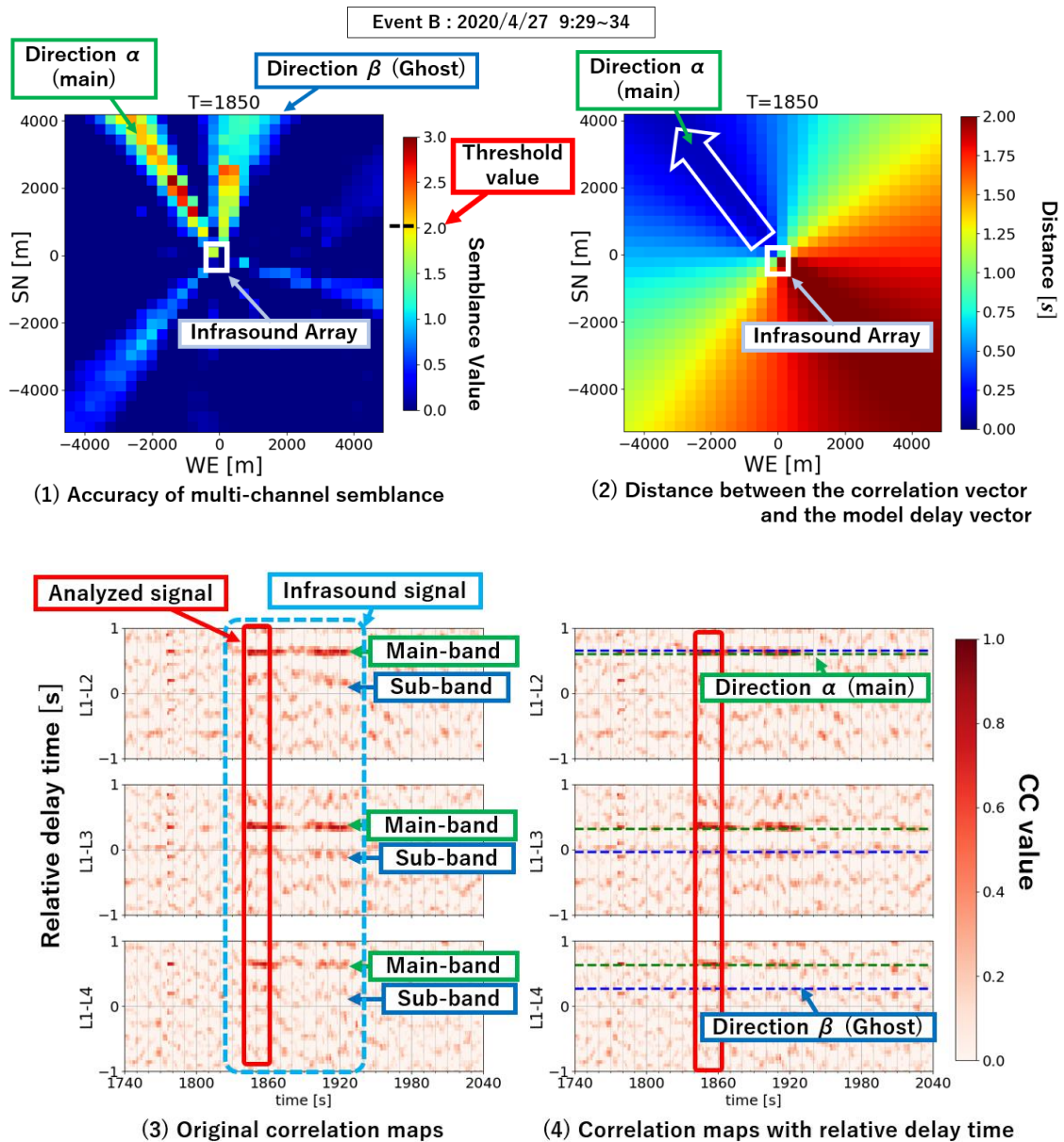


Fig 4-2-9. Map of semblance value, results of source estimation by minimization of correlation vector and the correlation maps of infrasound array on Event B.

<Visibility and Wind Level>

The visibility and wind level were gained by the methods of the previous section and the results are shown in Fig 4-2-10. The horizontal axis shows the date of observation and the vertical axis shows the infrasound visibility (green) and the low-wind probability (blue line) in 0 to 1 scale. The temporal distribution of the events is presented in this figure: the black star-shaped points represent the events which were estimated to be the avalanche signal, and the grey diamonds mark the times of the inconsistent signals.

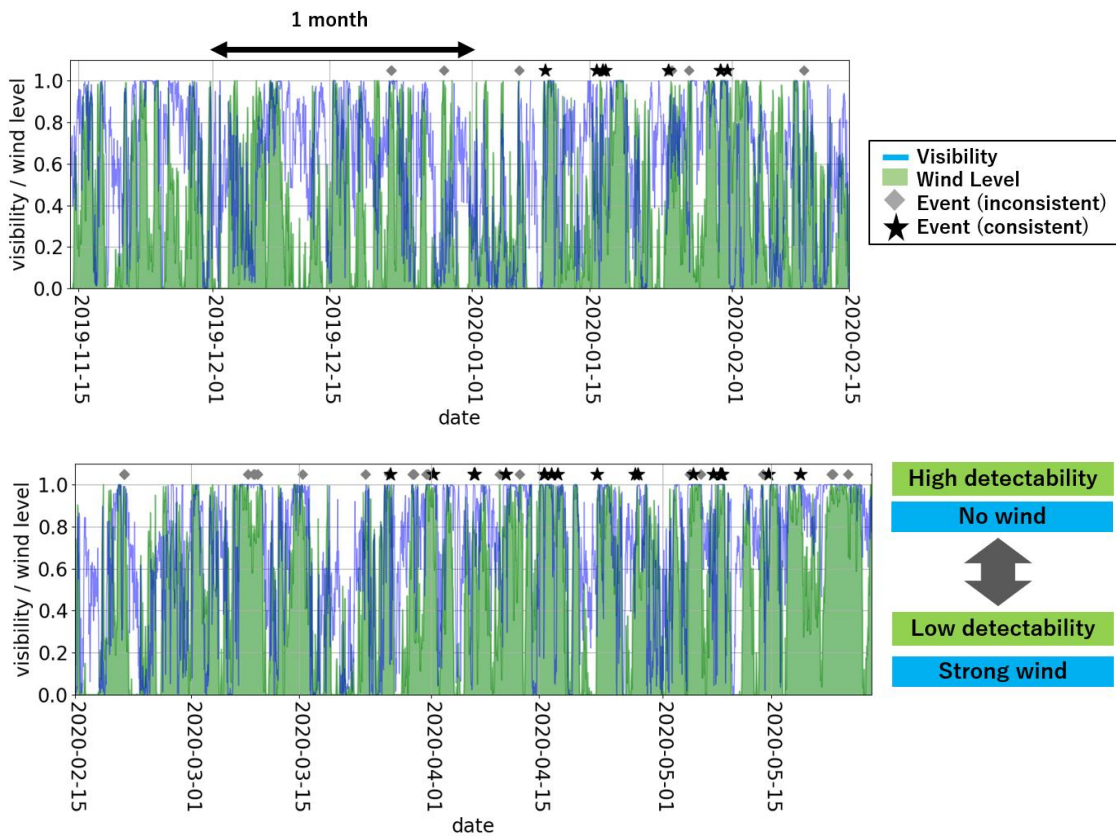


Fig 4-2-10. The visibility of infrasound array and the wind level during the observation period in 2019-2020 winter season

4-2-2 Thermometer Probe and Snowfall

The estimated snowfall measured by the thermometer probes is shown in Fig 4-2-11 with a black line. The method to calculate snowfall by the data of thermometer probes is described in 3-2-3. Since the snowfall exceeded the maximum height of the thermometer probe (120 cm), we could not assume the detailed snowfall from the beginning of February to the beginning of March as the blue dashed line shows in the figure.

Along with this result, the snowfall measured by the snow-depth meter of the automatic meteorological station next to the thermometer probes is shown in the same figure (red). The features consistent between the thermometer probes and the snow-depth meter are marked by the light-blue rectangles.

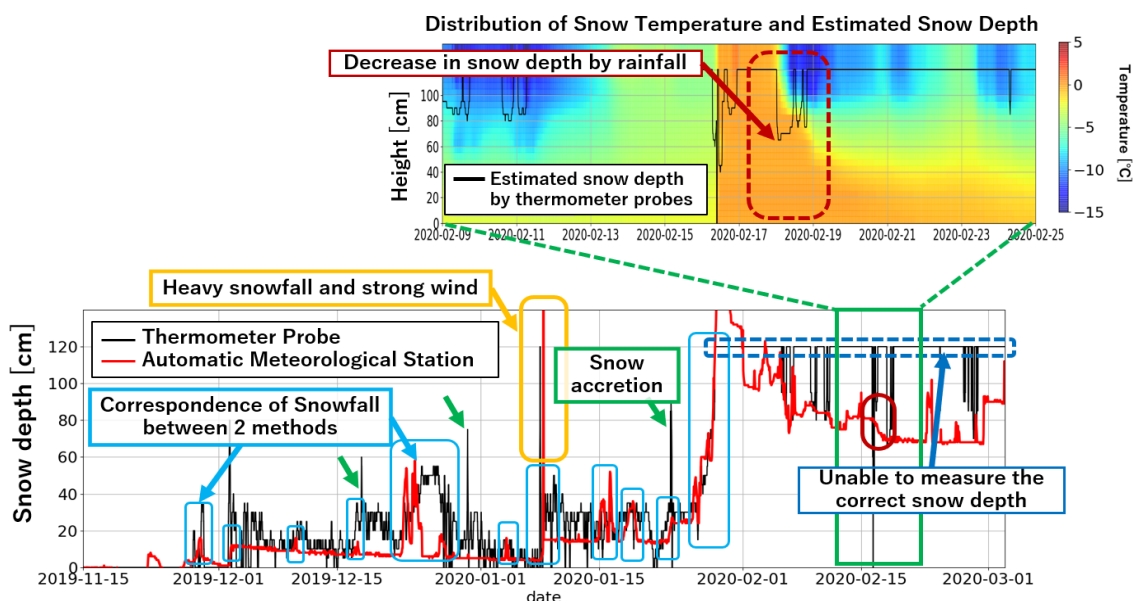


Fig 4-2-11. Estimated snow depth by thermometer probes and the recorded snow depth at automatic meteorological station at 7th step

Fig 4-2-12 shows the snow-depth data from the automatic meteorological station for the entire observation period from November 14th, 2019 to May 28th, 2020 (the same period as the observation by infrasound array) along with the event times detected by the infrasound array. The grey diamonds and black stars represent the same events as in Fig 4-2-10. Interpretation of the result is given in the next section.

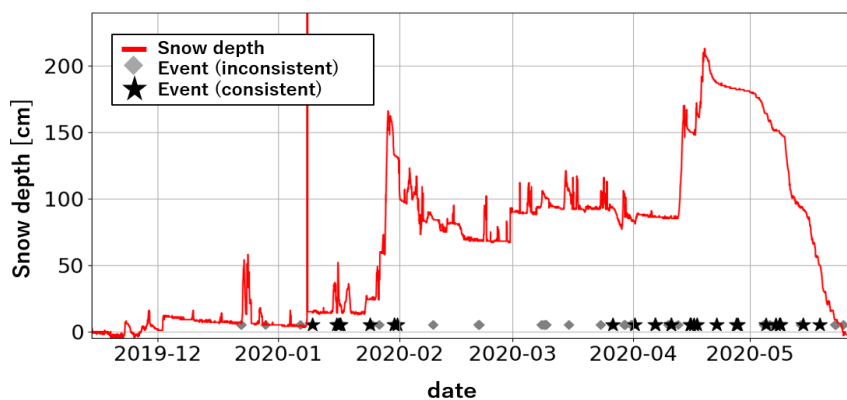


Fig 4-2-12. The recorded snow depth at automatic meteorological station at 7th step and the distribution of detected events by infrasound array

5. Discussion

5-1 2018-2019 Winter Season

5-1-1 Infrasound Microphones and Seismometers

<Verification of Infrasonic and Seismic Signals>

Although we detected the signals by the methods described in 3-1-1, we have not verified those signals as avalanches from other data such as visual information or traces.

Pérez-Guillén et al. (2020), who analyzed seismic data recording avalanches at Mt. Fuji, used information of deposits, aerial photos, and weather data to constrain the time windows and manually searched for avalanche signals in the seismograms. They reported big avalanches which left obvious traces such as destruction of toll road in March 2014, February 2016, and March 2018. However, we could not find such big avalanches either in 2018-2019 or 2019-2020 winter seasons.

The following Fig 5-1-1 compares the visibility, the estimated snow depth by the thermometer probe, and distribution of the detected events in the 2018-2019 winter season. The blue arrow shows the period of infrasound observation. Since the thermometer probe had not been installed, there was no data of snow depth before January 10th.

As Fig 5-1-1 shows, although the visibility decreases at certain points, the overall visibility is very high (1.0). The detected events were concentrated in certain periods as the orange frames represent. On the contrary, there were also the periods when the events were not detected regardless of high visibility (the red frames).

We assume that the main difference between these 2 types of periods is the snow fall and snow melt. As orange arrows show, clear snowfall or snowmelt was observed during the period with orange frame contrary to the periods of red frames with no change in snow depth. Especially, no event was detected before December 30th and after May 2nd, regardless of the sufficient visibility. Clear snowfall or snowmelt was not observed in these periods, neither. Therefore, we believe that the events were related to the snowfall and snowmelt. Although the estimated snow depth by the thermometer probe did not

represents the snow depth overall in Mt. Fuji, we presume that this data supports the idea that the detected events are related to the snowfall and snowmelt: namely avalanches.

In the following discussion, we mainly discuss the analysis of infrasonic and seismic signals which we assume to be the avalanche signals.

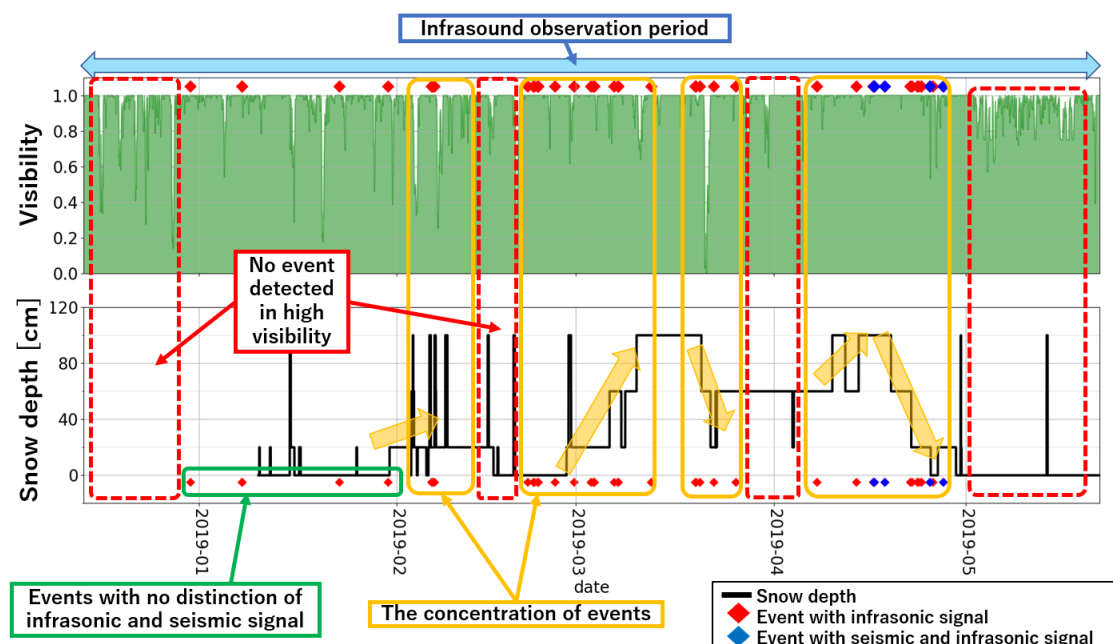


Fig 5-1-1. Visibility, estimated snow depth and the timing of the detected events in 2018-2019 winter season

<Infrasonic Signal and Seismic Signal>

As discussed in 4-1-1, the comparison in power spectral ratio between the data of the microphones and the collocated seismometer indicated that 42 of 46 detected events were infrasonic signals and that the corresponding waveforms recorded by the seismometers were the vibration of the ground surface by the infrasonic waves. Contrary to those 42 events, we found the other 4 events (15:58 on April 16th, 9:48 on April 18th, 9:08 on April 25th and 13:17 on April 27th) with both infrasonic and seismic waves.

According to Koelning et al. (2011), the avalanche releases both infrasonic and seismic waves but from different regimes. They proposed that the amplitudes of the infrasound and seismic signals roughly correlated with the size of suspension and dense layer, respectively.

Therefore, we expect that the 4 avalanches which released both infrasonic and seismic signals involved not only suspension layers but also dense layers. In contrast to the 4 avalanches, we assume that the other 42 avalanches involved no dense layers or, if any, very small ones generating undetectably weak seismic signals.

The avalanches on Mt Fuji in 2014, 2016 and 2018 that Pérez-Guillén et al. (2020) analyzed were size class 3 to 5. Thus, these avalanches might have involved dense layers to generate observable seismic signals. On the other hand, we cannot exclude the possibility that the signals they reported were infrasound waves coupled to the ground because they analyzed only seismic data. In order to distinguish the infrasonic signals from seismic signals, we have confirmed it useful to install both infrasound microphones and seismometers and to compare the powers of their data.

Besides, we believe that observation by infrasound microphones is more efficient to detect the events with only infrasonic wave than the observation only by seismometers. This is because the infrasonic signals recorded in the seismometers has very low amplitudes (e.g., 0.0002 mm/s in Fig 4-1-4) and the seismic signals with such amplitudes is very difficult to detect due to the seismic noise and to identify as the avalanche signals only by the seismic data. Although a seismic array can detect infrasound waves and distinguish them from seismic waves, it uses quite a few (seven in the previous studies) seismometers in a small area (Heck et al., 2019; Marchetti et al., 2020).

Consequently, the observation of the avalanches by both infrasound microphones and seismometers enables us to distinguish the infrasound signals and seismic signals, to identify the property of avalanches, and to monitor a wide range for avalanche signals.

5-1-2 Thermometer Probe and Avalanche Events

Fig 5-1-2 compares the timing of the 4 avalanche events accompanying both infrasound and seismic signals with the estimated snowfall by the thermometer probe. The 4 events occurred from 16th to 27th of April. The thermometer data showed that there was more than 40-cm snowfall from 10th to 11th of April and possibly April 14th. Although the snow fall on April 14th was not estimated in Fig 5-1-2 in black line determined by the STD analysis (3-1-2), the temporal diurnal change on April 13th in Fig 5-1-2 suggests the

possibility of decrease in snow depth on April 12th and the new snowfall on April 14th. The rise in the atmospheric temperature started sometime after that, though we could not specify the timing without a thermometer above the snowpack. Nevertheless, it is highly possible that the weather conditions made the avalanches denser in the four events.

As stated in the previous section, Koelning et al. (2011) proposed that the amplitudes of the infrasound and seismic signals were positively correlated with the size of suspension and dense layer, respectively. The temperature data from 16th to 27th of April and the 4 avalanche events are consistent with the idea of Koelning et al. (2011). Due to the snowfall and temperature rise, it is expected that the whole volumes of the 4 avalanches and their dense parts increased to generate seismic waves as well as the infrasound waves.

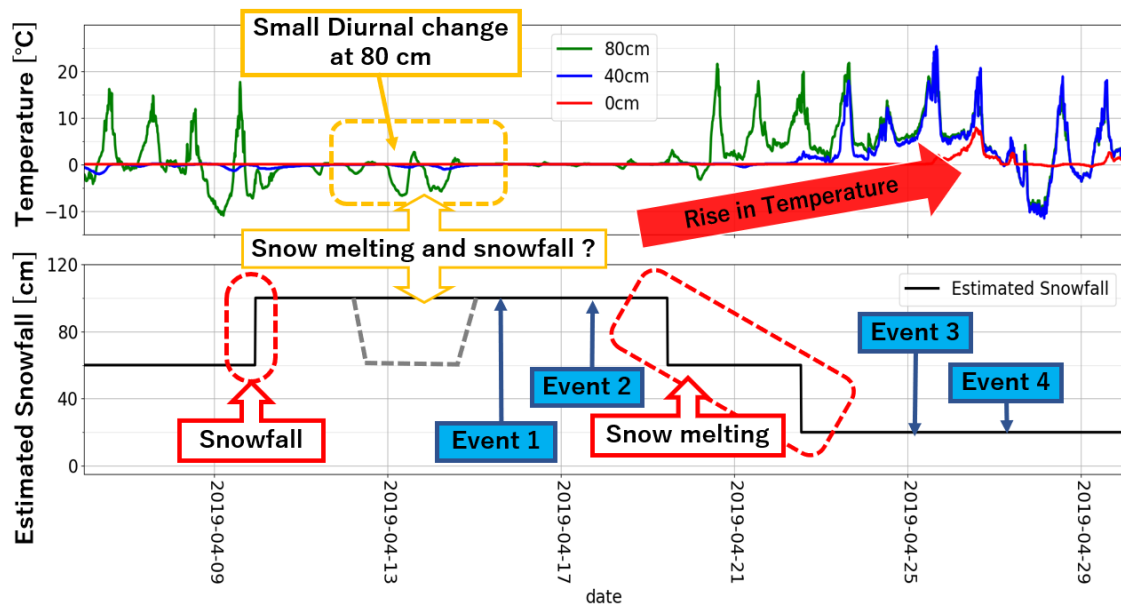


Fig 5-1-2. Temperature recorded in the thermometer probe from 7th to 30th of April (top), Estimated snow depth and the timing of the detected events with seismic signals (bottom)

5-2 2019-2020 Winter Season

5-2-1 Snowfall Estimation by Thermometer Probe

<Difference in the Results between Thermometer Probes and the Automatic Meteorological Observatory>

Fig 4-2-11 showed a good agreement of snowfall heights estimated by the thermometer probes and measured by the automatic meteorological station as indicated by the light blue frames. The absolute snow heights are different between the 2 methods: the meteorological station tends to show lower snow heights and more rapid height decrease after snowfalls (e.g., after February 2nd, 2020 in Fig 4-2-11).

We consider that the topographic difference had a large effect on the results. It is known that the local topography largely affects the amount of snow accumulation through the redistribution by winds (e.g., Doorschot et al. 2001, Schweizer et al. 2003). As Fig 2-2-5 shows, the thermometer probes were about 20 m away from the automatic meteorological station. The probes were placed close to the bottom of the valley, while the station was almost on the ridge.

<Behavior of Estimated Snowfall>

The snow heights estimated by the thermometer probes show rapid increase and decrease several times as the green arrows in Fig 4-2-11 indicate. We assume that these changes were caused by snow accretion on the probes, which is highly possible in case of snowfalls under strong winds. When the thermometers are temporary covered by the attached snow, the temperature fluctuation (STD) in those thermometers would keep low until the snow is removed by the sunshine, high temperature, wind from other direction, or other possible effects. When the snow accretion affected only an isolate thermometer, the smoothing method we employed (3-2-3) could eliminate such an inconsistently snow-covered point from the snow-height estimation. However, we need further improvements in the measurement and the analysis to completely exclude the errors.

On January 7th, 2020, the thermometer probes and the automatic meteorological station both recorded the sudden increase and decrease of snowfall (the orange frame in Fig 4-2-11). In this case, it is inferred that a heavy snowfall in strong wind covered the

thermometers and the laser instrument at the same time.

<Observation of Precipitation >

We consider an advantage of the thermometer probes is the observation of precipitation. In Fig 4-2-11, the thermometer probes show that the temperature had suddenly changed to near 0 °C at all heights on February 16th, 2020. We consider it was caused by precipitation, as the temperature of the mixture of water and snow is fixed at 0 °C. When it rained, the precipitation wetted the snowfall. Although there was no meteorological data to verify this precipitation at the 7th step (2730 m a.s.l.) of Mt. Fuji, the meteorological station at Fuji Yoshida (the town at the north base of the mountain 650 m a.s.l.) recorded high temperature (14 °C) and precipitation. This temperature is high enough to trigger the rainfall at the 7th step under the consideration of lapse rate. In addition, the thermometers on the Air probe recorded higher than 4 °C in the air, which is too warm to have snowfall. We consider that these meteorological data are reliable enough to consider the precipitation at the 7th step.

However, we do not consider that the all snowpack was completely soaked by the rainfall immediately. Conway and Raymond (1993) reported that when rain fell on new snow, water penetrated only the upper 5-10 cm in the first hour and that the penetration to greater depth began as “flow fingers” which are the streams of water and about 2-20 cm apart. Therefore, we suspect that the probe pole and/or the levee wall to which the probe was attached could play a role as these “flow fingers”. If this is the case, not all the snow layers in the area were soaked, and the thermometer probe data might not have represented their thermal structures. Yet, such water flows can also occur at natural walls such as cliffs and rocks and can affect triggering snow avalanches.

On the contrary, the snowfall observed by the automatic meteorological station only recorded the trivial decrease of snow height on that day as the brown circle imply in Fig 4-2-11. This data is not enough to identify the rainfall by itself. Thus, in the case of precipitation, we consider that the thermometer probes provide more specific and detailed information than the laser measurement of snowfall at the automatic meteorological observatory even the snow around the thermometer probes could be wet by the penetration of water along with the wood poles.

<The Advantage of Thermometer Probes>

As we discussed above, although there is some difference between the two methods, we consider that snowfall estimation by the thermometer probes is comparable to the snow-depth sensor for estimating the snowfall continuously. The thermometer probes are lighter, easier to install, less expensive, and better power-saving than the laser-based snow-depth sensor. As Fujihara et al. (2017) proposed, they are useful in monitoring the snowfalls at more points in mountain fields only accessible on foot. In addition to this, we expect that monitoring the vertical temperature distribution in snow layers is useful to analyze the detailed structures (snowflakes, weak layers etc.) and to assess the snow avalanche risks.

5-2-2 Array Analysis of Infrasound Microphones

<Visibility and the Noise Level of Infrasound Microphones>

Fig 4-2-10 shows the relationship between the visibility of infrasound microphones and the wind level of the automatic meteorological observatory at 7th step of Mt. Fuji. As this figure shows, the visibility is high when the low-wind probability is high and vice versa. Besides, the events detected by the infrasound array corresponds to the moment when the visibility is high. This confirms that detectability of the infrasound array declines when the wind is strong. This is a critical problem in avalanche observation, since it is reported that avalanches happen frequently not only after the snowfall but also during the snowfall (Heck et al., 2018, Lacroix et al., 2012). On the other hand, for monitoring, it is necessary to be aware of the detectability condition to interpret the absence of events. For this, the infrasound visibility is useful (Castano et al., 2020).

Fig 5-2-1 indicates the distribution of noise level in every infrasound microphones in L-array as stated in 3-2-1. As those figures show, there is obvious difference in the distribution of noise level between the 4 microphones. Noise levels in L_1 and L_3 are far lower than those in L_2 and L_4 . We assume that this difference is the result of installation site. L_1 and L_3 are installed in the shades of trees and buildings where snow covers the microphones for long periods. In contrast, L_2 and L_4 are installed in the open place where snow does not remain long. Scott et al. (2007) proposed that the snow cover reduces the wind noise of infrasound microphones considerably, and the trends in Fig 5-2-1 is consistent to this trend. Therefore, we expect that installing all the microphones under the snow cover can improve the visibility under bad weather conditions.

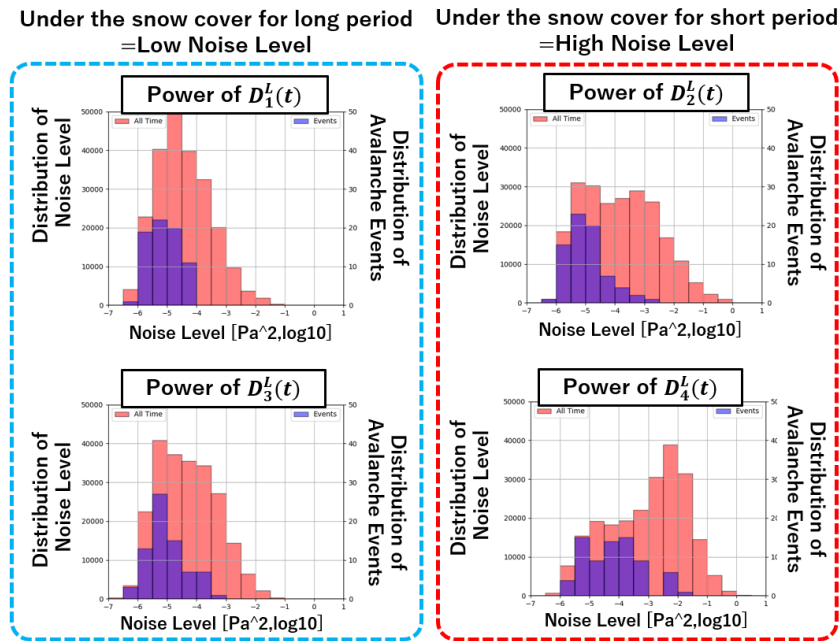


Fig 5-2-1. Distribution of noise level in 4 microphones in L-array

<Verification of Infrasound and Seismic Signals>

As in 2018-2019, we could not visually confirm the avalanches 2019-2020 winter seasons, neither. Fig 5-2-2 shows the visibility, the measured snow depth, and distribution of the detected events in the 2019-2020 winter season. The blue arrow shows the period of the infrasound array observation. As the orange frames in Fig 5-2-2 show, there are periods with concentration of events. On the contrary, there are also periods without detected signals (grey and red frames). The no-event periods tend to have low infrasound visibility (grey frames). Nevertheless, in the two periods indicated by the red frames, we had sufficiently high visibility to infer that there were few snow avalanches.

When we observed the whole-layer melting, possibly triggered by precipitation (February 16th), the visibility was very low, as shown by the blue frame. Even if we did not detect any events after the precipitation, we cannot confirm the absence of avalanches in this period.

Although there are 4 events in exception (the brown dashed frame), there were clear snowfall or snowmelt during the periods with orange frames and no clear change in snow depth during the periods with red frames. Therefore, like the previous winter season, we believe that the detected events are highly related to the avalanches.

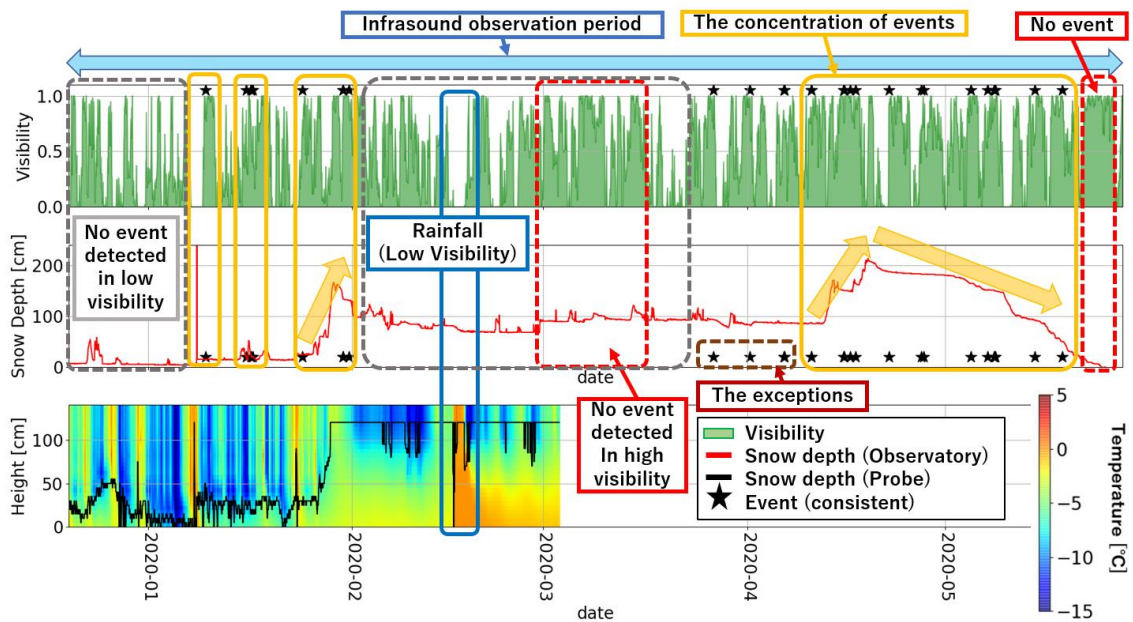


Fig 5-2-2. The visibility, the estimated snow depth and the timing of the detected events in 2019-2020 winter season

<Analysis on the Results of Source Estimation by Multi-Channel Semblance>

Most of the selected events were found to have infrasound originated from the slopes which are north from the infrasound array, as presented in 4-2-1. The multi-channel semblance method had a high resolution in direction but a low resolution in distance (Fig 4-2-9). Therefore, it is necessary to interpret the results of the source estimation results taking account of those factors.

All the estimated sources show no change in direction within the individual events. Since an avalanche goes down directly from the trigger point, the infrasonic array would observe changes in the source directions when the avalanches pass by the array (orange arrows in Fig 5-2-3). On the contrary, the directions change little if the avalanche slopes are right above or below the infrasonic array (red arrows in Fig 5-2-3). Besides, source movements could also be resolved as changes in the apparent propagation velocity of infrasound, which indicates the elevation angle of incidence (Marchetti et al., 2020). However, such observations are possible only if the avalanches flow above the array on steep slopes.

In the 26 events, the estimated source directions ranged from north-west to the north-east.

There are slopes running in fixed directions in the range as the red arrows in Fig 5-2-4 show. Therefore, it is possible that those 26 events were avalanches on these slopes.

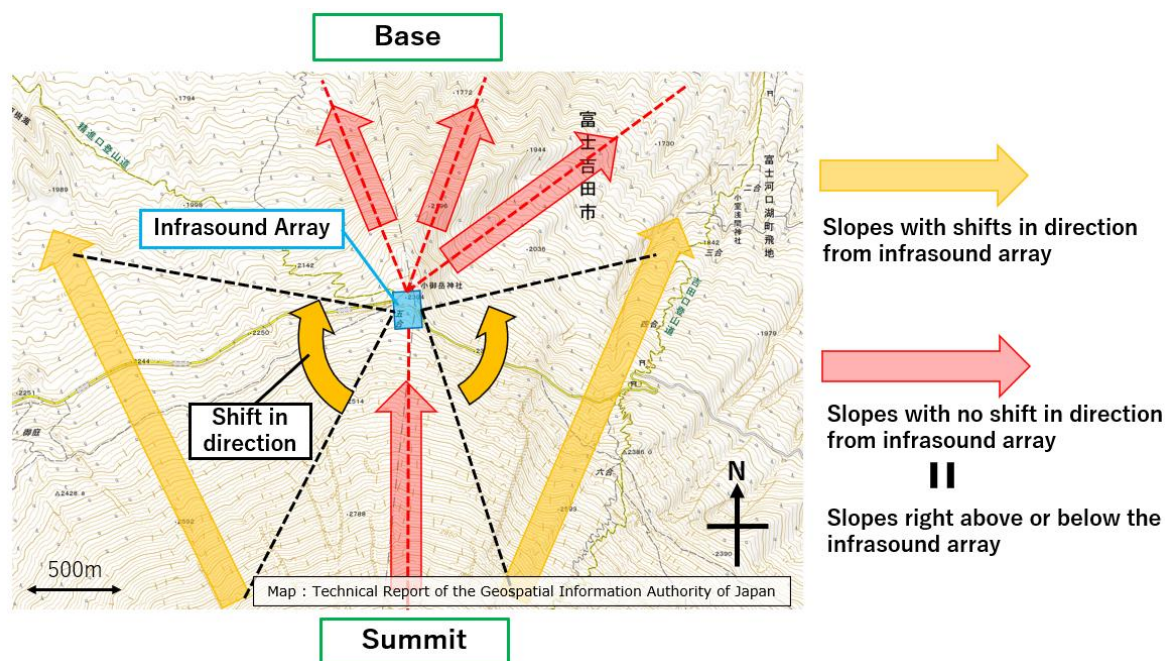


Fig 5-2-3. The model of slopes with no shift in direction from infrasound array and slopes with shift in direction from infrasound array

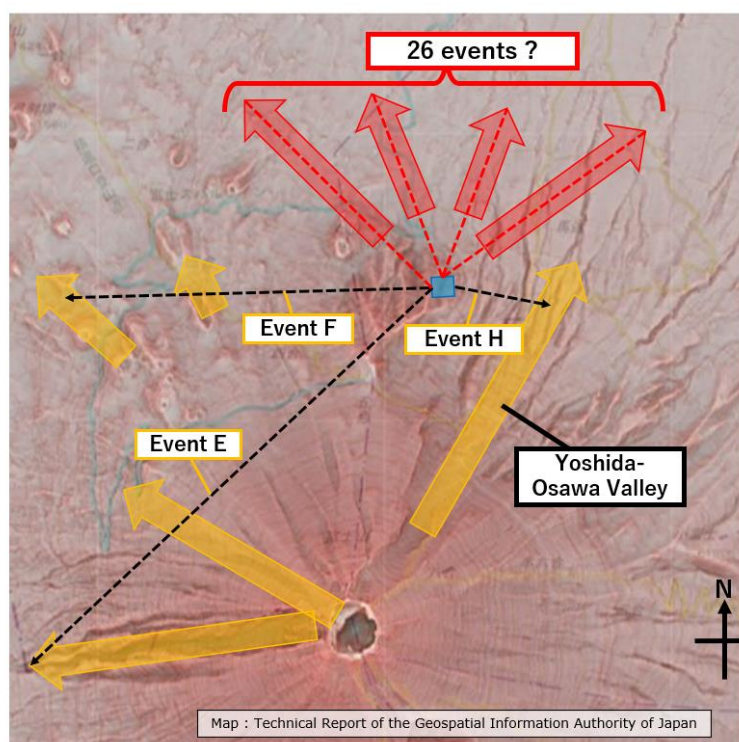


Fig 5-2-4. Estimated slopes of detected avalanches

On the other hand, in the 3 events with different trends of direction (Event E, F and H in Fig 4-2-6), there were no corresponding slope. We assume that this is because only partial infrasound signals were detected due to the topographical barrier (see next section for detail). For example, in the case of Event H, there is a huge valley called “Yoshida-Osawa valley” as the orange arrow in Fig 5-2-4 shows and the estimated direction of the sources (the black dashed arrow) corresponds to a part of it. Similar estimation can be applied on the other 2 events (Event F and E).

<Differences between This Observation and Other Previous Studies>

The previous infrasonic array analyses (Marchetti et al. 2020 and 2015, Arai et al. 2016, Ulivieri et al. 2010) successfully identified the avalanche paths in various directions using the correlation time shifts among the sensors.

Ulivieri et al. (2011) and Arai et al. (2016) installed the infrasound array at the bottom of the ravine surrounded by the slopes that had high probabilities of avalanches. In these topographical conditions, they could identify the avalanche source slopes based on the back azimuth of infrasound signals. Scott et al. (2007) and Marchetti et al. (2020) installed a 160-m aperture 5-element infrasound array at the bottom of the ravine which faces one side of the mountain. Marchetti et al. (2020) analyzed an avalanche event that flowed down to a short distance (<100 m) from the array. They estimated the back azimuth and apparent velocity of the avalanche signals and specified the detailed avalanche path on the side of mountain facing to the array. Scott et al. (2007) also identified the detailed avalanche slopes on the close side of the mountain. They combined a 150-m aperture 5-element array and two isolated sensors in several hundreds of meters. They analyzed artificially generated snow avalanches at the slopes in front of the sensors within distances of 1 km.

However, with the array in our 2019-2020 study, we only detected the signals from limited slopes. We consider that this difference resulted from the topographical features of the array site. In the previous researches, the infrasonic arrays were installed at the bottom of bowl-shaped concave slopes, to which the avalanches were expected to flow down (Fig 5-2-5-(1)). On the contrary, at Mt. Fuji, the infrasonic array was installed on the flank of a corn-shaped mountain (Fig 5-2-5-(2)). As Fig 5-2-5-(2) shows, if the infrasound array is installed to face the bowl-shaped valleys, it is expected that an array can detect signals from wide ranges, because the signals can directly reach the array from many paths. On

the other hand, if the mountain is corn-shaped, the valleys on it diverge and run behind ridges seen from the array. Then, it is more difficult to observe the signals from various valleys at one station, as the topographic barriers attenuate infrasound (Lacanna and Ripepe, 2013; Ishii et al., 2020), especially when the propagation couples with the atmospheric structure due to the source-receiver distances and altitude differences (Lacanna et al., 2014). We assume that this mechanism is the biggest reason why we could not or only partially detect the signals of slopes which are far from the infrasound array.

Based on this hypothesis, it is also possible that some of the events which were excluded as inconsistent signals in 3-2-1 could also be avalanches. In defining the inconsistent signals, we hypothesized that the infrasound reached all the microphones directly and excluded those of which relative delay times were apparently inside the L-array. However, this exclusion is not always valid if the infrasound wave diffracts and reaches the individual microphones via different paths.

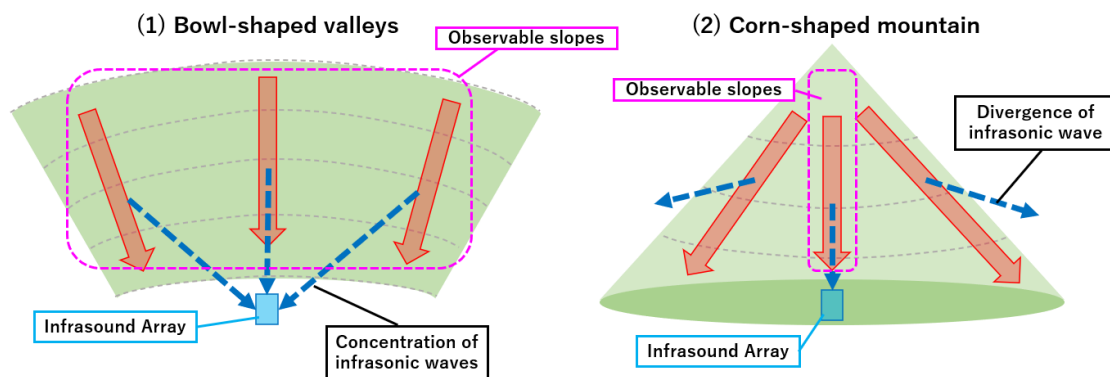


Fig 5-2-5. Simple models of infrasound propagation in bowl-shaped valleys (left) and corn-shaped mountain (right)

5-3 Designing Infrasound Observation for Snow Avalanches at Mt. Fuji

5-3-1 Ambient Infrasound Noise at Mt. Fuji

In the observation of 2018-2019 winter season, the automatic process miss-detected infrasound noise for 13 times as the avalanche events, which were excluded manually. The example waveforms, correlation maps, and spectrogram of the infrasound noise are shown in Fig 5-3-1-(1), (2) and (3) respectively (this is the same event as Fig 3-1-1-(2)). In addition, the spectra of the 2 detected infrasound signals of avalanches and the

spectrum of this infrasound noise are shown in Fig 5-3-1-(4). By comparing the spectrum, we can tell that this infrasound noise has high power in low-frequency band compared to the other detected infrasound signals.

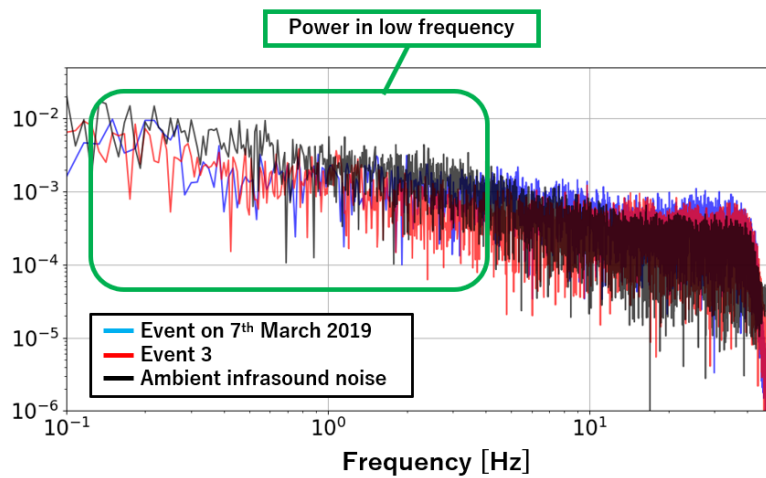
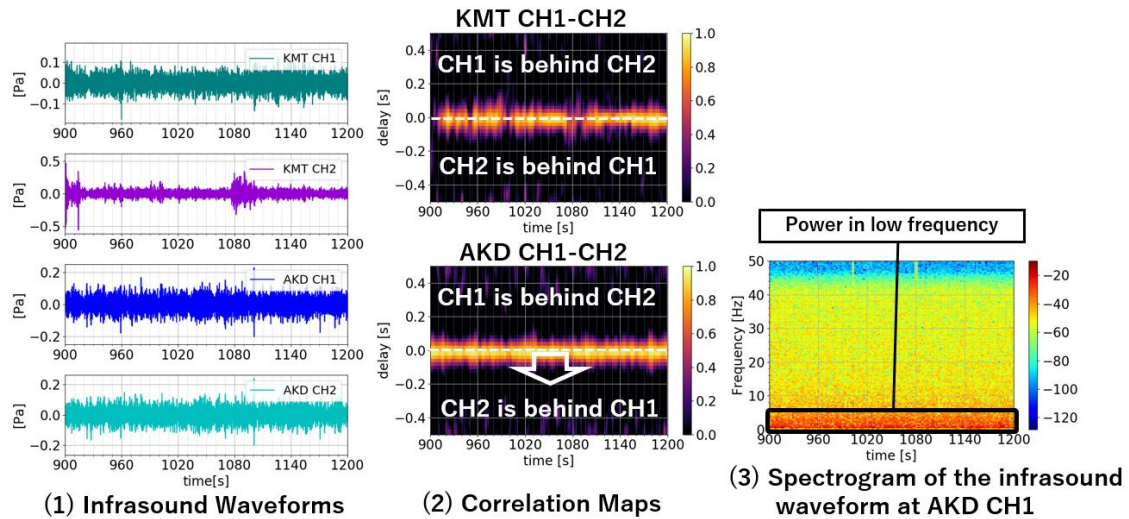


Fig 5-3-1. Infrasound waveforms, correlation maps and spectrogram of ambient infrasound noise observed in 2018-2019 winter season

Similar infrasound noise was also detected in the observation of 2019-2020 winter season. Signals on Event G (Fig 4-2-6) and those on Event A at $t = 3050\sim 3180$ (Fig 4-2-3) were the examples of frequently detected infrasound noise. Fig 5-3-2 shows the waveforms and correlation maps at all the microphones and the spectrogram on Event G.

Those noises in the two winter seasons have common features; long duration time (>120 s), unclear waveforms, and high power in low-frequency bands, as Fig 5-3-1 and Fig 5-3-2 show. In addition, as shown in Fig 5-3-1-(2), the signal of CH2 is delayed compared to CH1 at AKD in the observation in 2018-2019 winter season. Since CH1 and CH2 were aligned from south to north at AKD as Fig 2-1-2 represents, it means that the noise was from the south, that is, from the summit direction. Although the distance of the microphone pair was only 10 m, the result is consistent with the results of source estimation with the larger-aperture array in 2019-2020 (Fig 4-2-6-(G-3)).

The infrasound noise from the summit direction seems to be typical and persistent at Mt. Fuji. Although we could not identify the source of this infrasound noise, this unknown infrasound noise from the summit direction was detected for the first time by this observation and could be an obstacle for infrasound observation at Mt. Fuji.

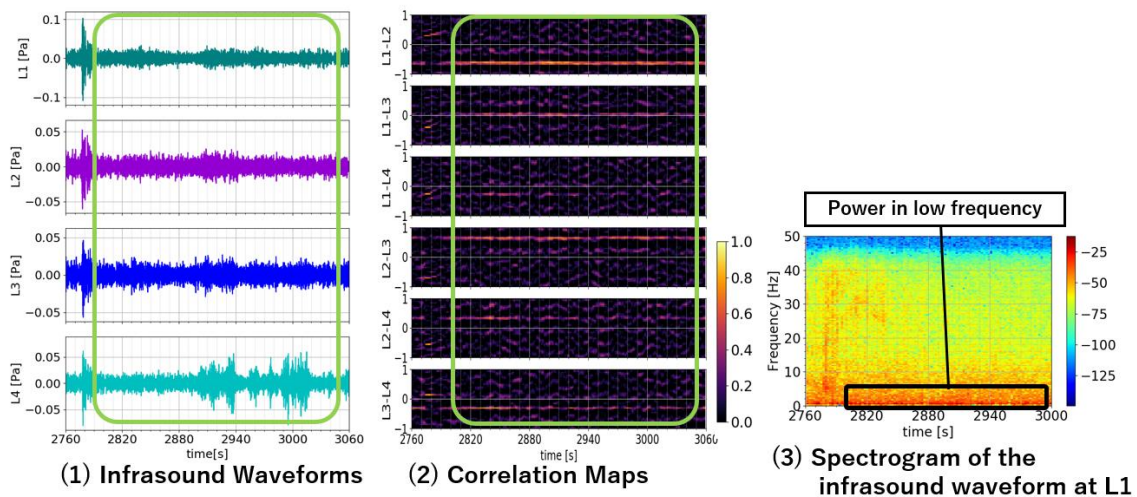


Fig 5-3-2. Infrasound waveforms, correlation maps and spectrogram of ambient infrasound noise observed in 2019-2020 winter season (Event G)

5-3-2 Comparison of the Infrasound Observations in 2018-2019 and in 2019-2020

In the observation of 2018-2019 winter season, we installed the microphone pairs at 2 stations and monitored the avalanches. As shown in Fig 4-1-6-(4), we successfully found a change in the correlation time delay between the two infrasound stations during the event. However, the 2 microphone pairs were not enough to estimate the location of the sources.

Then, in the observation of the 2019-2020 winter season, we installed the 4-element infrasound array at one station and better constrained the signal source directions. However, we found that a single station could not or only partially detect the signals of slopes that were far from it. As discussed in 5-2-2, we hypothesize that the topographical features of Mt. Fuji limit the observable areas by the infrasonic array. Namely, a comprehensive observation of avalanches on a corn-shaped mountain cannot be achieved by a single infrasonic station due to the divergence of the slopes. We expect that the use of several infrasonic arrays will cover several sides of the mountain.

5-3-3 Designing Infrasound Observation for Snow Avalanches at Mt. Fuji

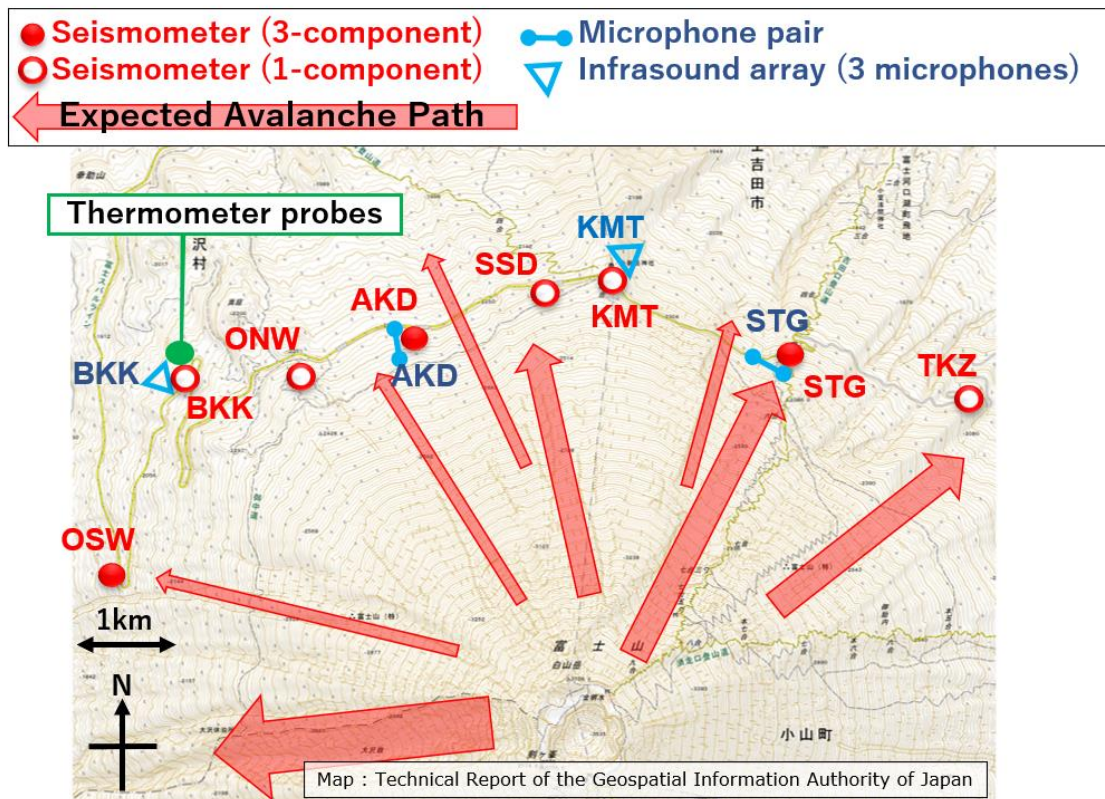


Fig 5-3-3. Design of the infrasound microphones and the seismometers in the observation of 2020-2021 winter season

Based on the results and discussion in the two winter seasons, we propose the new observation design at Mt. Fuji to effectively detect snow avalanches.

Fig 5-3-3 shows the installation in the 2020-2021 winter season. In this observation, we have installed 4 stations; 2 infrasound arrays with 3 elements (BKK and KMT, blue

triangles in Fig 5-3-3) and 2 microphone pairs (AKD and STG, blue lines), to cover the several faces of Mt. Fuji. We aim to observe the infrasound signals from a wider range by installing BKK and STG, on the west and east sides. The locations of the infrasound microphones were carefully chosen to be covered by snow to reduce the infrasound noise (see 5-2-2 for detail). Furthermore, in addition to the seismic network in the 2019-2020 winter, we have installed 1-component seismometers at BKK and KMT. This aims to distinguish the infrasonic wave and seismic wave by calculating the power ratio between the microphones and the collocated seismometers. A thermometer probe has also been installed to monitor the snowfall. It has been installed at BKK because of the accessibility. We believe that this design is effective in monitoring the avalanches and better understanding the avalanche dynamics. The locations of those installation sites are shown in Table 5-3-1 and Table 5-3-2. Table 5-3-1 shows the location of the stations and Table 5-3-2 represents the location of infrasound microphones at each infrasound array in NE plane with the origin of the location of the station in Table 5-3-2. Besides, the details of instruments are shown in Table 5-3-3.

Station Name	Latitude[N]			Longitude[E]			Altitude[m]	
	Degrees	Minutes	Seconds	Degrees	Minutes	Seconds		
OSW	35	23	19.12	138	42	30.71	2030	
BKK	35	23	5.24	138	41	43.7	2092	
ONW	35	23	18.76	138	42	20.37	2239	
AKD	seismometer	35	23	26.38	138	43	0.58	2245
	microphone	35	23	26.02	138	42	59.53	2269
KMT	35	23	38.76	138	44	1.79	2308	
SSD	35	23	37.42	138	43	44.56	2281	
TKZ	35	23	6.71	138	45	52.66	2008	

Table 5-3-1. Location and the name of the station on 2020-2021 winter season

Station Name	Component	L[m]	N[m]	E[m]
BKK	Logger	0	0	0
	CH1	8.88	-1.91	8.68
	CH2	18.57	7.08	-17.17
	CH3	10.46	-9.27	4.85
	Seis	8.90	-3.10	8.34
AKD	CH1	0	0	0
	CH2	9.54	-2.08	-9.31
	Seis	0	0	0
KMT	Logger	0	0	0
	CH1	7.77	-2.35	-7.40
	CH2	7.22	-7.18	0.70
	CH3	8.16	6.88	-4.40
STG	CH1	0	0	0
	CH2	11.22	-8.52	7.30

Table 5-3-2. Location of the infrasound microphones in NE plane on 2020-2021 winter season

Station name	Sampling Frequency [Hz]	A/D resolution	Senor	Component	Sensitivity	Unit of sensitivity	Logger	1LSB voltage [V]	Date of Installation	Date of removal
OSW	100	24	LE3D Mk3	UD	800.00	V/m/s	LS7000XT	3.22465E-06	2020/12/2	-
	100	24	LE3D Mk3	NS	800.00					
	100	24	LE3D Mk3	EW	800.00					
BKK	100	18	L22D	UD	70.00	V/m/s	EDR-X1000	7.60E-8	2020/12/2	-
	100	24	ACO 646	ch1	8.10E-03	V/Pa	LS8800 #0667	6.2585E-7		
	100	24	MEMS 3	ch2	2.10E-02					
	100	24	MEMS 4	ch3	2.20E-02					
ONW	100	18	L22D	UD	70.00	V/m/s	EDR-X1000	7.60E-8	2020/12/2	-
AKD	100	27	LE3D Mk3	UD	800.00	V/m/s	HKS-9700	3.07047E-07		
	100	27	LE3D Mk3	NS	800.00					
	100	27	LE3D Mk3	EW	800.00					
	100	24	ACO 654	ch1	8.30E-03	V/Pa	LS8800 #0668	6.26E-07		
	100	24	MEMS 1	ch2	4.00E-02					
100	24	Seis 427	ch3	70.00	V/m/s					
SSD	100	18	L22D	UD	70.00	V/m/s	EDR-X1000	7.60E-8	2020/12/2	-
KMT	100	24	ACO 647	ch1	8.30E-03	V/Pa	HKS-9700	8.18791E-07	2020/12/2	-
	100	24	MEMS 4-1	ch2	4.29E-02					
	100	24	MEMS 4-3	ch3	4.28E-02					
	100	24	Seis 428	ch4	7.00E+01	V/m/s				
STG	100	27	LE3D Mk3	UD	800.00	V/m/s	HKS-9700	2.456E-6		
	100	27	LE3D Mk3	NS	800.00					
	100	27	LE3D Mk3	EW	800.00					
	100	24	ACO 653	ch1	9.18E-03	V/Pa	LS8800 #0669	6.2585E-7		
	100	24	MEMS	ch2	0.02				LS8800 #0790	6.2585E-7
TKZ	100	18	L22D	UD	70.00	V/m/s	EDR-X1000	7.60E-8	2020/12/2	-

Table 5-3-3. List of instruments used in the observation on 2020-2021 winter season

6. Conclusions

We installed infrasound microphones, seismometers and thermometer probes at Mt. Fuji for 2 winter seasons (2018-2019 and 2019-2020). We detected the snow avalanches by using the infrasonic and seismic signals. Besides, analyzing the data of the thermometer probes, we captured the snow depth, snowfall, the snow-layer melting, and weather conditions. The combination of the information from the infrasound and seismic data and from the thermometer probe enabled us to understand the relationship between avalanches and snow conditions.

In the 2018-2019 winter observation, although the sources of those signals were not determined due to the geometry of microphone pairs, by comparing the power spectra of the infrasound data and the collocated seismic data at a station, we successfully distinguished the infrasonic and seismic signals. Surprisingly, only 4 of 46 detected events were estimated to involve both seismic and infrasonic signals, while only infrasonic signals were detected in the other 42 events. Furthermore, based on the estimated snow depth by the thermometer probes, the 4 events with seismic signals occurred during the snowfall and temperature rise in spring. We expected that the whole volumes of the 4 avalanches and their dense parts increased to generate seismic waves as well as infrasound waves.

In the 2019-2020 winter observation, we used the multi-channel semblance methods for selected events, and found that 26 of them originated from the slopes in the limited range from north-west to north-east from the array. Only 3 were estimated to originate from the other slopes. Therefore, we hypothesize that the topographical features of Mt. Fuji limited the observable areas by the infrasonic array at one station.

In both winter seasons, most of the events were detected during and shortly after the new snowfall or snowmelt. Although it is well-known that snowfall and snowmelt are the dominant factor for the avalanches, this study confirmed for the first time that it can be monitored only by infrasound and thermometer-probe observations.

Based on the results from the observations and data analyses for the two years, we confirmed the following important points for the comprehensive observation of avalanches in Mt. Fuji.

1. Installation of both infrasound microphones and seismometers enable us to detect the infrasound signals efficiently and to distinguish the infrasonic signals and seismic signals.
2. The topographical features of Mt. Fuji limit the observable areas by the infrasonic array at one station. Installation of multiple infrasound array is essential to cover the wide range of slopes.
3. Thermometer probes can measure the snow depth, snow-layer melting or precipitation, and the air temperatures. Besides, it is portable and practical enough to install in the severe mountainous field with high altitude during winter.
4. Combination of infrasonic arrays, seismometers, and thermometer probes allow to capture the relationship between weather conditions (such as snowfall, snowmelt, precipitation and rise in temperature) and avalanches.

In addition to those 4 points, our observations revealed the background noises against the infrasound measurements at Mt. Fuji for the first time. In particular, unknown persistent infrasound noise from the summit of Mt. Fuji was often recorded, which is expected to be the disturbance for the infrasound observation in Mt. Fuji.

Finally, we propose a snow-avalanche monitoring system suitable for Mt. Fuji based on the above points. In this design, it is expected to observe the infrasound signals from a wider range of slopes, to distinguish the infrasonic signals and seismic signals, and to estimate the location of sources. The observation of this design is carried out in 2020-2021 winter season.

An important task in the future is the observation and analysis of 2020-2021 winter season. It is also expected to specify the sources and mechanism of the ambient infrasound noise, which is scientifically and practically interesting.

7. Acknowledgements

We would like to thank Mie Ichihara from The Earthquake Research Institute, The University of Tokyo for precious advice and support. We thank Shinichi Sakai from The Earthquake Research Institute, The University of Tokyo, Ryo Honda and Mitsuhiro Yoshimoto from Mount Fuji Research Institute, Yamanashi Prefectural Government, Hiroshi Aoyama from Hokkaido University and Koichi Nishimura from Nagoya University for their advice, support and discussion of the results. We also thank Hidetoshi Takahashi and Ruka Wada from Keio University and Isao Shimoyama from Toyama Prefectural University for developing and providing the MEMS infrasound sensors for this research.

8. References

Anma, S., 2007. Lahars and slush lahars on the slopes of Fuji volcano, *edited by: S. Aramaki, T. Fujii, S. Nakada, N. Miyaji, Yamanashi Institute of Environmental Science, Fujiyoshida*. 285-301 (in Japanese with English summary).

Anma, S., M. Fukuse, K. Yamashita, 1988. Deforestation by slush avalanches and vegetation recovery on the eastern slope of Mt. Fuji, *in: Proc. of Internat. Symp. INTERPRAEVENT 1988, 4-8 July 1988, Graz, Austria*, 133-156.

Arai, N., T. Imai, M. Otsuki, Y. Saito, T. Murayama, M. Iwakuni, 2017. Detection of avalanche locations using infrasound array data, *Bulletin of Glaciological Res.*, **35**, 1-6.

Bartelt, P. and M. Lehning, 2002. A physical SNOWPACK model for the swiss avalanche warning Part I: numerical model, *Cold regions sci. and tech.*, **35**, 123-145.

Cannata, A., P. Montalto, D. Patane, 2013. Joint analysis of infrasound and seismic signals by cross wavelet transform: detection of Mt. Etna explosive activity, *Nat. Hazards Earth Syst. Sci.*, **13**, 1669-1677.

Castano, L. M., C. A. Ospina, O. E. Cadena, B. Glavis-Arenas, J. M. Londono, C. A. Laverde, T. Kaneko, M. Ichihara, 2020. Continuous monitoring of the 2015-2018 Nevado del Ruiz activity, Colombia, using satellite infrared images and local infrasound records, *Earth, Planets and Space*. **72**, 81.

Conway, H. and C. F. Raymond, 1993. Snow stability during rain, *Jour. of Glaciology*. **39**, 635-642.

Doorschot, J., N. Raderschall, M. Lehning, 2001. Measurements and one-dimensional model calculations of snow transport over a mountain ridge, *Annals of Glaciology*. **32**, 153-158.

Fujihara, Y., K. Takase, A. Ogura, E. Ichion, S. Chono, 2015. Verification of snow-depth measurement technique based on snow temperature profile, *IDRE Jour.*, **300**, 207-213.

Fujihara, Y., K. Takase, S. Chono, E. Ichion, A. Ogura, K. Tanaka, 2017. Influence of topography and forest characteristics on the snow distributions in a forested catchment, *Jour. of Hydrology*. **546**, 289-298.

Gascón, E., J. L. Sanchez, S. Frenández-González, L. Hermida, L. López, E. García-Ortega, A. Merino, 2015. Monitoring a convective winter episode of the Iberian Peninsula using a multichannel microwave radiometer, *Jour. of Geophys. Res. Atmos.*, **120**, 1565-1581.

Heck, M., M. Hobiger, A. van Herwijnen, J. Schweizer, D. Fah, 2018. Localization of Seismic events produced by avalanches using multiple signal classification, *Geophys. Jour. Int.*, **216**, 201-217.

Ichihara, M., 2016. Seismic and infrasonic eruption tremors and their relation to magma discharge rate: A case study for sub-Plinian events in the 2011 eruption of Shinmoe-dake, Japan, *Jour. Geophys. Res. Solid Earth*. **121**, 7101–7118.

Ishii, K., A. Yokoo, M. Iguchi, E. Fujita, 2015. Utilizing the solution of sound diffraction by a thin screen to evaluate infrasound waves attenuated around volcano topography, *Jour. of Volcanology and Geothermal Res.*, **402**, 106983.

Koelning, A., E. Suriñach, I. Vilajosana, J. Hubl, B. Sovilla, M. Hiller, F. Dufour, 2011. On the complementariness of infrasound and seismic sensors for monitoring snow avalanches, *Nat. Hazards and Erath Syst. Sci.*, **11**, 2355-2370.

Kodou, J., 1994. Mizukanokyou no Kishougaku – Tihyoumen no Mizusyuusi, Netusyuusi (Meteorology of water environment: Water balance and heat balance on the earth surface), Asakura Shoten.

Kurokawa, A. K. and M. Ichihara, 2020. Identifications of infrasonic and seismic components of tremors in single-station records: application to the 2013 and 2018 events at Ioto Island, Japan, *Earth, Planets and Space*, **72**, 171.

Lacanna, G. and M. Ripepe, 2013. Influence near-source volcano topography on the acoustic wavefield and implication for source modeling, *Jour. of Volcanology and Geothermal Res.*, **250**, 9-18.

Lacanna, G., M. Ichihara, M. Iwakuni, M. Takeo, M. Iguchi, M. Ripepe, 2014. Influence of atmospheric structure and topography on infrasonic wave propagation, *Jour. Geophys. Res.*, **119**, 2988-3005.

Lacroix, P., J.-R. Grasso, J. Roulle, G. Giraud, D. Gotez, S. Morin, A. Helmstetter, 2012. Monitoring of snow avalanches using a seismic array: Location, speed estimation, and relationship to meteorological variables, *Jour. of Geophysical Res.*, **117**, F01034.

Langston, C. A., 2004. Seismic ground motions from a bolide shock wave, *Jour. Geophys. Res.*, **109**, B12309.

Marchetti, E., A. van Herwijnen, M. Christen, M. C. Silengo, G. Barfucci, 2020. Seismo-acoustic energy partitioning of a powder snow avalanche, *Earth Surf. Dynam.*, **8**, 399-411.

Marchetti, E., N. Ripepe, G. Ulivieri, A. Koelning, 2015. Infrasonic array criteria for automatic detection and front velocity estimation of snow avalanches: towards a real-time early-warning system, *Nat. Hazards Earth Syst. Sci.*, **15**, 2545-2555.

Matoza, R.S., D. Fee, 2014. Infrasonic component of volcano-seismic eruption tremor, *Geophys. Res. Lett.*, **41**, 1964-1970.

Pérez-Guillén, C., K. Tsunematsu, K. Nishimura, D. Issler, 2019. Seismic location and tracking of snow avalanches and slush flows on Mt. Fuji, Japan, *Earth Surf. Dynam.*, **7**, 989-1007.

Pierson, T.C., R.J. Janda, J.C. Thouret, C.A. Borrero, 1990. Perturbation and melting of snow and ice by the 13 November 1985 eruption of Nevado del Ruiz, Colombia, and consequent mobilization, flow, and deposition of lahars, *Jour. of Volcanology and Geothermal Res.*, **41**, 17-66.

Ripepe, M., E. Marchetti, G. Ulivieri, 2007. Infrasonic monitoring at Stromboli Volcano during the 2003 effusive eruption: insights on the explosive and degassing process of an open conduit system, *Jour. Geophys. Res-Sol EA.*, **112**, 1-13.

Schattan, P., G. Baroni, S. E. Oswald, J. Schöber, C. Fey, C. Kormann, M. Huttenlau, and S. Achleitner, 2017. Continuous monitoring of snowpack dynamics in alpine terrain by aboveground neutron sensing, *Water Resour. Res.*, **53**, 3615-3634.

Schweizer, J. and J. B. Jamieson, 2000. Field observations of skier-triggered avalanches, *Proceedings International Snow Science Workshop, Big Sky, Montana, U.S.A., 2-6 October 2000*.

Schweizer, J., J. B. Jamieson, M. Schneebeli, 2003. Snow avalanche formation, *Rev. of Geophys.*, **41**, 1016-1041.

Scott, E. D., C. T. Hayward, R. F. Kubichek, J. C. Hamann, J. W. Pierre, B. Comey, T. Mendenhall, 2007. Single and multiple sensor identification of avalanche-generated infrasound, *Cold Regions Sci. and Tech.*, **47**, 159-170.

Shields, F. D., 2005. Low-frequency wind noise correlation in microphone arrays, *Jour. Acoust. Soc. Am.*, **117**, 3489.

Steinkogler, W., B. Sovilla, M. Lhning, 2014. Influence of snow cover properties on avalanche dynamics, *Cold Regions Sci. and Tech.*, **97**, 121-131.

Tanaka, A., Y. Yamamura, T. Nakano, 2008. Effects of forest-floor avalanche disturbance on the structure and dynamics of a subalpine forest near the forest limit n Mt. Fuji, *The Ecological Society of Japan.*, **23**, 71-81.

Ulivieri, G., E. Marchetti, M. Ripepe, I. Chiambretti, G. De Rosa, V. Segor, 2011. Monitoring snow avalanches in Northwestern Italian Alps using an infrasound array. *Cold region Sci. and Tech.*, **69**, 177-183.

Wada, R. and H. Hidetoshi, 2020. Time response characteristics of highly sensitive barometric pressure change sensor based on MEMS piezoresistive cantilevers, *Jpn. Jour. of Appl. Phys.*, **59**, 070906.

Watada, S., T. Kunugi, K. Hirata, H. Sugioka, K. Nishida, S. Sekiguchi, J. Oikawa, Y. Tsuji, H. Kanamori, 2006. Atmospheric pressure change associated with the 2003 Tokachi-Oki earthquake, *Geophys. Res. Lett.*, **33**, L24306.

Yamakawa, K., K. Ishii, H. Aoyama, T. Nishimura, M. Ripepe, 2018. Azimuth estimation from a small aperture infrasonic array: test observation at Stromboli Volcano, Italy, *Geophys. Res. Lett.*, **45**, 8931-8938.